Study of buckling and delamination of ductile thin films on rigid substrates

Nadia Ben Dahmane

To cite this version:

Nadia Ben Dahmane. Study of buckling and delamination of ductile thin films on rigid substrates. Mechanics of materials [physics.class-ph]. Université Grenoble Alpes, 2018. English. NNT : 2018GREAI013 . tel-02012703v1

HAL Id: tel-02012703

https://theses.hal.science/tel-02012703v1

Submitted on 9 Feb 2019 (v1), last revised 15 Jul 2019 (v2)

Communauté
UNIVERSITÉ Grenoble Alpes

THÈSE

Pour obtenir le grade de

DOCTEUR DE LA COMMUNAUTE UNIVERSITÉ DE GRENOBLE ALPES
Spécialité : **Matériaux, Mécanique, Génie Civil, Electrochimie**

Arrêté ministériel : 25 mai 2016

Présentée par

Nadia BEN DAHMANE

Thèse dirigée par **Guillaume PARRY**,
codirigée par **Rafael ESTEVEZ**

préparée au sein **du Laboratoire de Science et Ingénierie des Matériaux et des Procédés (SIMaP)**
et de **École doctorale d'Ingénierie - Matériaux Mécanique Energétique Environnement Procédé Production (I-MEP2)**

Etude du cloquage de films minces élastoplastiques sur substrat rigide

Study of buckling delamination of ductile thin films on rigid substrates

Thèse soutenue publiquement le **8 Février 2018**,
devant le jury composé de :

M. Benoit ROMAN
Directeur de Recherche , CNRS, Président
M. Damien FAURIE
Maître de Conférence HDR, Université Paris 13 , Rapporteur
M. Patrick MCGARRY
Professeur associé, NUI, GAlway, Rapporteur
M. Christophe COUPEAU
Professeur des Universités, Institut PPRIME, Examinateur
M. Guillaume PARRY
Maître de Conférences HDR, Grenoble INP, Directeur de thèse
M. Rafael ESTEVEZ
Professeur, Université Grenoble-Alpes, Co-directeur de thèse

“Every block of stone has a statue inside it and it is the task of the sculptor to discover it.”

Michelangelo

Acknowledgements

Ce travail de recherche n'aurait pas pu aboutir sans l'aide de plusieurs personnes: encadrants, collègues, amis et famille. Qu'elles trouvent içi l'expression de ma gratitude pour leurs apports scientifiques, leur confiance, leur générosité et toutes leurs qualités humaines.

Tout d'abord, je souhaite remercier les membres du jury. Je remercie Damien Faurie et Patrick McGarry d'avoir accepté d'être les rapporteurs de mon manuscrit et Benoit Roman d'avoir présidé mon jury. Vos relectures attentives et vos remarques et suggestions m'ont été très bénéfiques. Je tiens aussi particulièrement à remercier Christophe Coupeau non seulement pour avoir accepté de faire partie de mon jury de thèse mais aussi pour tout l'intérêt qu'il a su porter à mon projet durant ces trois années et pour son aide précieuse au niveau expérimental.

Durant ma thèse j'ai aussi eu le plaisir de collaborer avec Marc Fivel pour le couplage FEM/DDD et Marc Verdier pour les essais de nano-indentation. Merci à vous deux pour tous nos échanges, votre générosité et vos disponibilités malgré des emplois de temps déjà bien chargés.

Je voudrais ensuite remercier mes directeurs de thèse Guillaume Parry et Rafael Estevez. Merci à toi Guillaume de m'avoir communiqué cet engouement et cette curiosité pour les instabilités mécaniques. Durant cette thèse nous avons été comme deux inspecteurs cherchant à comprendre la présence de ces «cloques bizarres» observées sur les films d'or. Nous avons suivi plusieurs pistes et beaucoup n'ont pas abouti. Heureusement que tu as été là en ces moments difficiles rassurant et confiant me rappelant qu' «on est à ça du résultat». Merci à toi Rafael pour toutes les discussions scientifiques, tes remarques pertinentes et les efforts que tu as mis (toujours avec le sourire et la bonne humeur) à corriger mon manuscrit de thèse. Je te remercie également d'avoir instauré les MuMechs. J'ai beaucoup appris de ces sessions et je pense qu'elles ont permis d'instaurer une culture d'entraide et de dialogue au sein de l'équipe ce qui a été fortement bénéfique pour tous les thésards.

Je remercie aussi particulièrement Alain pour toute son aide avec le matériel informatique. Je ne peux même pas compter le nombre de fois où je suis allée te voir pour un problème de réseau, de serveur ou de stockage. Tu m'as toujours accueillie avec le sourire, écoutée attentivement et fait de ton mieux pour me proposer une solution. Pour tout cela un grand merci!

Cette expérience n'aurait pas pu être la même sans mes amis et collègues les thésards du SIMaP. Arrivée le premier jour, je t'ai trouvé toi Alexis tout seul au milieu de tous ces bureaux vides dans la salle 327. On a vite sympathisé et je t'ai raconté mes déboires de titre de séjour et toi tes déboires de signature de contrat (vive la bureaucratie!). Plus tard ça a été de nos problèmes numériques qu'on a débattus, de mes sacrées non-linéarités et de ton optimisation. On s'est mutuellement soutenu tout au long de cette aventure et je suis bien contente de t'avoir vu soutenir avec brio. Bonne route à toi!

Après mon arrivée, le bureau 327 n'est pas resté longtemps vide. Il y'a eu bientôt Anne, Ilhem, Marie, le Pamplemousse, Clément puis Nico et Idir. On a vite formé une sacrée équipe et on a partagé ensemble pas mal de repas, de fous rires, de discussions plus ou

moins sérieuses et des soirées à Grenoble. Je remercie particulièrement Marie et Ilhem d'avoir été mes camarades de rédaction. Ça aurait été beaucoup plus difficile sans vous! Je remercie aussi particulièrement Cristian pour son optimisme contagieux et pour m'avoir fait découvrir le café guatémaltèque. Je ne saurais oublier les anciens: Mark, Aymen, Laurent, Fanny, Audrey et Olivier qui étaient toujours prêts a transmettre leurs expériences et à me donner des conseils. Je remercie aussi toute l'équipe des PM Juniors: Solène, Zélie, Rosen, Michael, Damien et les derniers arrivés que j'apprécie tout autant: Aseem, Imad, Lorenzo, Charline et Amandine. Merci pour les pauses café sur la terrasse, les gâteaux partagés et la bonne humeur. Je veux également remercier Robin et Etienne qui sont souvent venus déjeuner avec nous et avec qui j'ai beaucoup discuté modélisation et Python. J'ai beaucoup apprécié le côté humain de nos échanges et pour moi, vous faites clairement partis des thésards du troisième;-)

Je tiens aussi à remercier tous les gourmets du troisième étage, notamment Catherine, Magali, Nadine, Édouard et Guy pour les repas partagés, les idées culinaires et tous nos échanges. Rien de tel qu'un bon repas et de la bonne humeur pour oublier les tracas de la thèse.

Je remercie mes anciens profs de PHELMA qui sont devenus collègues, m'ont beaucoup aidé et éclairé mes choix en particulier Fabien, Alexis et Catherine.

Merci à Virginie et à Sylvie. Vous m'avez beaucoup aidé administrativement du début de la thèse jusqu'au dernier jour.

Je remercie mes parents et ma famille qui ont toujours cru en moi, qui m'ont toujours encouragée et qui n'ont jamais souhaité autre chose que mon bonheur et mon épanouissement. Du fond du cœur, merci! Pour finir, j'aimerais te remercier Alexandre pour avoir été à été à mes côtés pendant toute cette aventure. J'ai été très heureuse de partager cette réussite avec toi, et j'espère qu'ensemble, nous aurons plein d'autres moments de bonheur!

Contents

List of Figures

List of Tables

Introduction

Thin films and coatings are extensively used for their mechanical, electronic and optoelectronic properties [37]. They are involved in a variety of technological applications ranging from low emissivity windows [55] to microelectronic devices [105]. During the deposition process, thin films can be subjected to high residual compressive stresses [73, 114] reaching up to a few GPa. These residual stresses may cause simultaneous buckling and delamination of the film, giving rise to various blister morphologies such as circular blisters, straight-sided blisters or telephone cord blisters as shown in figure 1. Such defects are detrimental to the mechanical properties and conductivity of the multi layer system and are thus highly undesirable.

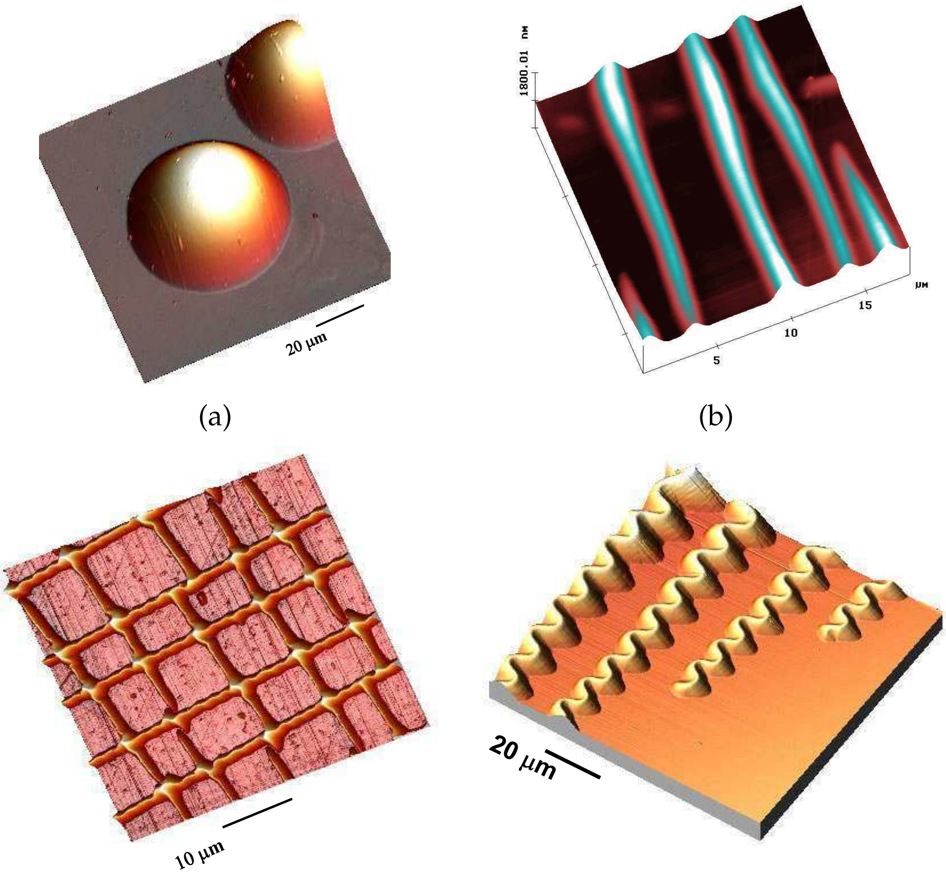

(a) (b) (c) (d)

FIGURE 1: *Examples of buckling delamination structures. (a) Circular blisters – Au(630 nm) on Si. (b) Straight sided blisters – stainless steel. (c) Intersecting blisters – Stainless steel on polycarbonate. (d) Telephone cords blisters –* Y_2O_3*(30-50nm) on GaAs. (Courtesy of C. Coupeau et col., Institut P')*

A growing interest in the study of these mechanical instabilities has emerged during the last decades. In particular, analytical studies based on Föppl von Kármán plate theory have provided valuable insights into the mechanism of formation of straight-sided and circular blisters [48, 49], in the case of elastic thin films on rigid substrates. Later, the finite element method proved to be a valuable tool for the study of buckling-driven delamination of elastic thin films and allowed deeper understanding of the mechanism of formation of telephone cord buckles [31] and highlighted the existing correlation between the film/substrate interface energy and the blister's wavelength. However, the response of ductile thin films deposited on rigid substrates remains an open issue. For instance, it has been evidenced experimentally that the shape of circular blisters observed on gold thin films differs from the sinusoidal form predicted by the elastic model [18]. In particular, the folding angle measured at the basis of the blister is significantly larger in the experimental case compared to the elastic model predictions. Regarding the delamination problem, an interesting point is that some circular blisters can be observed on gold films deposited on silicon substrates, while the analysis of buckle delamination considering linear elastic films predicts that this particular shape is unstable [49].

These differences in morphology and stability are thought to originate from the elastic-plastic response of the film. However, the key features of the mechanisms leading to such morphologies need to be clarified, which is the purpose of the present study.

The purpose of this thesis is thus to:

- generate buckling structures in samples of gold thin films deposited on silicon substrates, study their morphology and characterize the mechanical properties of the thin film,
- develop a model for the buckling driven delamination of ductile thin films deposited on rigid substrate and study the effect of plasticity on the response of the film in the case of straight and circular blisters,
- analyse conditions leading to the formation of the experimentally observed buckles and try to fit their profiles using finite element calculations. Explore how plastic deformation of the film influences the mechanics of blisters propagation, especially their morphological stability during the delamination stage.

This research project has required expertise in the experimental field as well as in the numerical field and gave place to fruitful collaborations between the following research units:

- the group "'Surface, Interfaces et Matériaux sous Contrainte"' of P' Institute in Poitiers where the Au/Si samples were prepared and the buckling structures as well as the residual stresses characterized,
- the group "'Physique du Métal"' of the SIMaP laboratory in Grenoble where nanoindentation tests and finite element simulations were performed.

This thesis contains four different chapters. In the first chapter, we present the context of this research project and provide an overview of some fundamental results in the understanding of the complex mechanisms of buckling-driven delamination. In particular, we introduce the problem of plate buckling and post-buckling and consider the delamination of thin films from their substrate as an application of fracture mechanics at the film/substrate interface (coupled with the plate buckling problem).

In the second chapter, we present an experimental study of the buckling structures observed on gold thin film deposited on silicon substrates. The methods used for residual stress measurement as well as the characterization of the thin film's mechanical properties are presented and the corresponding results are discussed. These results provide important data for the elaboration of elastic-plastic buckling model.

In the third chapter, we present our numerical model for the buckling of ductile thin films and use it to study the effects of plasticity on the morphology of straight and circular blisters. By comparing the simulation results with the experimental observations, we gain a better understanding of the possible conditions that lead to the formation of the blisters observed experimentally. In particular, we study the influence of the loading history on the equilibrium profiles of straight and circular blisters.

In the last chapter, we present a numerical model for the buckling-driven delamination of ductile thin films and use it to study the influence of plasticity on the morphology of straight blisters and on the energy balance of the system during delamination. We also study the influence of other important parameters on the final profile of straight blisters such as the influence of the interface properties, the boundary conditions during the loading and and the loading history. The last part of this chapter is dedicated to the study of the morphological stability of circular blisters in purely elastic and ductile thin films.

In the conclusion of this thesis we discuss the limits of our models and suggest some perspectives that can be pursued in order to improve the buckling-driven delamination model of ductile thin films on rigid substrates.

Chapter 1

State of the art

Contents

The aim of this chapter is to give the reader an overview of some fundamental results in the mechanics of plates and shells as well as fracture mechanics applied to interfacial failure. These results are crucial to understand the complex mechanisms of buckling-driven delamination. Although analytical descriptions are available for the analysis of buckling, numerical model are mandatory when buckling and delamination are considered.

This chapter contains three main sections: In the first section, Föppl von Kármán plate theory is used to study the elastic buckling of elastic thin films in the case of straight and circular buckles. In the second section, we recall the main results from the literature concerning the study of of cracks and especially interface cracks. We complete this section with a description of cohesive models which will be applied to describe interface cracking. In the third section, we combine Föppl von Kármán plate theory with interfacial crack propagation to study buckling-driven delamination of thin films.

1.1 Elastic buckling of thin films

Elasticity is defined as the ability of a deformed material body to return to its original shape and size when the forces causing the deformation are removed. On general basis, most objects that undergo elastic deformation exhibit small deformations and can thus be described by a linear relation between the stress and strain.[63, 101] Conditions are entirely different if those objects undergo large displacements that alter significantly their initial shapes. The linear elastic model thus does no longer apply and it becomes necessary to consider a non-linear relation between the applied stress and the resultant strain. The buckling of beams and thin films is an example of non-linear response.[101] However, it is due to large displacements (geometric non-linearity) rather than to material behaviour (material non-linearity).

In many cases, the damage of a thin film submitted to compressive stresses may be attributed to an elastic instability (buckling). Studying the buckling of thin films and plates is thus of great practical importance as it helps determine the critical buckling load (i.e the load at which the film buckles) and the corresponding buckling configuration of equilibrium.

In order to model the elastic buckling of thin films, we use the formalism introduced by A.Föppl [36] and then T.von Kármán [56]at the beginning of the 20th century. This approach has been lately applied to model the buckling-driven delamination of thin films in the work of J. W. Hutchinson and Z. Suo [48].

1.1.1 Straight buckling of elastic thin films

We consider an isotropic and elastic thin film of thickness h, deposited on a rigid substrate. Its elastic properties are given by E and ν, its Young's modulus and Poisson's ratio respectively. The film is assumed to be free from the substrate along a region of width $2b$ and clamped along its edges. The film, initially unbuckled and in a state of equilibrium, is subject to a uniform equi-biaxial compressive in-plane stress, $\sigma_{xx} = \sigma_{yy} = -\sigma$.

Under the assumption $h << b$, the film is represented by a wide, clamped Euler column of width $2b$. If we take into account the invariance of the equilibrium state along the x-axis, the problem can be considered as two-dimensional. The full geometry of the problem is presented in figure 1.1.

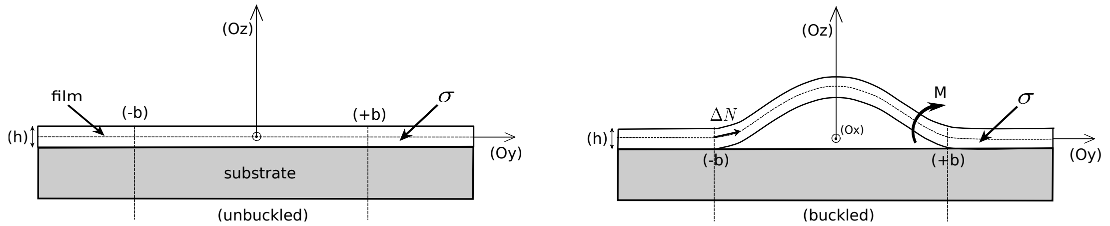

FIGURE 1.1: *Geometry and conventions of the one-dimensional blister.* ΔN *and* M *are respectively the resultant stress and the bending moment. left: unbuckled state; right: buckled state and local loading on the film.*

The deformation of the plate is characterized by its y- and z- displacement, v and w. The system can be characterized by Föppl von Kármán (FvK) plate theory with fully clamped conditions at its edges:

$$v = w = \frac{\partial w}{\partial y} = 0, \text{ for } y = \pm b \tag{1.1}$$

The general form of the governing differential equation of a geometrically non-linear plate ensures moment equilibrium and is given by the following set of equations in Cartesian coordinates system:

$$\begin{cases} \dfrac{\partial N_x}{\partial x} + \dfrac{\partial N_{xy}}{\partial y} = 0 \\ \\ \dfrac{\partial N_{yx}}{\partial x} + \dfrac{\partial N_y}{\partial y} = 0 \\ \\ D(\dfrac{\partial^4 w}{\partial x^4} + 2\dfrac{\partial^4 w}{\partial x^2 \partial y^2} + \dfrac{\partial^4 w}{\partial y^4}) = N_x \dfrac{\partial^2 w}{\partial x^2} + 2N_{xy}\dfrac{\partial^2 w}{\partial x \partial y} + N_y \dfrac{\partial^2 w}{\partial y^2} \end{cases} \tag{1.2}$$

where N_x, N_y and N_{xy} are the internal forces acting in the mid surface of the film. The changes in the resultant stresses with respect to the initial state are given by $\Delta N_x = N_x + \sigma h$, $\Delta N_y = N_y + \sigma h$ and $\Delta N_{xy} = N_{xy} + \sigma h$. $D = Eh^3/(12(1-\nu^2))$ is called the bending stiffness or the flexural rigidity of the film. It should be noted that the bending moment is related to the bending strain by $M_y = D\frac{\partial^2 w}{\partial y^2}$.

Under the assumption of the invariance of the equilibrium state along the x-axis, the problem takes a simpler form:

$$\begin{cases} \dfrac{\partial \Delta N_y}{\partial y} = 0 \Rightarrow \Delta N_y = cste = \Delta N \\ \\ D\dfrac{\partial^4 w}{\partial y^4} - N_y \dfrac{\partial^2 w}{\partial y^2} = 0 \Rightarrow D\dfrac{\partial^4 w}{\partial y^4} - (\Delta N - \sigma h)\dfrac{\partial^2 w}{\partial y^2} = 0 \end{cases} \tag{1.3}$$

In general, such a problem has only one solution corresponding to the initial flat configuration of equilibrium (i.e $w = 0$). However, the magnitude of N_x in the differential equation depends on the prescribed in-plane external load σ. We can find values of these loads for which non-trival solutions are possible. The minimum load allowing for such a non-trivial solution is called the critical load.

To solve the equation, we start first by applying Hooke's Law. Considering the non-variance of the solution along the x-axis, we establish the following equation:

$$\begin{cases} \epsilon_y = \dfrac{\partial v}{\partial y} + \frac{1}{2}(\dfrac{\partial w}{\partial y})^2 = (1-\nu^2)\frac{\Delta N_y}{Eh} \\ \\ \epsilon_x = 0 \rightarrow \Delta N_x = \nu \Delta N_y \end{cases} \tag{1.4}$$

Then, the resolution of Eq.1.4 yields:

$$\begin{cases} w = \frac{1}{2}\delta\left(1+\cos\left(\frac{\pi y}{b}\right)\right) & (1.5)\\ M = M_y(b) = \frac{\pi^2}{2}\frac{Dh}{b^2}\delta & (1.6)\\ \frac{\sigma h - \Delta N}{D} = \frac{\pi^2}{b^2} & (1.7)\end{cases}$$

Eq.1.7 gives the value of the residual stress that is constant in the delaminated part of the straight sided blister according to Eq.1.3. It is equal to its critical buckling stress σ_c.

$$\sigma_c = \frac{\sigma h - \Delta N}{h} = \frac{\pi^2 D}{b^2 h} = \frac{\pi^2}{12}\frac{E}{(1-\nu^2)}\left(\frac{h}{b}\right)^2 \tag{1.8}$$

By integrating Eq.1.4 between $x = -b$ and $x = b$, using the deflection given by Eq.1.5 and the boundary conditions given by $v(-b) = v(b) = 0$, we obtain the following expression of ΔN as well as the relation between the maximum out-of plane displacement δ and the loading ration $\frac{\sigma}{\sigma_c}$ of the straight sided blister.

$$\begin{cases} \Delta N = \frac{3\pi^2}{4}\frac{D}{b^2}\delta^2 & (1.9)\\ \delta = h\sqrt{\frac{4}{3}\left(\frac{\sigma}{\sigma_c}-1\right)} & (1.10)\end{cases}$$

The nonlinear nature of the post-buckling solution is expressed through the square root dependency of the blister amplitude with respect to the loading in Eq.1.10, which is typical from spercritical bifurcations.

1.1.2 Circular buckling of elastic thin films

In this part, the case of one-dimensional blister is generalised to the axisymmetric case corresponding to a circular blister. In this approach, we follow quite freely the method developed in the following references [48, 101, 106]. As in the previous case, we consider an elastic thin film assumed to be isotropic with Young's modulus E, Poisson's ratio ν and thickness h, deposited on a hard substrate. The film is submitted to an in-plane equi-biaxial compressive stress implying $\sigma_r = -\sigma_0$. The geometry is similar to the one presented previously except that a circular interface crack of radius R exists on the interface between the film and the substrate. The full geometry of the problem is presented in figure 1.2.

For such an axisymmetric problem, it is more convenient to use the polar coordinates r and ϕ rather than Cartesian coordinates.

$$x = r\cos(\phi),\ y = r\sin(\phi),\ r^2 = x^2 + y^2 \ and\ \phi = \tan^{-1}\left(\frac{y}{x}\right) \tag{1.11}$$

We use the relations between the Cartesian and the polar coordinates (eq. 1.11) to adapt the governing equation of plate buckling (eq.1.2), derived for a rectangular plate, to a circular plate.

Thus, in the case of axi-symmetrically loaded circular plate, Föppl von Kármán equation takes the following form.

$$\begin{cases} \vec{div}(\bar{\bar{N}}) = \vec{0}, \text{ with } \bar{\bar{N}} = \begin{pmatrix} N_{rr} & N_{r\theta} \\ N_{r\theta} & N_{\theta\theta} \end{pmatrix} & (1.12) \\ \frac{\mathrm{d}^4 w}{\mathrm{d}r^4} + \frac{2}{r}\frac{\mathrm{d}^3 w}{\mathrm{d}r^3} - \frac{1}{r^2}\frac{\mathrm{d}^2 w}{\mathrm{d}r^2} + \frac{1}{r^3}\frac{\mathrm{d}w}{\mathrm{d}r} = \frac{-\sigma h}{D}\left[\frac{\mathrm{d}^2 w}{\mathrm{d}r^2} + \frac{1}{r^2}\frac{\mathrm{d}w}{\mathrm{d}r}\right] & (1.13) \end{cases}$$

We can note that the dimension of the quantity $\frac{\sigma h}{D}$ is $\frac{1}{L^2}$. By introducing the following dimensionless variable $\rho = r\sqrt{\frac{\sigma h}{D}}$ and rearranging the terms, we can re-write equation 1.13 as following [1]

$$\frac{\mathrm{d}^4 w}{\mathrm{d}\rho^4} + \frac{2}{\rho}\frac{\mathrm{d}^3 w}{\mathrm{d}\rho^3} + (1 - \frac{1}{\rho^2})\frac{\mathrm{d}^2 w}{\mathrm{d}\rho^2} + \frac{1}{\rho}(1 + \frac{1}{\rho^2})\frac{\mathrm{d}w}{\mathrm{d}\rho} = 0. \tag{1.14}$$

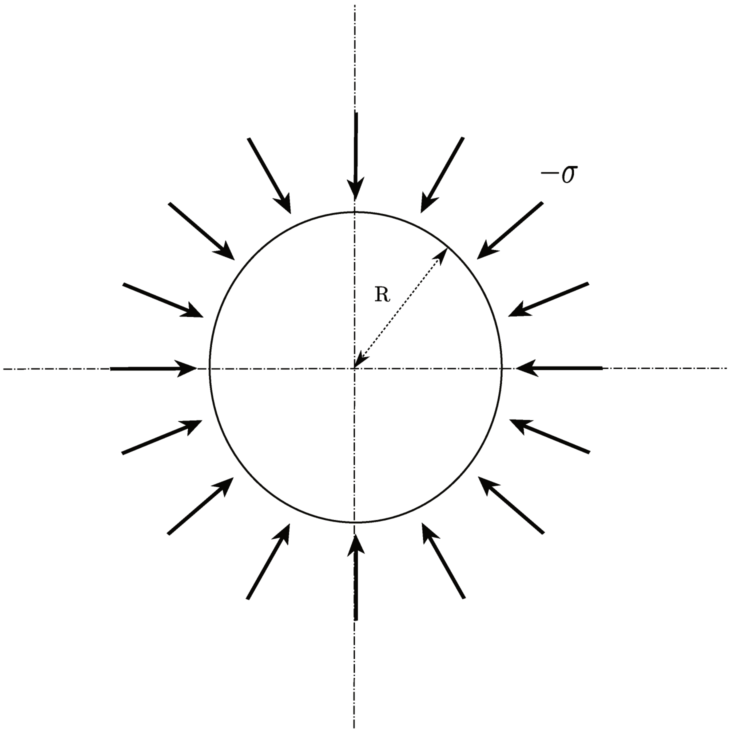

FIGURE 1.2: *Geometry and conventions of the circular blister.*

Equation 1.14 can be written as follow

$$[\rho w''(\rho)]'' - [(\frac{1}{\rho} - \rho)w'(\rho)]' = 0. \tag{1.15}$$

---

[1] An alternative method to using fourth order Bessel type equations, consists of introducing the variable $\phi = \frac{\mathrm{d}w}{\mathrm{d}\rho}$ and integrating once the equation 1.14.
By taking into account the fully clamped conditions, we obtain the following differential equation which is fully solved and explained in [101]

$$\rho^2\frac{\mathrm{d}^2\phi}{\mathrm{d}\rho^2} + \rho\frac{\mathrm{d}\phi}{\mathrm{d}\rho} + (\rho^2 - 1)\phi = 0.$$

This is a fourth order Bessel type homogeneous differential equations. Its has a general solution of the form [19].

$$w(\rho) = C_1 + C_2 \ln(\rho) + C_3 J_0(\rho) + C_4 Y_0(\rho) \tag{1.16}$$

where $J_0(\rho)$ and $Y_0(\rho)$ are ,respectively, the Bessel functions of the first and second kind of zero order [111] and $C_{i,i=(1,\ldots,4)}$ are constants. Since the terms $\ln(\rho)$ and $Y_0(\rho)$ tend towards ∞ when $\rho = 0$ and $w(\rho = 0)$ is finite and equal to the maximum deflection, the constants C_2 and C_4 must be equal to zero which leads to the following form of deflection

$$w(\rho) = C_1 + C_3 J_0(\rho). \tag{1.17}$$

Let $\kappa = \rho(r = R) = R\sqrt{\frac{\sigma h}{D}}$ where R is the radius of the plate. The clamping boundary conditions requires:

$$\begin{cases} w(\rho = \kappa) = 0 \\ \\ \dfrac{\mathrm{d}w}{\mathrm{d}\rho}|_{\rho=\kappa} = 0 \end{cases} \tag{1.18}$$

By deriving equation 1.17 we obtain the slope of the plate mid-surface which is given by

$$\frac{\mathrm{d}w}{\mathrm{d}\rho} = C_3 \frac{\mathrm{d}J_0}{\mathrm{d}\rho}. \tag{1.19}$$

From the Bessel function theory, we have[111]

$$J_1(\rho) = -\frac{\mathrm{d}J_0}{\mathrm{d}\rho}. \tag{1.20}$$

We can thus re-write conditions 1.18 as

$$\begin{cases} C_1 + C_3 J_0(\kappa) = 0 \\ \\ -C_3 J_1(\kappa) = 0 \end{cases} \tag{1.21}$$

A non trivial solution for these equations is $J_1(\kappa) = 0$. The first non-zero solution to this equation [111] is given by $\kappa^* = 3.8317$, which is the first order solution.

Noting that $\kappa^{*2} = \rho^{*2}(r = R) = \sigma\frac{R^2 h}{D}$ and $D = Eh^3/(12(1 - \nu^2))$, we can derive the critical buckling stress in the case of a circular plate σ_c^* as following:

$$\sigma_c^* = \kappa^{*2}\frac{D}{hR^2} = 1.2235\frac{E}{1-\nu^2}(\frac{h}{R})^2 \tag{1.22}$$

In order to have an expression of the associated axisymmetric buckling mode $w_1(\rho)$, we use the first of equations 1.21 to get $C_1 = -C_3 J_0(\kappa^*)$. Reporting this entity in equation 1.17, we get:

$$w_1(\rho) = -C_3(J_0(\kappa^*) - J_0(\rho)) \tag{1.23}$$

The post-critical state has no explicit solution and requires for example an asymptotic analysis [97]. We can normalize the solution so that $w_1(0) = 1$, which leads us to the following expression:

$$w_1(\rho) = \frac{J_0(\kappa^*) - J_0(\rho)}{J_0(\kappa^*) - 1} \tag{1.24}$$

This normalized solution given by equation 1.24 is presented in figure 1.3. The $X-$, $Y-$, and Z-axis origin point has been set at the centre of the bubble's base. We can notice that the solution satisfies well the conditions $w_1(\rho = 0) = 1$ and $w_1(\rho = \kappa^*) = 0$.

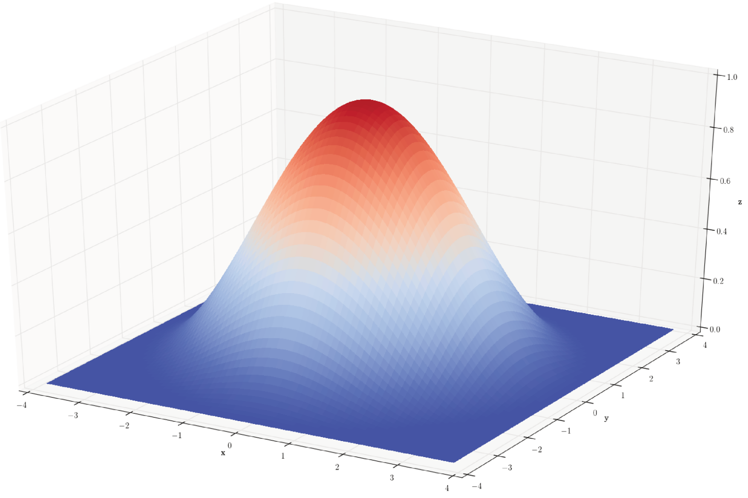

FIGURE 1.3: *Representation of the analytical solution $w_1(\rho)$. The $X-$, $Y-$, and Z-axis origin point has been set at the centre of the bubble's basis.*

1.2 Interfacial fracture cohesive model

1.2.1 Fracture modes

Depending on the loading applied to the crack tip, three opening modes can arise as shown in figure 1.4. Mode I is called the opening mode and corresponds to the application of a tensile stress that is normal to the crack plane. Mode II is called shear mode and corresponds to the application of a shear stress that is acting parallel to the plane of the crack and perpendicular to the crack front. Finally, mode III is called tearing mode and corresponds to the application of a shear stress that is acting parallel to the plane of the crack and parallel to the crack front.

In the case of brittle homogeneous isotropic material, cracks are known to propagate such that pure mode I conditions are maintained at the crack tip, which represents the lowest energy cost. However, in the case of interfacial fracture, the difference in mechanical

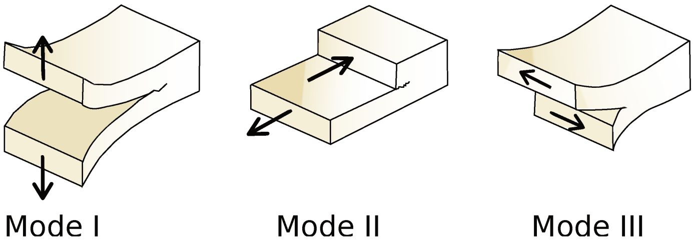

FIGURE 1.4: *The three opening modes for crack propagation. Mode I: opening mode; Mode II: shear mode; Mode III: transverse mode*

properties between the two layers creates an asymmetry that leads to mixed mode propagation of the crack (essentially combination of mode I and mode II). Indeed, as long as the interface represents the least demanding path in term of energy, the crack will be simply trapped in it, even though it is not perpendicular to the loading force.

1.2.2 Dundurs' parameters

As explained above, mode mixity can originate when a crack is laid in between two dissimilar materials. In this paragraph, we consider two isotropic elastic solids joined along the x axis as indicated in figure 1.5 with material 1 above the interface and material 2 below it.

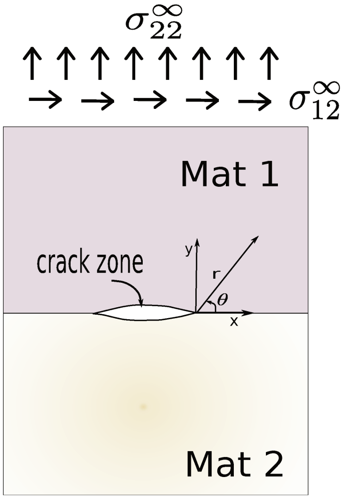

FIGURE 1.5: *Crack at an interface between two materials*

Dundurs has shown that a large variety of plane elasticity problems for bimaterials depend on only two non-dimensional parameters. These parameters are called Dundurs' elastic mismatch parameters and can be written as combinations of the elastic moduli [24, 48]:

$$\alpha = \frac{\mu_1(\kappa_2+1)-\mu_2(\kappa_1+1)}{\mu_1(\kappa_2+1)+\mu_2(\kappa_1+1)} \quad \text{and} \quad \beta = \frac{\mu_1(\kappa_2-1)-\mu_2(\kappa_1-1)}{\mu_1(\kappa_2+1)+\mu_2(\kappa_1+1)} \tag{1.25}$$

with μ_i and ν_i respectively the shear moduli of materials $(i = 1, 2)$, $\kappa_i = 3 - 4\nu_i$ for plane strain and $\kappa_i = \frac{3-\nu_i}{1+\nu_i}$ for plane stress and ν_i the Poisson's ratio for material i. Dundurs' coefficients measure the contrast between the elastic properties of the assembled materials.

They tend towards zero when there is no difference between the two materials and get their signs changed when the two materials are switched. A more explicit way of expressing α is given below:

$$\alpha = \frac{\bar{E}_1 - \bar{E}_2}{\bar{E}_1 + \bar{E}_2}$$

where $\bar{E} = E_i$ in plane stress and $\bar{E}_i = \frac{E_i}{1-\nu_i^2}$ in plane strain, with E_i Young's modulus for material i. The coefficient α tends, thus, toward 1 when the first material is highly rigid compared to the second material and towards zero when both materials are equally rigid.

Under plane strain condition, in the (α, β) plane, the physically admissible values of α and β lie within an enclosed parallelogram defined by $\alpha = \pm 1$ and $\alpha - 4\beta = \pm 1$ (Fig. 1.6). As can be noted, most of the systems exhibit values of beta ranging between 0 and $\alpha/4$.

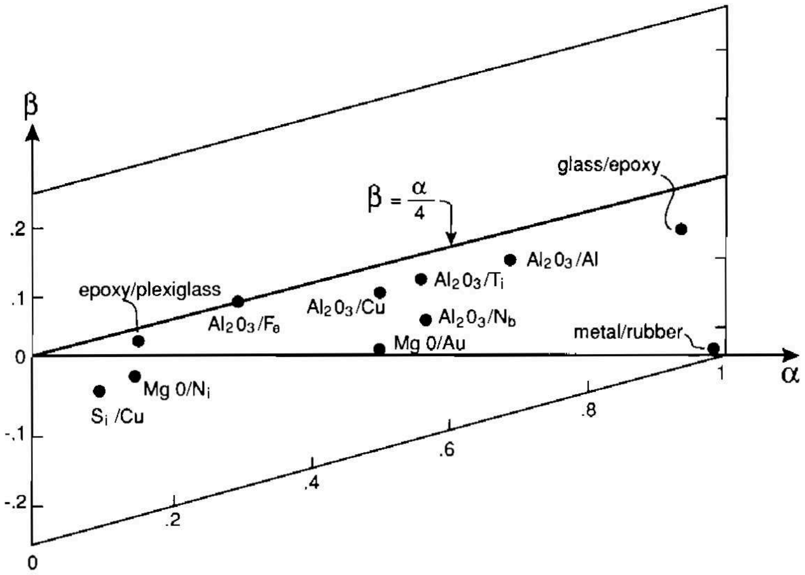

FIGURE 1.6: *Values of Dundurs' parameters in plane strain for some couples of materials, from [48]*

1.2.3 Stress fields at the crack tip

For the sake of clarity, let us first consider the case of an infinitely large linear elastic solid which contains a plane crack , propagating along a straight line. The case of bimaterial will be considered later in this paragraph.

Case of homogeneous materials

Let us consider an infinitely large linear elastic solid with a crack of length $2a$ submitted to a remote tensile loading (Fig. 1.7). E, ν and μ the Young's modulus, Poisson's ratio and shear modulus respectively. The system is described using polar coordinates with the origin at the crack tip as specified figure 1.7.

We assume that during the initiation of fracture, the plastic deformation is localized very close to the crack tip. Solving the equilibrium equation in the framework of linear elasticity

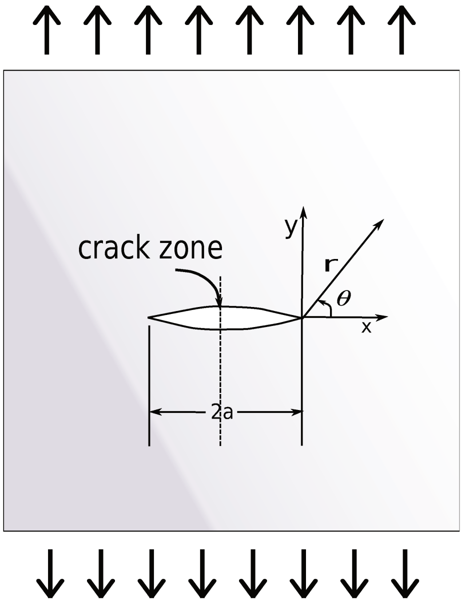

FIGURE 1.7: *Conventions at crack tip in homogeneous material*

leads to a general expression of the displacement and stress fields around the crack tip as presented in [113] and [52]. If applied to the case of a 2-dimensional crack, one obtains the following expression [48, 84]:

$$\begin{cases} u_i = \dfrac{K_I}{2\mu}\sqrt{\dfrac{r}{2\pi}}g_i^I(\theta) + \dfrac{K_{II}}{2\mu}\sqrt{\dfrac{r}{2\pi}}g_i^{II}(\theta) + o(\sqrt{r}) \\ \\ \sigma_{ij} = \dfrac{K_I}{\sqrt{2\pi r}}f_{ij}^I(\theta) + \dfrac{K_I}{\sqrt{2\pi r}}f_{ij}^{II}(\theta) + o(\dfrac{1}{\sqrt{r}}) \end{cases} \tag{1.26}$$

where σ_{ij} is the stress tensor components, u_i the displacement components and the terms $g_i^{I,II}(\theta)$ and $f_{ij}^{I,II}(\theta)$ are dimensionless functions of θ that vary with the load and geometry. The terms K_I et K_{II} are the stress intensity factors for mode I and mode II respectively. These parameters are used to characterize the severity of the stress field at the crack tip caused by a remote load or residual stresses.

The preceding expressions correspond to the first terms of development of Williams series, dominant at the crack tip. The region where these terms dominate is called K-dominance area. We notice that the stress distribution is singular when $r \to 0$ and the crack tip is thus considered as a geometrical singularity. This issue will be reconsidered with cohesive zone model.

Case of interfacial crack

In the case of an interfacial crack, the stress field takes the following form, based on the notations and definitions of [84]:

$$\sigma_{ij} = \frac{1}{\sqrt{2\pi r}}\left(\mathcal{R}e\left(Kr^{i\epsilon}\right)F_{ij}^I(\theta,\epsilon) + \mathcal{I}m\left(Kr^{i\epsilon}\right)F_{ij}^{II}(\theta,\epsilon)\right) \tag{1.27}$$

where $i = \sqrt{-1}$ and $K = K_1 + iK_2$ is the complex stress intensity factor for the interface. The term $r^{i\epsilon}$ is given by $r^{i\epsilon} = \cos(\epsilon \ln r) + i \sin(\epsilon \ln r)$ with ϵ the elastic heterogeneity parameter expressed as a function of the Dundurs' parameter β as follow:

$$\epsilon = \frac{1}{2\pi} \ln \left(\frac{1-\beta}{1+\beta} \right) \tag{1.28}$$

The quantities F^{I}_{ij} and F^{II}_{ij} are specified in [85]. We notice that when $\beta = 0$, $\epsilon = 0$ and K_1, K_2, F^{I}_{ij} and F^{II}_{ij} reduce to the quantities K_I, K_{II}, f^{I}_{ij} and f^{II}_{ij} respectively, as presented in equation 1.26 in the case of homogeneous materials. Thus, in this case K_1 and K_2 play then similar roles to conventional modes I and mode II intensity factors K_I, K_{II} in homogeneous materials, although these parameters should not be identified in general. The singular fields are normalized so that,in the plane containing the interface ($\theta = 0°$):

$$\sigma_{22} + i\sigma_{12} = \frac{K r^{i\epsilon}}{\sqrt{2\pi r}} \tag{1.29}$$

We notice that the terms K_2 and K_1 cannot characterize σ_{22} and σ_{11} independently because of the term $r^{i\epsilon}$. Moreover, the term $r^{i\epsilon}$ brings some complications due to its oscillatory nature that are not present in the elastic homogeneous case. The associated crack opening at a distance r from the crack front can be approximated by $\delta_i = u_i(r, \theta = \pi) - u_i(r, \theta = -\pi)$, which leads to:

$$\delta_2 + i\delta_1 = \frac{8}{(1+2i\epsilon)\cosh(\pi\epsilon)} \frac{(K_1 + iK_2)}{E*} \left(\frac{r}{2\pi} \right)^{1/2} r^{i\epsilon} \tag{1.30}$$

with $\frac{1}{E*} = \frac{1}{2}\left(\frac{1}{E_1} + \frac{1}{E_2} \right)$

1.2.4 Mode dependence of interfacial fracture

As presented in the beginning of section 1.2, in the case of a crack propagating along the interface between two materials, the contrast in the elastic moduli with respect to the interface induces a mode II component. These asymmetries can heavily affect the propagation of the crack and its final equilibrium state. It is thus important to characterize the proportion in which the different modes contribute to the crack opening. To this end, a mode mixity parameter ψ is introduced:

$$\psi = \arctan \left(\frac{\mathcal{I}m\left(K l^{i\epsilon}\right)}{\mathcal{R}e\left(K l^{i\epsilon}\right)} \right) = \mathcal{A}rg(K l^{i\epsilon}) \tag{1.31}$$

with $K = K_1 + iK_2$ the complex stress intensity factor and l a reference length that can be fixed based on specimen geometry considerations (crack size, thickness of the layer...) or material length scale considerations (size of the fracture process zone, plastic zone at fracture...) [48, 92]. The choice stays optional even though for a matter of simplicity it can be preferable to fix l so that, whatever the system is, it stays inside the K-dominance area. The freedom in the choice of l comes from the simple transformation rule that links one choice (l_1 of mode mixity angle ψ_1) to another (l_2 of mode mixity angle ψ_2) [84]:

$$\psi_2 = \psi_1 + \epsilon \ln\left(\frac{l_2}{l_1}\right) \tag{1.32}$$

If l is chosen inside the K-dominance area, the equation 1.29 can be used in order to write another expression equivalent to Eq. 1.31:

$$\psi = \arctan\left(\frac{\sigma_{12}}{\sigma_{22}}\right)_{(r=l,\theta=0°)} \tag{1.33}$$

where $\sigma_{12}(r = l, \theta = 0°)$ and $\sigma_{22}(r = l, \theta = 0°)$ are respectively the shear and normal stress near the crack tip. We notice that if the crack front undergoes pure mode I loading, then $\psi = 0°$ and if it undergoes a pure mode II loading, $\psi = 90°$.

Finally, if $\beta = 0$, the equation 1.33 becomes

$$\psi = \arctan\left(\frac{K_2}{K_1}\right). \tag{1.34}$$

where as mentioned before, the terms K_2 and K_1 in equation 1.34 turn into the classical stress intensity factors K_I and K_{II} defined in the case of homogeneous materials.

Now that we have properly defined the mode mixity parameter, we can look into the dependence of adhesion upon mode mixity. From a thermodynamic point of view, the true work of adhesion W_A of a given interface is the amount of energy required to create new surfaces from the bonded state of two elastic solids, such as a film and its substrate. The true work of adhesion is generally hard to measure as it can be altered by other sources of dissipation such as plasticity around the crack tip. Thus mechanical tests can only provide measurements of interfacial toughness G_c which is larger than W_A and tends towards the true work of adhesion as the dissipated energy is minimized. Among the most used techniques for interfacial toughness measurements, we can cite the double cantilever beam test (DCB) [54], four-point bend test [50, 96] the bulge test [108].

We can find in the literature clear evidences for mode dependence of interfacial toughness at the interface between two solids [59, 102, 110, 112]. In particular, Liechti and Chai [65] considered in their pioneer experiments the case of a glass/epoxy interface (The specimen is represented figure 1.8). The authors have set up an experimental method that enables the measurement of the interfacial toughness G_c for various mode mixity values. They observed that the values of the interfacial toughness reaches its minimum around $\psi = 0°$ i.e pure mode I loading and its maximum when ψ approaches 90° i.e pure shear loading.

Two values of l were chosen: $l_1 = 12,7mm$ associated to values ψ_1 fixed in accordance to the typical dimension of the layers and $l_2 = 127\mu m$ associated to values ψ_2 taken two orders of magnitude smaller than l_1 so that it lays in the K-dominance area. The shift between the two results in term of ψ is approximately of 15°. We can notice that the use of l_2 for ψ calculation places the origin of the ψ_2 axis (i.e. $\psi_2 = 0$) at the minimum of G_c and roughly centres the data, although a slight asymmetry remains in the $G_c(\psi_2)$ function.

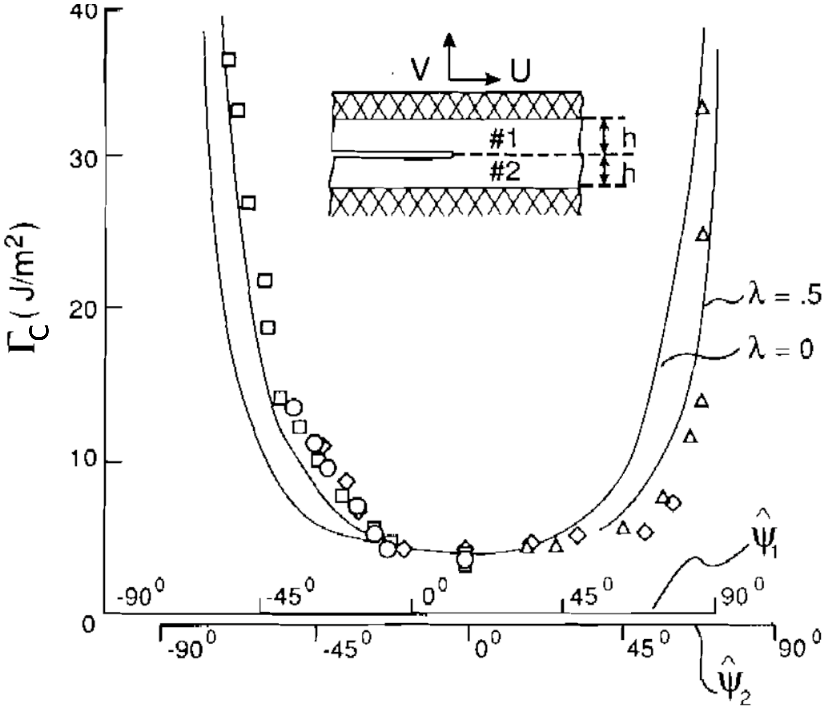

FIGURE 1.8: *Data from [65] for an epoxy ♯1 / glass ♯2 interface:* ψ_1 *axis is obtained using* $l_1 = 12,7mm$ *and* ψ_2 *using* $l_2 = 127\mu m$*. The solid curves represent* $G_c(\psi_2)$ *as given by equation 1.35*

Based on experimental results, phenomenological laws have been proposed to account for the mode mixity dependence of adhesion. Among the most widely used, we can cite the one used in [48]. It uses a symmetrical function with respect to $\psi = 0$ to correct the value of mode I toughness G_{Ic}.

$$G_c(\psi) = G_{Ic} f(\psi) = G_{Ic}\left(1 + \tan^2(\eta\psi)\right) \tag{1.35}$$

where η is determined by $G_c(\frac{\pi}{2}) = G_{IIc}$.

The origin of the mode mixity of interfacial toughness is to a large extend dependent of the assembly under consideration (polymer on metal, metal on metal etc.. ..) and a unified or unique description could not yet meet general agreement. However experimental work involving two solids bonded by a thin adhesive layer where at least one is ductile [28, 65, 100] showed a marked dependence of the toughness upon mode mixity and suggested the importance of the role played by plasticity in this effect. Numerical studies using finite elements [99] gave evidence that the increase of roughness observed with increasing proportion of mode II to mode I is due to the extension of plastic deformation outside of the fracture process zone. Later, plastic flow models allowed an accurate assessment of the plasticity contribution to interface fracture resistance in thin-film interconnect structures ($Cu/TaN/SiO_2$) [64].

1.2.5 Cohesive zone model

The concept of cohesive zone model was first introduced by Dugdale [23] and Barenblatt [5] in the framework of their research on elastic-plastic fracture in metals. In cohesive-zone models, the surfaces of the material facing each other at the crack tip are no longer assumed stress free as it is the case in linear elastic fracture mechanics. They are on the contrary assumed to interact with each other. This interaction is referred to as 'cohesive law' and links the interaction forces (traction), to the relative distance between the two surfaces referred to as 'separation'. This approach is appropriate when studying the initiation and propagation of cracks, whether the crack initiates within the bulk of a given material or at the interface between two materials. For the sake of simplicity, we name the surfaces on both sides of the crack path, surface 1 and surface 2, whether the crack occurs within a given material or at the interface between two materials. The process of crack initiation and propagation can be decomposed into the following stages:

- Stage 1: The two surfaces, surface 1 and surface 2 are perfectly bonded. The mechanical response at the interface corresponds to that of the bulk material (elastic, plastic, visco-plastic ...) and the displacement fields are continuous across the interface.
- Stage 2: This stage corresponds to the initiation of the crack: For a maximum traction locally, the onset of debonding takes place with progressive decay in the traction with increasing separation.
- Stage 3: In this stage the opening reaches the critical value δ_{cr} for which the traction vanishes. There is no more interaction between the two surfaces and the separation is thus completed.

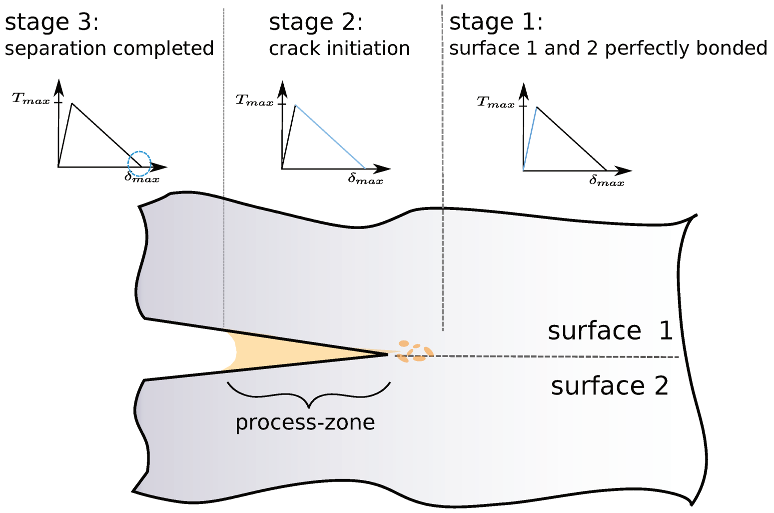

FIGURE 1.9: *Schematic illustration of the different stages of crack initiation and growth in cohesive zone model.*

These stages are illustrated along with an example of bi-linear traction separation law in figure 1.9.

The specific stages of a traction separation law depends on the physical fracture mechanisms at the microscopic scale as illustrated in figure 1.10.

The traction opening profile mimics mechanically the failure process. Therefore, various profiles can be identified depending on the opening mechanism. These laws are generally under the form $\vec{T} = f(\vec{\delta})$, where $\vec{\delta}$ is the opening and $\vec{T}$ the traction. It should be noted that this law can be specified for normal and shear modes by considering the normal and tangential components of the traction and the opening vectors specified in equation 1.36.

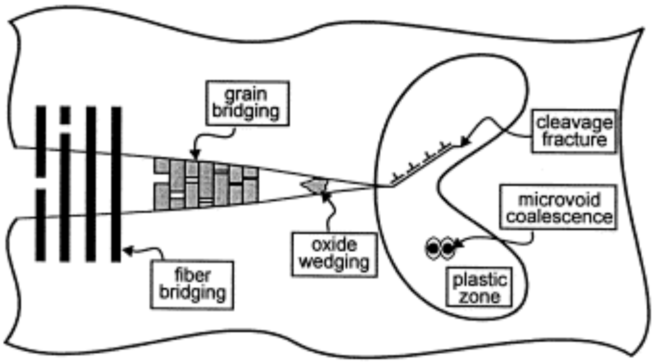

FIGURE 1.10: *Schematic illustration of several physical mechanisms occurring in materials during crack growth. from [86]*

$$\vec{T} = \begin{pmatrix} T_n \\ T_t \end{pmatrix} \quad , \vec{\delta} = \begin{pmatrix} \delta_n \\ \delta_t \end{pmatrix} \tag{1.36}$$

where n and t stand respectively for normal and shear components. Among the most used cohesive laws, we enumerate the following: cubic polynomial law [103], trapezoidal [104], smoothed trapezoidal [91], exponential [75], linear softening [9] and bilinear softening[79, 115]. These laws are depicted in figure 1.11. The x-axis corresponds to normalizes opening δ/δ_c where δ_c is the critical opening. The y-axis corresponds to normalized traction T/T_{max} where T_{max} is the maximum traction.

For each of these cohesive laws, the cohesive energy G_c is defined as the energy per unit surface that is dissipated during the fracture process and corresponds in Fig. 1.11 to the area underneath the function $f(\delta)$. In the case of linear elastic mechanics, it can be defined as follow

$$G_c = \int_0^{\delta_{cr}} \vec{T}.d\vec{\delta} = \underbrace{\int_0^{\delta_{cr}^n} T_n.d\delta_n}_{G_{Ic}} + \underbrace{\int_0^{\delta_{cr}^t} T_t.d\delta_t}_{G_{IIc}} \tag{1.37}$$

1.3 Simultaneous buckling and delamination of thin films

In section 1.1, we have established a post-buckling solution in the case of straight and circular blisters respectively. This solution is valid as long as the edges of the blisters are assumed

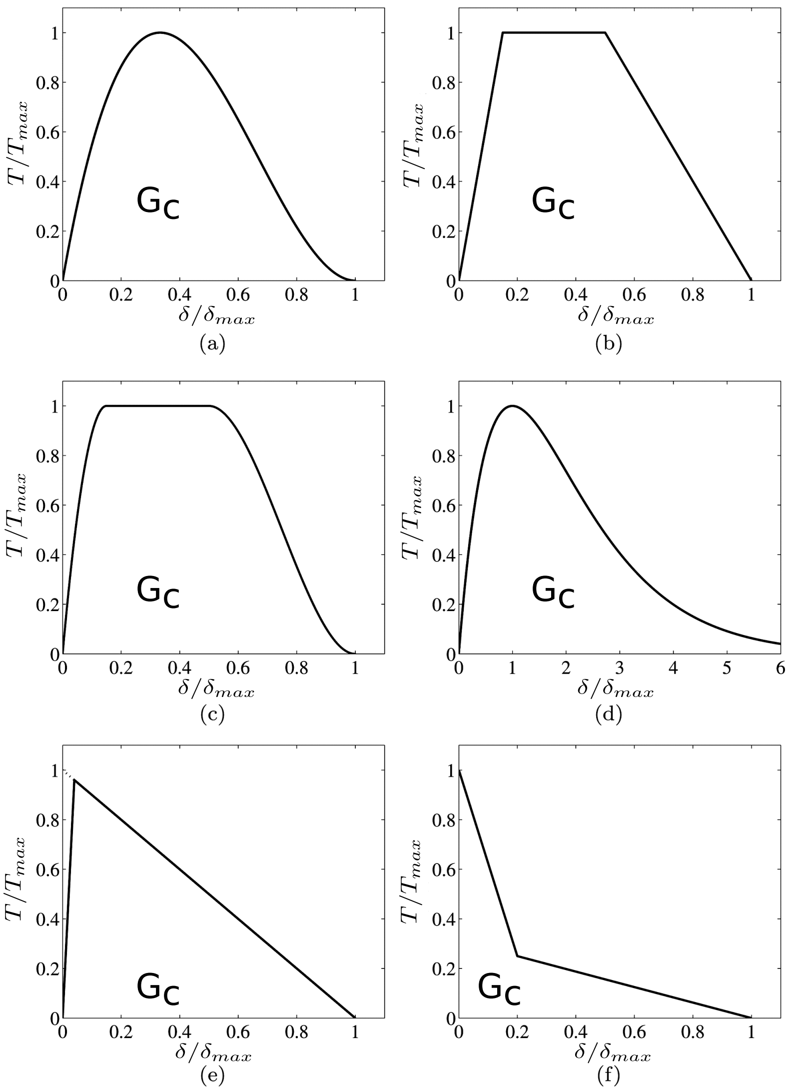

FIGURE 1.11: *Example of traction-separation laws: (a) cubic polynomial, (b) trapezoidal, (c) smooth trapezoidal, (d)exponential, (e) linear softening, a,d (f) bilinear softening. from [77]*

to be perfectly clamped to a rigid substrate. However, in the case of a possible delamination along the interface, blister edges can be considered as a crack front and are prone to evolve. To study the stability of the crack front, we need to consider the variation of the elastic energy (E_e) spent during the propagation of a crack of surface A. This entity is called the energy release rate and can be expressed as follow.

$$G = -\frac{dE_e}{dA} \tag{1.38}$$

The Griffith criterion states that the crack front is stable as long as the energy release rate G is lower or equal to the interfacial toughness G_c [45] ($G < G_c$).

1.3.1 Growth and destabilization of straight blisters

In the case of straight blisters, the value of the energy release rate G can be calculated as a function of σ and σ_c [48].

$$G = \frac{1}{2}\frac{(1-\nu^2)}{E}h(\sigma-\sigma_c)(\sigma+\sigma_c) \tag{1.39}$$

G reaches its maximum for a loading ratio $\frac{\sigma}{\sigma_c} = 3$. It is convenient to introduce the elastic strain energy per unit area in the film G_0:

$$G_0 = \frac{(1-\nu^2)h}{2E}\sigma^2 \tag{1.40}$$

The normalized energy release rate is thus given by:

$$\frac{G}{G_0} = \left(1-\frac{\sigma_c}{\sigma}\right)\left(1+3\frac{\sigma_c}{\sigma}\right) \tag{1.41}$$

G_0 can be seen as the maximum energy per unit surface that can be available to break the interface when released.

Case of brittle interface

Under the assumption of a perfectly brittle interface, G_c is constant and does not change as the crack front propagates. We can plot the ratio $\frac{G}{G_c}$ as a function of the width of the blister b using equations 1.8 and 1.39 (see fig.1.12).

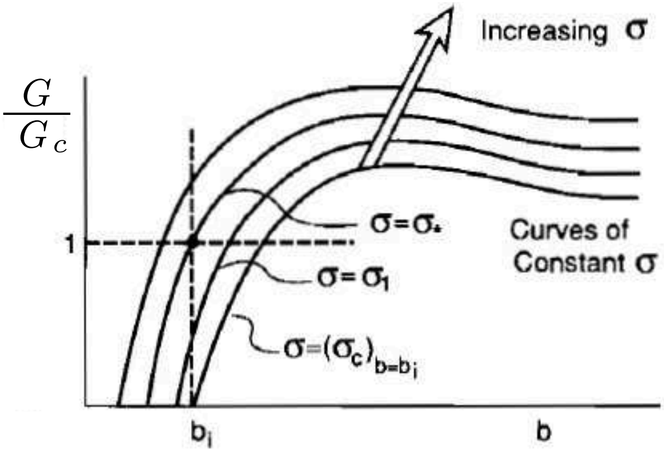

FIGURE 1.12: *Evolution of the ratio $\frac{G}{G_c}$ during straight blister's propagation based on an ideally brittle interface, from [48]*

We notice that for an initially debonded area of width $2b_i$, once the internal stresses are high enough, and the ratio $\frac{G}{G_c}$ reaches the value 1, the propagation of the crack front starts and doe not stop as the ratio $\frac{G}{G_c}$ increases and stays higher than 1 during the propagation. This result is not in agreement with the experimental observations that clearly state a stable equilibrium at the crack front. To avoid this dissonance, a mode mixity dependence of the interfacial toughness needs to be taken into account.

Case of mode mixity dependent interface fracture

In the case of the buckling-driven delamination of a straight blister, the crack front is submitted to a mixed mode I and mode II loading [48]. It is then important to define the proportion in which mode II contributes to the crack tip opening compared to mode I during the propagation of the crack front. To do so, we use the mode mixity angle parameter ψ as derived in [48]:

$$\tan(\psi) = \frac{\sqrt{12}M\cos(\omega) + h\Delta N\sin(\omega)}{-\sqrt{12}M\sin(\omega) + h\Delta N\cos(\omega)} \tag{1.42}$$

where ω is a non-dimensional coefficient depending on Dundur's parameters α and β, and M and ΔN are the moment per unit length and the change in resultant stress at the crack front respectively (see figure 1.1). Figure 1.13 shows curves of ω as a function of α for two different values of β, $\beta = 0$ and $\beta = \frac{\alpha}{4}$ for a thin film on an infinite substrate. We notice that if the same material is taken for the film and for the substrate i.e $\alpha = \beta = 0$ then $\omega \simeq 52°$. Another important value of ω corresponds to the case where $\beta = 0$ (This choice greatly simplifies crack tip fields as explained in 1.2.3) and $\alpha = -1$ which corresponds to an infinitely rigid substrate which leads to $\omega \simeq 45°$.

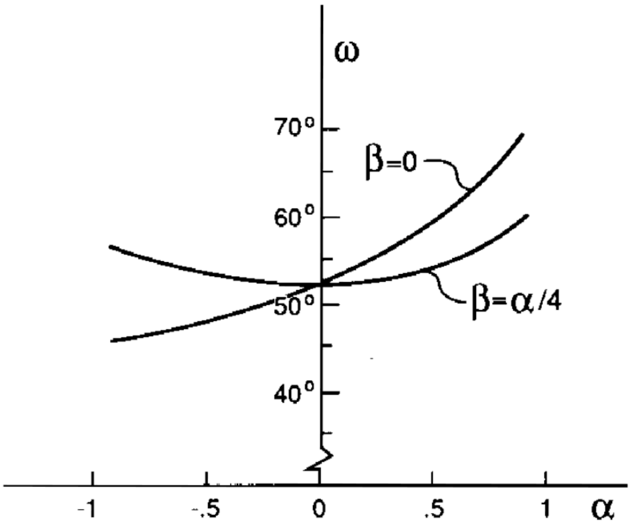

FIGURE 1.13: *Curves of $\omega = \omega(\alpha, \beta)$, from [48]*

By replacing ΔN et M by their literal expressions given by equations 1.9 and 1.6 respectively in equation 1.42 , we obtain:

$$\tan(\psi) = \frac{4\cos(\omega) + \sqrt{3}\frac{\delta}{h}\sin(\omega)}{-4\sin(\omega) + \sqrt{3}\frac{\delta}{h}\cos(\omega)} = \frac{2\cos(\omega) + \sqrt{\frac{\sigma}{\sigma_c} - 1}\sin(\omega)}{-2\sin(\omega) + \sqrt{\frac{\sigma}{\sigma_c} - 1}\cos(\omega)} \tag{1.43}$$

Figure 1.14 shows the evolution of ψ as a function of $\frac{\sigma}{\sigma_c}$. It is important to note that as the crack propagates i.e b increases, σ_c decreases (equation 1.10) and thus $\frac{\sigma}{\sigma_c}$ increases (the loading being maintained constant during the propagation of the blister) leading to an increase in the quantity $|\psi|$. The previous reasoning leads to the conclusion that the proportion of mode II to mode I increases as the crack propagates and so does the interfacial toughness (refer equation 1.35: $G_c(\psi) = G_{Ic}\left(1 + \tan^2(\eta\psi)\right))$

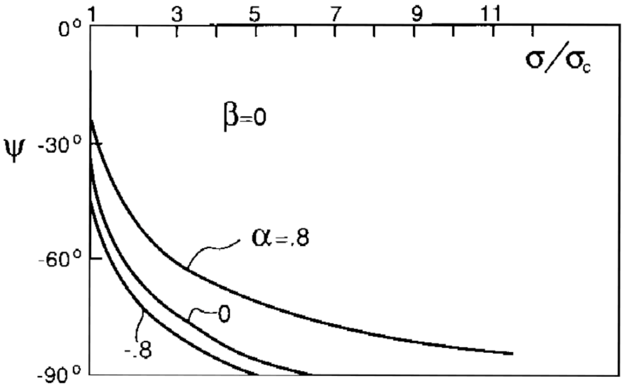

FIGURE 1.14: *Mixed mode angle at the crack tip as a function of the normalized stress σ/σ_c, from [48]*

This increase in the interfacial toughness G_c along with the blister's propagation is sufficient to reverse the tendency of the curve $\frac{G}{G_c}$ and make the propagation of the blister stop reaching its final half-width b_* as shown in figure 1.15.

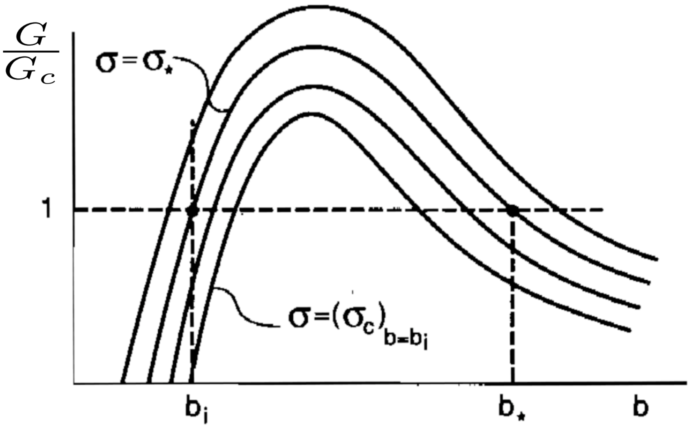

FIGURE 1.15: *, Evolution of the ratio $\frac{G}{G_c}$ during straight blister's propagation based on mode mixity dependent toughness, from [48]*

This example highlights the strong coupling between buckling and adhesion in thin films delamination and makes mode mixity dependence a necessary condition to explain why the blister reaches an equilibrium state.

Destabilization of straight blisters

It has been observed in literature that straight blisters (primary buckling), can destabilize into secondary buckling structures such as telephone cord blisters which are among the most commonly observed buckling structures [15, 42, 70, 71, 72]. An example of the transition of the straight to telephone cord morphology is presented in figure 1.16.

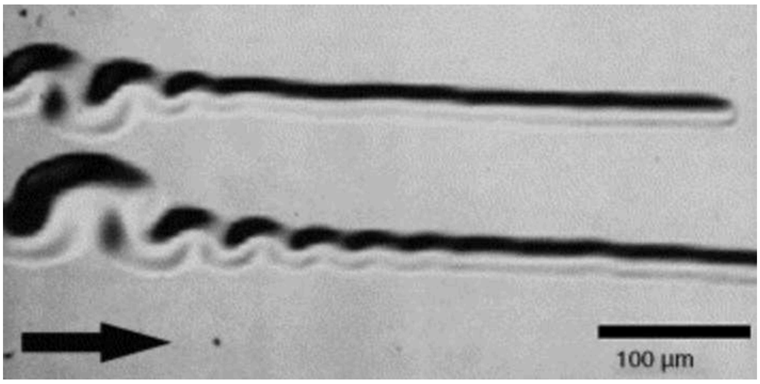

FIGURE 1.16: *Buckling structures formed on a 300 nm tungsten film. Straight buckles formed initially from left to right (direction of arrow). The straight blisters widened initially until destabilizing into telephone cord morphology [15]*

In the previous paragraphs, the calculations concerning buckling-driven delamination were performed by assuming the stability of the initial buckling configuration. To test the stability of such configuration, Audoly performed in [4] a linear stability analysis of the Euler column solution, taking into account the longitudinal compression that remains present after Euler buckling: $\sigma_{xx} = -(1-\nu)\sigma_0$ (see figure 1.1 for geometrical conventions). This residual stress was found to induce a secondary buckling of the Euler column under certain conditions. The stability analysis was performed by introducing a small perturbation that is harmonic in the x-direction near the Euler solution. Lateral growth of the pre-existing blister was allowed. Symmetric and antisymmetric modes in the y-direction have been sought independently for different values of Poisson's ratio ν.

The analysis showed that above a critical width of the buckle b_c, the secondary critical buckling stress (associated to the secondary buckling) becomes smaller than σ_0 causing the destabilization of the straight blister. In particular, for low Poisson's ratios ($\nu < \nu_c$ where ν_c is determined numerically to be 0.255 ± 0.001), the most unstable mode is symmetric and takes the form of varicose, while for $\nu > \nu_c$, telephone cord formation is more likely to happen. It should be noted that the destabilization of the Euler column can result from the lateral growth of the blister as well as from the increase of compressive stress due to the similarity of their effect on the ratio $\frac{\sigma_0}{\sigma_c}$.

In most experiments however, telephone-cord blisters do not result from the destabilization of a pre-existing, infinite, straight blister: they wave as they spread forward. Recently, Faou et al. provided numerically in [31] an explanation of the propagation mechanism of telephone cord blister. They highlighted in particular the importance of the coupling between instability and mode mixity dependent adhesion in the formation of the wavy morphology. Although very interesting, these results will not be further discussed as they are beyond the scope of this study.

1.3.2 Growth and configurational stability of circular blisters

In a similar approach to that presented in subsection 1.3.1, we consider in this subsection the case of an elastic film deposited on an infinitely rigid substrate. The film is initially debonded over a circular region of radius R_0. The origin of polar coordinates is considered to be at the centre of this region. In the adherent part ($r > R_0$), the interface behaviour is governed by a mode mixity dependent toughness G_c as presented in equation 1.35. When the film is subjected to compressive stress of amplitude σ, and if $\sigma > \sigma_c$, the film buckles and propagates if the energy release rate G satisfies Griffith criterion $G \geq G_c$. The energy release rate can be derived using the moment and resultant stress change quantities in the unbuckled area of the film and can be expressed as a function the elastic properties of the film, σ_0 and σ_c as following [49]:

$$G = \frac{(1-\nu)c_1}{E} h(\sigma - \sigma_c)(\sigma + \sigma_c) \tag{1.44}$$

where E is Young's modulus, ν Poisson's ratio, h the thickness of the film and $c_1 = [1 + 0.9021(1-\nu)]^{-1}$. During the propagation of the circular blister, the energy release rate G given in equation 1.39 increases monotonically with increasing radius r. However, $|\psi|$ also increases with increasing r which causes $G_c(\psi)$ to increase. As a result of this competition, the blister reaches an equilibrium point for which $\frac{G}{G_c}(b) = 1$ and the radial expansion stops. This phenomenon has already been explained in the case of propagation of straight blister and is illustrated by figure 1.15.

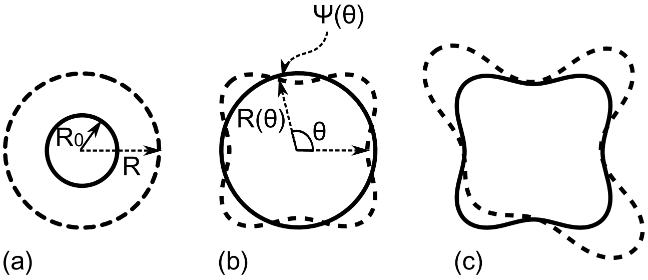

FIGURE 1.17: (a) Growth of a circular defect. (b) Destabilization of a circular defect. (c) Growth of destabilized crack fronts.

The above-mentioned approach, used the hypothesis of a stable static circular shape which is not consistent with the observed destabilization of circular blisters [30, 49]. The mechanism of destabilization of a circular blisters has been first studied by Hutchinson et al. in [49] and is very similar to the mechanism of destabilization of straight blisters. In figure 1.17, we have an example of the destabilization of a circular blister into 4 lobes ($n = 4$).

The authors studied the sensitivity of the circular crack front to harmonic perturbation of the form $R(\theta) = R(1+\epsilon\cos(n\theta))$. This perturbation introduces n lobes and has the amplitude ϵ. The authors then studied the distribution of crack driving force along the crack front to determine whether the perturbation is stable or not. The expression of the ratio $\frac{G}{G_c(\psi)}$ for a

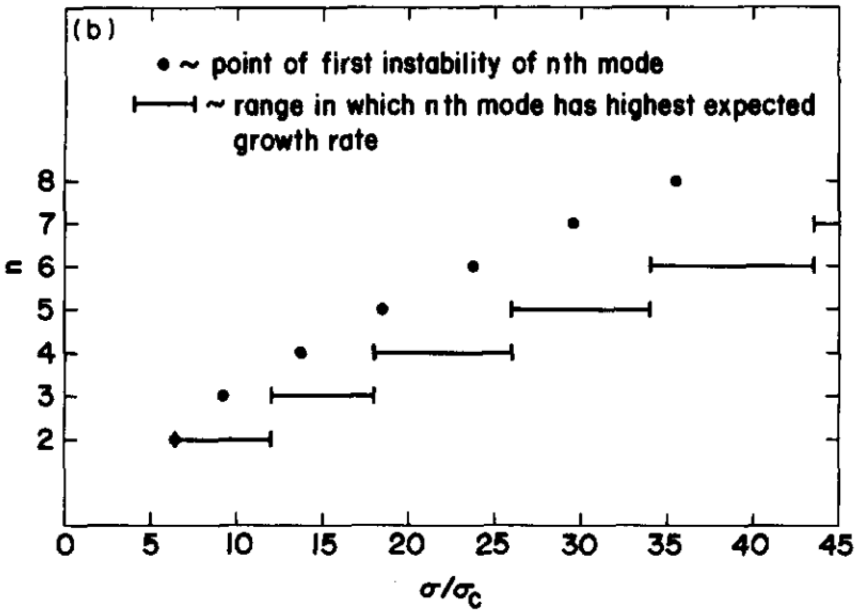

FIGURE 1.18: destabilization of circular blister: Number of lobes as a function of the loading ratio $\frac{\sigma_0}{\sigma_c}$ for $\eta = 1$ and $\nu = \frac{1}{3}$

given perturbation is given by equation 1.45.

$$F = \frac{G}{f(\psi)} = F_0(\frac{\sigma_0}{\sigma_c}) + \epsilon F_1(\frac{\sigma_0}{\sigma_c}, n)\cos(n\theta) \tag{1.45}$$

where $f(\psi) = 1 + (\tan(\eta\psi))^2$, F_0 is the value of F in the axisymmetric state and F_1 is the Fourier coefficient associated with the n^{th} order perturbation. The stability with respect to a perturbation of the crack front with a given n depends on the sign of F_1. Let us first notice that the outward lobes are associated with $\cos(n\theta) = 1$ whereas the inward depressions are obtained for $\cos(n\theta) = -1$. Hence if $F_1 < 0$, G will be smaller at outward lobes than at depressions and the crack will resume its circular shape as it expands. This is a stable configuration. On the other hand, if $F_1 > 0$, G will be higher at outward lobes than at inner depressions, leading the lobes to develop faster whereas the inner depressions linger back. This is an unstable configuration.

The study showed that for a given loading ratio $\frac{\sigma_0}{\sigma_c}$ and mode mixity dependence coefficient η, the circular blister destabilizes for a unique mode n. typically, the first non-axisymmetric instability occurs for $n = 2$ with $\eta = 1$ and the ratio $\frac{\sigma_0}{\sigma_c}$ in the range $5 - 9$. As $\frac{\sigma_0}{\sigma_c}$ increases, instability occurs with higher modes. Figure 1.18 summarizes the different destabilization modes as a function of the ratio $\frac{\sigma_0}{\sigma_c}$ for $\eta = 1$.

1.4 Conclusion

This chapter gathers the most important results and tools when it comes to studying the buckling driven-delamination of elastic thin films on rigid substrates. In section 1.1, we reviewed the elastic buckling of thin films and highlighted the non-linear aspect of the solution due to large out-of-plane displacements. We provided the buckling solution for both straight and circular cases which are the cases of interest in this research work that are studied numerically in the frame of elastic-plastic behaviour in chapter 3.

In section 1.2, we presented some fundamental concepts of fracture mechanics at interfaces including fracture modes, Dundur's parameters and the expression of stress fields at the crack tip and the definition of a parameter defining the mode mixity of the loading. We closed the section by introducing the concept of cohesive zone model and the traction-separation constitutive law which is an important ingredient in the implementation of our buckling-driven delamination model.

Finally, we presented the analytical model for the coupling between buckling and delamination and discussed the stability of linear buckling solution (straight sided and circular blisters). We introduced the phenomenon of secondary buckling (destabilization of primary buckling) and highlighted the importance of mode mixity dependence of the interfacial toughness on the final buckling shape for both straight and circular blisters. These results serve as benchmark when presenting the model of buckling-driven delamination of elastic-plastic thin films in chapter 4 and discussing the corresponding results.

Chapter 2

Questions raised by experiments

Contents

Various observations of gold thin film deposited by sputtering on Si(100) substrates have been carried out [18] and showed unusual shapes of buckling structures. It has been evidenced that such buckling structures can not be explained in the framework of continuum elasticity. Elastic-plastic behaviour of the film and damage are invoked as possible explanations for the unusual blister profiles. Moreover, up to date, no study has considered in details the effect of an elastic-plastic behaviour on the buckling of thin films.

In this chapter, we will present two experimental buckling shapes that motivated the implementation of the finite element model accounting for an elastic-plastic response of the film presented in section 3.1.2. The first example concerns the case of a straight buckle observed in the context of a collaboration with Dr. Coupeau, from P' Institute. The second case is a circular buckling structure as presented in [18]. In the first part of this chapter, we present the methodology used for the deposition of the thin film. Then, we present the results of the mechanical characterization of the thin film and the measurement of the residual stresses resulting from the deposition process. Finally, these observations are discussed in the last part of this chapter and questions about the role of the plastic behaviour of the thin film during the buckling process are raised.

2.1 Experimental observations of buckling structures in ductile thin films

In this section, we will present two different experimental buckling profiles: straight and circular blisters. The observations on circular buckles were made before this PhD, but were never analysed within a complete mechanical framework. For the sake of simplicity, we will refer to the sample corresponding to the straight blister as sample α and that corresponding to the circular blister as sample γ.

2.1.1 Deposition and characterization of the thin film

Deposition technique

In both samples, gold films were deposited by magnetron sputtering on a (100) silicon wafer. The gold film thickness is 400 nm for sample α and $630\,\mathrm{nm}$ for sample γ. Magnetron sputtering is a plasma coating process [73] in which positively charged ions from the plasma (Ar^{+}) are accelerated by the magnetic field and used to bombard a target surface (gold target in our case). This ion bombardment is sufficient to dislodge and eject atoms from the target and cause them to condense on a surface placed in front of the target. The presence of the magnetic field helps to trap the plasma and thus maintain a steady bombardment of the source. Figure 2.1 provides a more detailed scheme of the sputtering apparatus. After the deposition, the thickness of the film is characterized using DEKTAK mechanical profilometry.

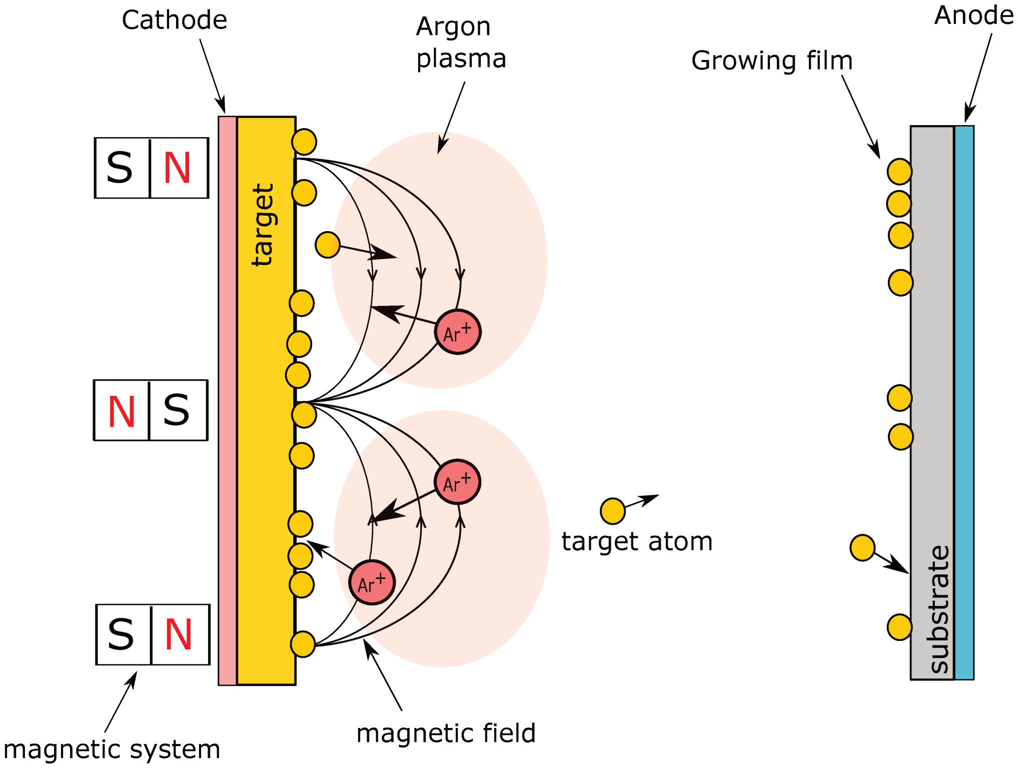

FIGURE 2.1: *Scheme of magnetron sputtering device*

AFM observations

After the deposition process, the samples are removed from the deposition chamber and optical microscopy observations are performed in order to detect the presence of buckled structures. The sample γ naturally showed buckling structures at the end of the deposition process. This is not the case for the sample α. The buckling on the sample α is induced by putting the coated materials in water for a few seconds, which is supposed to alter the adhesion properties. Once the presence of buckling structures confirmed, atomic force microscopy (AFM) with a a vacuum level of 10^{-6} mbar is performed to further investigate and characterize them.

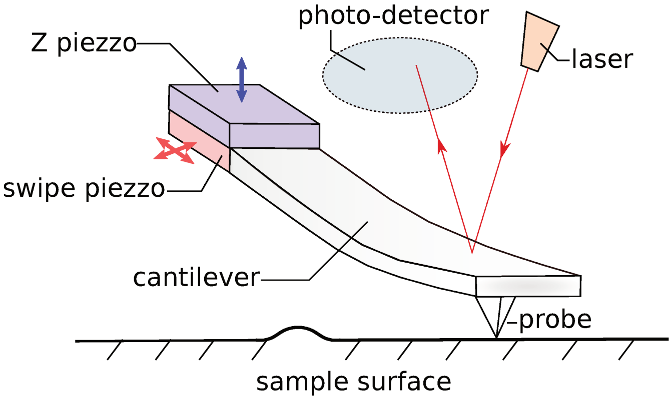

FIGURE 2.2: *Scheme of an atomic force microscope*

The Atomic force microscope operates by scanning the area of interest using a cantilever with a sharp tip at its end (10 nm radius). As the tip approaches the surface, the close-range forces between the atoms at the surface of the sample and the end of the tip cause the cantilever to deflect towards or away from the surface. The AFM apparatus includes a laser source permanently pointed towards the top of the cantilever and a position-sensitive photo-detector to track the reflected beam (from the top of the cantilever). Any small deflections will thus cause a change in the direction of the reflected beam that can be linked to a change in the topography of the surface. Figure 2.2 illustrates the principle of atomic force microscopy.

On the one hand, AFM observations revealed the presence of straight blisters with an atypical profile on sample α. The profile presented in figure 2.3 shows a stretched shape that does not match the sinusoidal form predicted for an elastic blister as described in equation 1.7. On the other hand, AFM observations of the sample γ showed the presence of circular buckling structures with a strong bending at its circumference (figure 2.4 from [18]). As both observations concerned a thin film known for its ductility (gold), we can formulate the hypothesis that these behaviours might be due to the plastic behaviour of gold thin films. To confirm this hypothesis, an assessment of both the stress levels involved in the buckling process as well as the elastic-plastic response of the thin film is necessary.

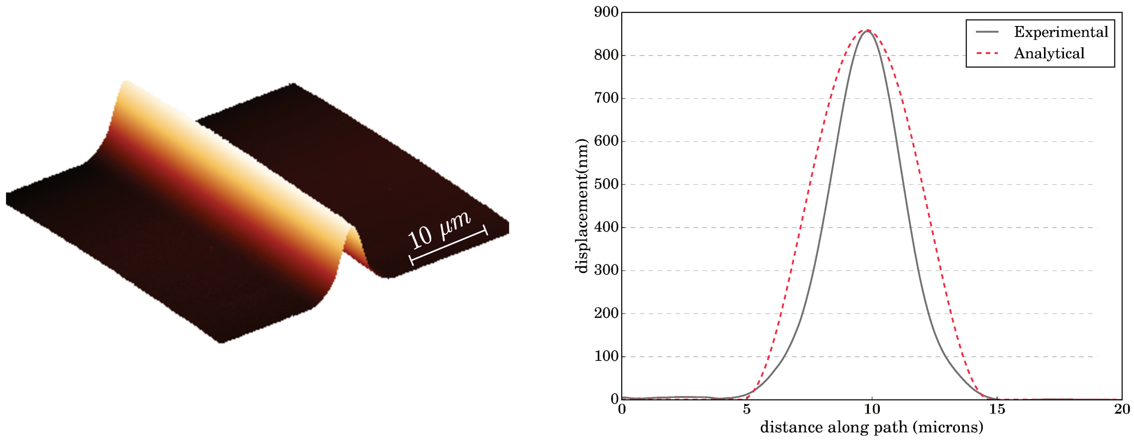

FIGURE 2.3: *Straight blister structure observed in gold film,* 400 nm *thick, deposited on silicon wafer. The profile of the experimental straight blister is plotted along with the usual sinusoidal shape predicted in the frame of elastic buckling.*

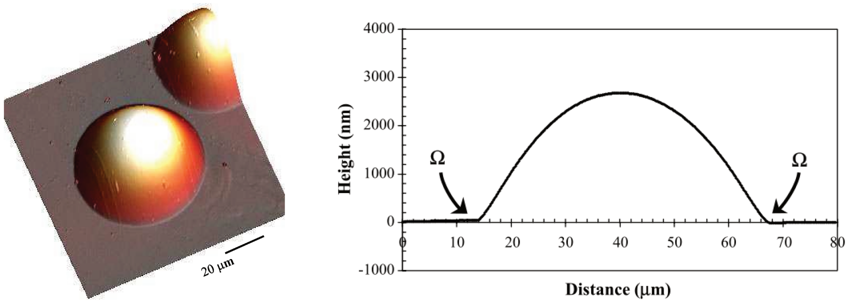

FIGURE 2.4: *Buckling structure observed in gold film,* 630 nm *thick, deposited on silicon substrate.A marked bending* Ω *of the buckling structure is observed at the base of the circular blister.*[18]

2.2 Characterization of the mechanical properties of the thin film

Due to the increasingly small thickness of new coatings, conventional techniques such as tensile or hardness tests fail to offer practical and reliable assessments of the mechanical properties of thin films. The growing need for a characterization method suitable for small volumes of materials, has lead to the development of very low-load, depth-sensing indentation technique [22, 67, 80] known as nano-indentation.

During a nano-indentation test, a hard tip whose geometry and mechanical properties are well characterized (typically diamond or sapphire) is pressed into the sample to be tested and a load–displacement (F vs. h) and stiffness-displacement (S vs. h) curves are measured during the loading and unloading. The analysis of this curve allows the estimation of different mechanical properties, including hardness and Young's modulus [74].

Different tips can be used for nano-indentation tests and are generally either pyramidal, conical or spherical. The choice of the tip geometry depends on what material is studied and which mechanical properties are investigated. For instance, three-sided pyramidal geometries such as Berkovich or cube-corner indenters are particularly used to measure the hardness of metallic thin films. This choice can be explained by the fact that three-sided pyramids can have a tip apex manufactured with better precision compared to four-sided Vickers or cone indenters which allows a better precision when it comes to measuring the contact area at small penetration depth. The geometries of Berkovich and cube-corner indenters are detailed in figure 2.5. On the one hand, a Berkovich type indenter has a triangular base and an angle of $65.3°$ between the axis of the pyramid and its faces. On the other hand, a cube corner indenter, as its name implies, is a three-sided pyramidal tip with perpendicular faces like the corner of a cube. It has an angle of $35.3°$ between the centreline and its faces.

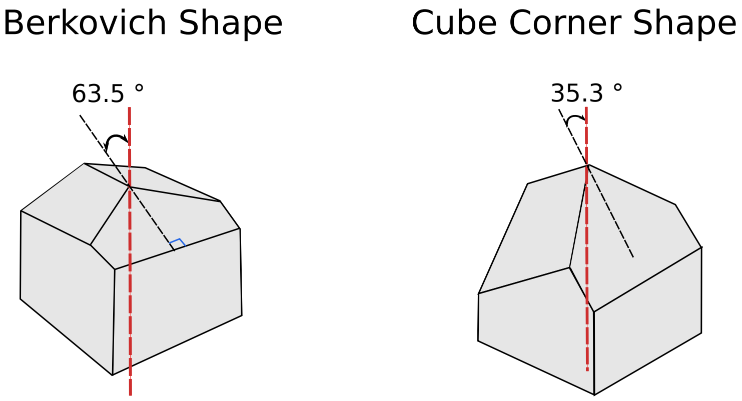

FIGURE 2.5: *Berkovich and cube corner indenter tip geometries*

2.2.1 Nanoindentation analysis method

The nanoindentation technique relies on the analysis of a load-displacement curve recorded during a loading-unloading cycle. During the loading, the load P applied on the sample increases at a given rate until reaching a maximum value P_{max} corresponding to a maximum displacement h_{max}. Then during unloading, the load P decreases until completely vanishing when there is no more contact between the indenter and the sample.

The evolution of the load-displacement curve depends strongly on the material properties. If the material of the sample is supposed perfectly elastic, then the load and unload curves are reversible. However, if it has an elastic-plastic behaviour, then the two curves are distinct and the sample still presents a residual imprint of depth h_f when completely unloaded. The loading-unloading cycle as well as the corresponding load-displacement curve are illustrated in figure 2.6.

At the end of a nanoindentation test, three different parameters can be accessed: the load, the displacement of the tip and the contact stiffness S defined as follow

$$S = \left(\frac{dP_{unloading}}{dh}\right)_{h=h_{max}} \tag{2.1}$$

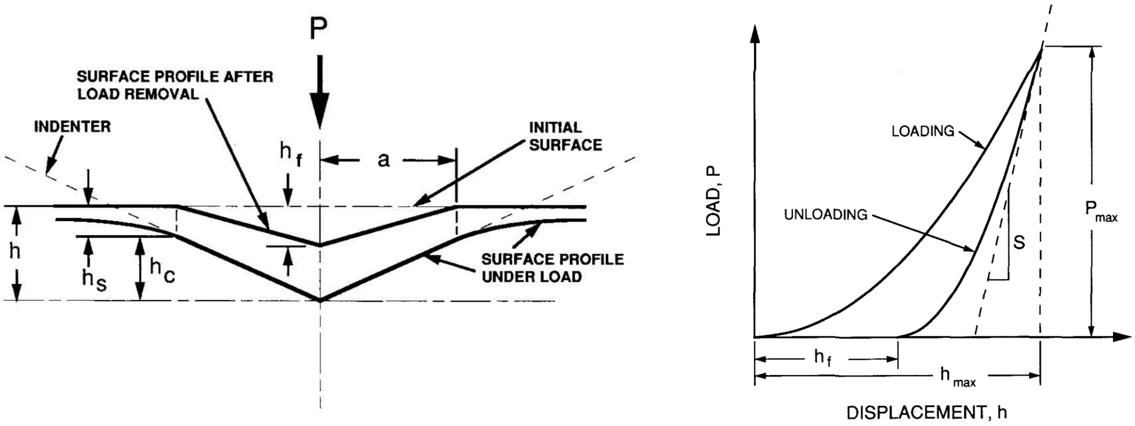

FIGURE 2.6: *(Left) Illustration of an indentation loading-unloading cycle performed by a rigid cone into an elastic-plastic thin film. At a given time during loading: P refers to the applied load, h is to the total displacement into the sample, h_c is the distance along which there is contact between the sample and the indenter (contact depth), h_s is the displacement of the surface at the perimeter of the contact and a is the half width of the contact area. After load removal: h_f is the residual displacement and a is the equivalent contact radius. (right) A schematic representation of a load-displacement curve. From [74]*

The derivation of the elastic properties from the load-displacement curve can be performed using the method developed by W. Oliver and G.Pharr [74] on homogeneous semi-infinite materials. This technique lies on on the work of Sneddon who showed that in many simple indentation problems the load-displacement relationship can be expressed as follow [93]

$$P = \alpha(h - h_f)^m = \alpha(h_c)^m. \tag{2.2}$$

where P, h, h_f and h_c correspond to the convention presented in figure 2.6 and α and m are m are constants that depend on the sample's material and the geometry of the indenter $1.2 \leq m \leq 1.6$ [81].

By differentiating equation 2.2 with respect to h, Sneddon established the following relationship between the contact stiffness S and the projected area of the elastic contact A which showed to be relevant for all axisymmetric indenters [8, 74]

$$S = \frac{2}{\sqrt{\pi}} E_r \sqrt{A_c}. \tag{2.3}$$

where A_c is the contact area and E_r is the reduced modulus defined in equation 2.5. The contact area is related to the equivalent contact radius a_c via the equation

$$a_c = \sqrt{\frac{A_c}{\pi}}. \tag{2.4}$$

The reduced modulus E_r takes into account the effect of non-rigid indenters on the load-displacement response and is defined as follow

$$\frac{1}{E_r} = \frac{1-\nu^2}{E} + \frac{1-\nu_i^2}{E_i}. \tag{2.5}$$

where E and ν are the Young's modulus and the Poisson's ratio of the sample while E_i and ν_i are those of the indenter.

The O. Pharr assumption is a partition of the elastic and plastic displacement and is only valid for materials with large $\frac{\sigma_y}{E}$ ratio. They proposed

$$h_c = h - \epsilon \frac{P}{S} \tag{2.6}$$

with $\epsilon \simeq 0.75$ for a cone indenter.

Thus, the indenter tip geometry can be deduced from calibration on known E material providing $A(h_c)$. Once we have $A(h_c)$, knowing the indentation depth h on the tested material, we can deduce the reduced modulus E_r and thus the Young's modulus of the material E.

The yield stress of the thin film can be approximated roughly using Tabor's relationship between the hardness H and the flow stress σ [95] at maximum load P_{max}:

$$H = 2.8\,\sigma \tag{2.7}$$

The value of the hardness can be determined easily using the value of the load P_{max} and the corresponding projected area of contact A_c. It is defined as

$$H = \frac{P_{max}}{A_c} \tag{2.8}$$

The previous results can be obtained using only one type of indenter, typically a Berkovich indenter. To study the elastic-plastic properties of the film and in particular its strain hardening, Bucaille et. al proposed in [7] a technique that uses two different indenters: Berkovich and cube corner which allow the determination of the flow stress for a chosen representative strain of 3.3% and 12.6% respectively.

2.2.2 Experimental methods

The nano-indentation measurements were performed by Dr. Marc Verdier at the SIMaP laboratory using an XP (MTS) nano-indenter. Two different diamond pyramidal indenters were used: a Berkovich and a cube corner indenter. A continuous stiffness measurement mode was used with a frequency of $45\ Hz$ and a displacement amplitude of $2\,\mathrm{nm}$. During the test, the indenter was loaded at a strain rate of $5 \times 10^{-2}.\ \mathrm{s}^{-1}$ until reaching the substrate. At least 5 tests per sample were performed and only tests with a minimum average drift less than $0.05\,\mathrm{nm\,s^{-1}}$ were retained. A minimum distance of $50\,\mu\mathrm{m}$ between neighbouring indents was maintained to avoid possible interferences. Finally, special attention has been paid to other factors affecting nano-indentation such as initial penetration depth and instrument compliance. The measurements were performed on a sample of $400\,\mathrm{nm}$ gold thin film deposited on silicon substrate (sample α).

The acquisition of the hardness as a function of the normalized contact radius $\frac{a}{t}$ (t is the thickness of the thin film) as well as the calculation of Young's modulus were first performed automatically using the method of Oliver and Pharr [74]. However, since the sample consists of a film deposited on a substrate, a composite behaviour in $E(h)$ and $H(h)$ is expected. It is necessary therefore to measure real A_c using atomic force microscopy. This approach allows the calculation of E and H with better accuracy especially as the material showed pile-up effect.

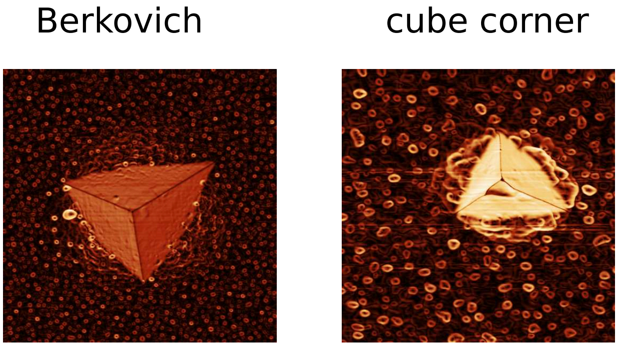

FIGURE 2.7: *AFM micrographs of Berkovich (left) and cube corner (right) residual imprints on* $400\,\mathrm{nm}$ *gold thin film.*

The micrographs presented in figure 2.7 show the residual imprints obtained using the Berkovich and the cube corner indenters. The pile up effect is observed in both micrographs due to the constrained geometry soft film (Au) / hard Si substrate. However it seems more important in the case of cube corner indentation. This observation can be explained by the fact that cube corner indenter has a sharper tip compared to Berkovich indenter which results in more material deformation and thus more pile-up. Finally, we can observe that in the case of cube corner indentation, the imprint reveals a defect in the geometry of the cube corner indenter near the tip. The presence of this defect can influence the calculation of the contact area and thus distort the calculated values of the thin film properties.

2.2.3 Experimental results and discussion

The measurements of hardness and the indentation modulus as a function of normalized equivalent contact radius $\frac{a_c}{t}$ are given in figure 2.8. These results were obtained using the manual measurements of the contact area in both the cases of Berkovich and cube corner indenter geometries.

We can observe that in the case of the indentation modulus, Berkovich and cube corner data points are in good agreement. Only the data points obtained by cube corner indentation at $\frac{a}{t} = 0.5$ seem to be inconsistent. The Young's modulus can be derived from the average modulus curve and is equal to the indentation modulus at the limit $\frac{a}{t} = 0$. It is thus approximately equal to $85\ \mathrm{GPa}$. This value is close to the Young's modulus of bulk gold [39] ($79\,\mathrm{GPa}$) and is comparable to gold thin films' Young's moduli values found in literature.

For example, nano-crystalline gold thin film samples of $10 - 60$ µm thickness and a mean grain size of $26 - 60$ nm exhibited Young's modulus of 73.6 ± 0.6 GPa [90]. Other measurements using X-ray diffraction performed on gold thin films of $560\,\mathrm{nm}$ thickness showed a Young's modulus of 97 ± 10 GPa [33].

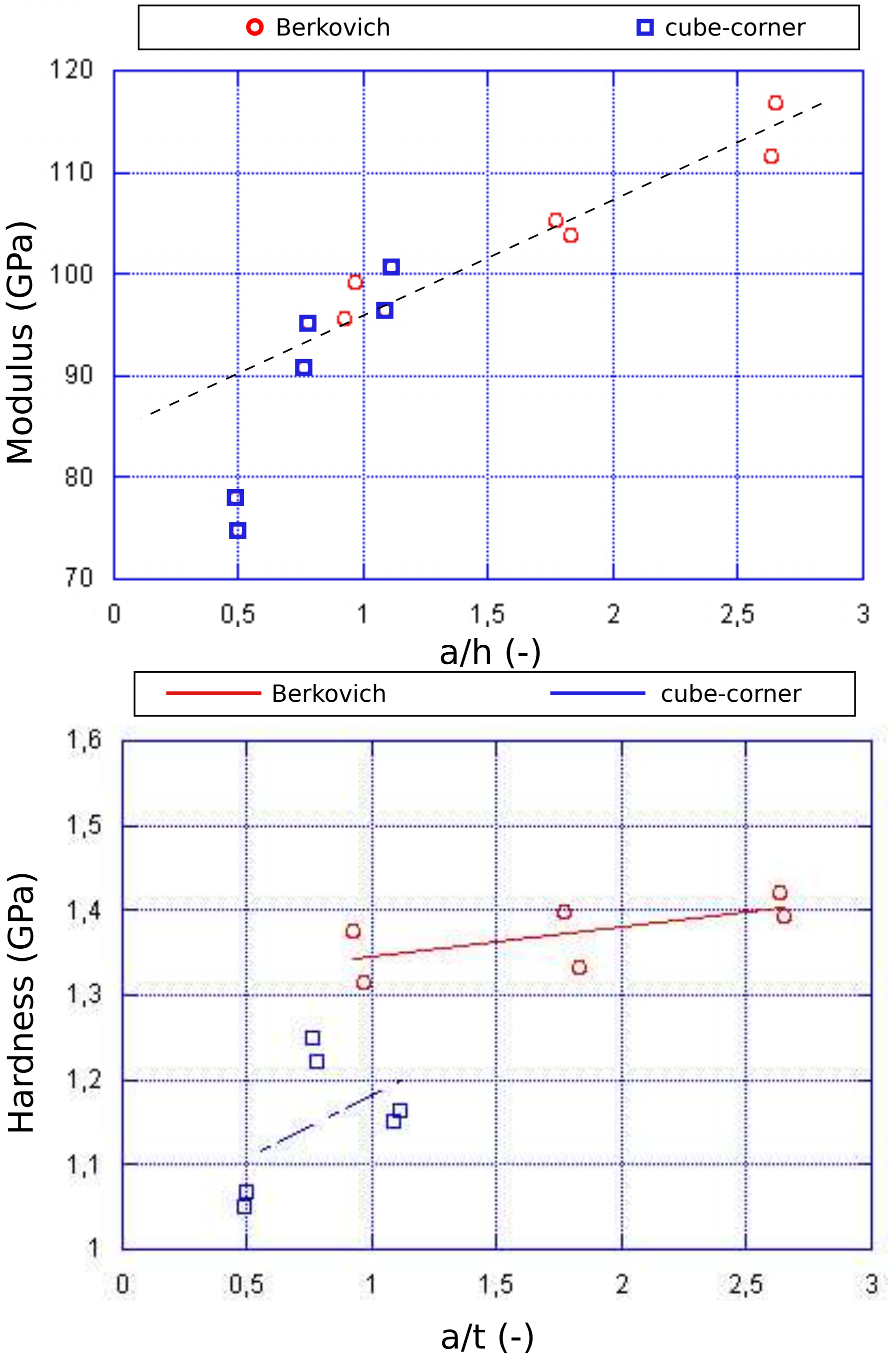

FIGURE 2.8: *Indentation modulus and hardness as function of normalized equivalent contact radius $\frac{a}{t}$ for 400 nm gold thin film deposited on silicon substrate. The red circles correspond to Berkovich indenter data while the blue squares correspond to cube-corner indenter data.*

Concerning the measurements of the hardness as a function of $\frac{a}{t}$, the results of Berkovich geometry indenter and cube corner geometry do not show significant difference and show a small increase in H with $\frac{a}{t}$. This observation means that the gold thin film exhibits small strain hardening between $\epsilon = 3.3\%$ and $\epsilon = 12.6\%$. Indeed, a non self-similar deformation pattern is present in the case of plastic Au film on elastic Si substrate. If the material was perfectly plastic, hardness would have been constant through the thickness. The fact that H increases for both geometries indicate the presence of a small work hardening. Similar results can be found in the literature concerning thin films of $Au - Cu$ alloys [11] and Ni thin films [7]. The yield stress can thus be derived for $400\,\mathrm{nm}$ gold thin film deposited on silicon substrate using Tabor's equation and is estimated to be of the order of few hundred of MPa (400 MPa) at 3.3% strain. Although this value is much higher than the typical yield strength of bulk gold estimated at $30\,\mathrm{MPa}$ at 2% strain, it is consistent with recent studies demonstrating a yield stress of $350\,\mathrm{MPa}$ for $800\,\mathrm{nm}$ gold thin films [27] reaching up to $700\,\mathrm{MPa}$ in the case of $200\,\mathrm{nm}$ gold film [44].

In comparison, the Young's modulus and yield stress measured automatically without manual measurement of the contact area are respectively equal to 140 GPa and 800 MPa.

Considering nano-hardness test results and their consistency with values found in the literature, we chose set the value of Young's modulus E to 85 GPa and considered in our simulations several values of elastic limit σ_y ranging from 400 MPa to 800 MPa. Concerning the strain hardening, we chose to work mainly with small hardening coefficients. In particular, when using linear or Ludwik's law we worked with small hardening modulus typically 50 MPa.

2.3 Stress measurement

Measurement of the residual stresses in the deposited thin films is crucial to ensure a proper understanding of the mechanical conditions that lead to the onset of the buckling structures observed in samples α and γ. Several techniques can be used to measure the stress in thin film : XRD [18, 76, 83], Raman spectroscopy [57] and curvature measurements [94].

2.3.1 Stoney method

Thin films' residual stresses can often be determined using the Stoney formula via the measurements of the substrate curvature. However, the use of this method requires the verification of the following conditions [69]:

- the substrate thickness is thin compared to the in-plane dimensions
- the coating thickness is small compared to the substrate thickness
- the coating and the substrate are homogeneous, isotropic and can be described using linear elasticity
- the film is subject to a homogeneous in-plane stress
- only small deformations and rotations are considered

- the curvature of the substrate mid-plane is considered uniform in all direction (spherical deformation). This is actually a consequence of small deformations and linear elasticity.

Although the required hypotheses are not completely fulfilled, in particular the 3^{rd} one due to the development of plasticity during deposition, we used the Stoney formula presented in equation 2.9 in order to calculate residual stresses in the film. The radius of curvature was measured, before and after coating by a contact profilometer in the full length of the sample.

$$\sigma_i = (\frac{1}{R_2} - \frac{1}{R_1})\frac{E_s}{6(1-\nu_s)}\frac{t_s^2}{t_f} \tag{2.9}$$

where σ_i is the average internal stress in the film, R_1 and R_2 in-plane curvatures of the substrate before and after the coating deposition, t_f the thickness of the film and E_s and ν_s and t_s the Young's modulus and Poisson's ratio respectively.

The calculations using Stoney formula result in a value of residual stresses in compression around 220 MPa for the sample α. To have a suitable point of comparison for this value, we can calculate the critical buckling stress as provided in equation 1.8. We consider the mechanical properties of gold: $E = 85$ GPa and $\nu = 0.44$. The thickness of the film is $h = 400$ nm and the blister's half width is $b \simeq 5\ \mu$m (see figure 2.3). The calculations lead to a critical stress of $\sigma_c = 555$ MPa in the case of sample α (similarly for circular blister, $h = 630$ nm and $b \simeq 27\ \mu$m which gives $\sigma_c = 67$ MPa). Thus in the case of the circular blister(γ), we have $\sigma_0 \approx 7 \times \sigma_c$ which is sufficient to cause buckling. However, in the case of the straight blister (α), we have $\sigma_0 < \sigma_c$, which means that according to Föppl von Kármán plate theory the thin film is not supposed to buckle, if it has a purely elastic behaviour. We decided to check the results using X-ray diffraction tests.

2.3.2 X-ray diffraction

In order to get a second estimation of the stress level involved in the buckling structures, a stress mapping has been carried out on the sample α. X-ray diffraction experiments were conducted by Dr. P.O. Renault, from P' Institute in Poitiers using a SEIFERT diffractometer employing monochromatic $Cu\ K_\alpha$ radiation ($\lambda = 1.54$ Å). The analysis was performed on the $< 111 >$ family of planes by using a punctual beam and rotating the sample α. The analysis revealed that the gold thin film is highly textured in the (111) direction and the compressive residual stresses were found to be around 300 MPa in sample α. These results are consistent with curvature calculations and are nonetheless still intriguing as the residual stresses in the case of the straight blister are not sufficient to cause the buckling of the thin film according to Föppl von Kármán plate theory. This indicates that plastic deformation may have occurred in sample α.

Concerning the sample γ, the residual stresses were found to be around 500 MPa [18] which is sufficient to cause the buckling of the thin film according to Föppl von Kármán plate theory.

2.4 Experimental results discussion

In this section, we have presented two different buckling structures: straight α and circular γ blisters that have been respectively observed in gold thin films of $400\,\mathrm{nm}$ and $630\,\mathrm{nm}$ thickness deposited on silicon substrates (see figure 2.3 and 2.4). For both samples, the residual stresses have been characterized using curvature measurements and DRX-method. The measured residual stresses in the case of the circular blister were demonstrated to be sufficient to cause the buckling of the structure according to elastic analysis ($\sigma_0 = 500$ MPa and $\sigma_c = 67$ MPa). However, this is not the case for the straight blister as the measured residual stresses are significantly lower than the corresponding critical buckling stress ($\sigma_0 = 300$ MPa and $\sigma_c = 515$ MPa).

These results suggest that the whole film went through plastic deformation. Indeed, a small tangent modulus E_0 in the the $\sigma = f(\epsilon)$ relation due to a global plastic deformation causes a loss of bending stiffness which favours buckling by lowering the critical buckling load. The influence of a global plastic deformation of the material on the tangent stiffness is depicted in figure 2.9. In this case, the results concerning the residual stresses in the film should be considered carefully as they are measured after the deposition process and we have no data concerning the stress variation during deposition (i.e we did not perform in-situ stress measurements).

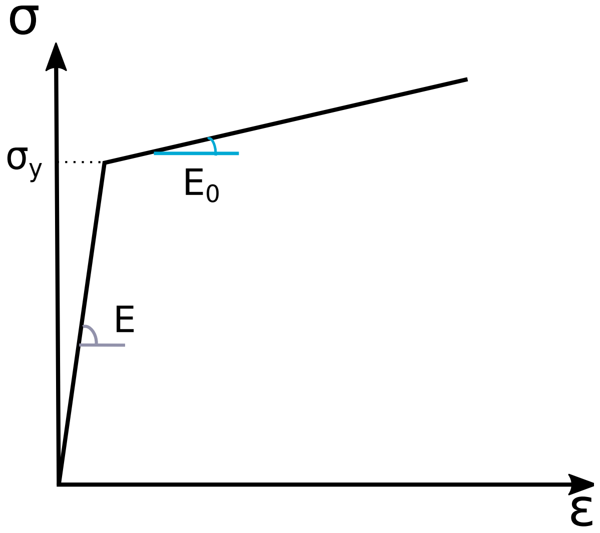

FIGURE 2.9: *Representation of the difference in the tangent modulus between the purely elastic (E) and the plastic (E_0) states.*

We can observe thus that an elastic analysis is not appropriate to predict the onset of buckling in all cases, nor the profile of the blister obtained in the post-buckling regime. Bearing these limitations in mind, we formulated the following hypotheses to interpret the mismatch between analytical predictions and the experimental results

- The buckling at lower values of critical stresses compared to the elastic case is due to a plastic deformation of the whole film [18].

- The history of the loading during the deposition must have allowed such a plastic deformation before reaching the final state [1, 29])
- The properties of the interface between the film and the substrate may also influence the height and morphology of the blister [30].

The first hypothesis can be the cause of the early buckling of the straight blister, as nano-indentation measurements showed a yield stress $\sigma_y = 400\ \mathrm{MPa}$ which is particularly close to the measured residual stresses $\sigma_f = 300\ \mathrm{MPa}$. However considered along with the second hypothesis, plasticity can have a significant impact on the buckling process if the thin film reaches higher compressive stresses during the deposition process.

These hypotheses will first be tested in the frame of elastic-plastic buckling of thin films without delamination in chapter 3. Then in chapter 4, the hypothesis of buckling-driven delamination will be examined along with the effect of the film's plasticity and the loading history.

Chapter 3

Elastic-plastic buckling of thin films

Contents

The aim of this chapter is to study the influence of an elastic-plastic behaviour of thin films on the buckling process of straight and circular blisters in order to gain better insight into the possible mechanisms that lead to the formation of the experimental buckles presented in chapter 2. In the first part of this chapter, we will present the mechanical problem of the buckling of ductile thin films along with its numerical implementation by means of finite element analysis. We will first apply this model to the case of purely elastic buckling and highlight its limits by comparing the simulation results with experimental data. Then we will introduce an elastic-plastic behaviour to the thin film and study the influence of the yield stress on the final morphology of the blister. Finally,we will further develop the study by discussing the importance of the loading history and/or the boundary conditions of the final morphology of the straight and circular blisters.

3.1 Mechanical model

The aim of this section, is to present the mechanical problem of elastic-plastic buckling of a clumped thin film and its numerical implementation. We will particularly focus on the implementation of the following aspects: the geometry and boundary conditions, unilateral contact, elastic-plastic response, loading and resolution method.

3.1.1 Presentation of the mechanical problem

The mechanical system considered here consists of an elastic-plastic thin film deposited on a rigid substrate. The lower part of the film is perfectly bounded to the substrate, except for a strip of the film of width $2b$, that is unbounded (see figure 3.1). The unbounded part of the film is thus able to buckle away from the substrate, once sufficient compressive stress is applied. This problem is highly non-linear, and requires a numerical simulation in order to be solved. There are 3 sources of non-linearity involved:

- Geometric non-linearities due to the large values of the out-of-plane displacement. This type of non-linearity can be accounted for by performing the calculations within the framework of large displacements using the Green Lagrange strain tensor.
- Unilateral buckling, i.e. the equilibrium must satisfy $\omega > 0$ in the whole film domain. This is done by implementing a rigid contact between the film and the substrate.
- The material of the film is elastic-plastic. A plastic deformation based on a J_2 flow theory with isotropic hardening is chosen.

As far as boundary conditions are concerned the film is clamped at its basis ($z = 0$) except for the rectangular unbounded area. In order to generate the isotropic compressive stress ($\sigma_{xx} = \sigma_{yy} = \sigma_0$, with $\sigma_0 < 0$; $\sigma_{xy} = 0$), a thermal strain $\epsilon_0 = \alpha\Delta T$ is applied. Because the total strain is zero due to clamping of the film basis, equibiaxial stresses are generated ($\sigma_{xx} = \sigma_{yy} = \frac{-E}{1-\nu}\alpha\Delta T$, $\sigma_{xy} = 0$ during elastic regime). Note that the thermal strain is mimicking the deposition strain of the film, witch is formally equivalent as far as the mechanical modelling is concerned.

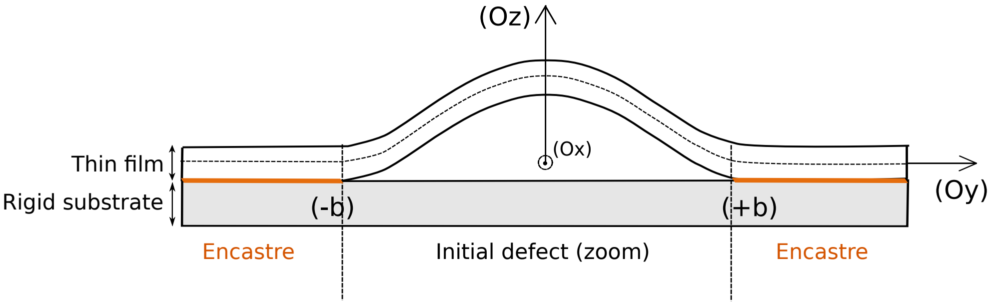

FIGURE 3.1: *Mechanical model for the buckling of a thin film.*

3.1.2 Implementation of the numerical model

In order to solve the problem of the buckling of a ductile thin film on a rigid substrate, we performed FEM calculations using the finite elements code ABAQUS. Various elements have been used : continuum 3D elements and thick shell elements. Although thick shell elements are supposed to handle plasticity, we wanted to compare the results with those obtained using continuum elements with quadratic interpolation, which are supposed to better handle strain localization.

Geometry and boundary conditions

The simulations focused on two different geometries: straight and circular blisters. In the case of straight blister, the geometry is presented in figure 3.2 and consists of a rectangular plate of length $6b$, width b and thickness h. For the thin film, we use solid quadratic elements with 20 nodes located at its vertices and mid-edges. The element size is chosen so that there are at least about 50 elements in the buckle width. Nodes that are part of the lateral edges parallel to x axis as well as the bottom nodes of the film that are in contact with the rigid substrate have fully built-in conditions. For the edges parallel to the y axis, the displacement is only allowed along the z axis and no rotation is allowed around the y and z axis. In the unbounded zone of length $2b$, a very small geometrical defect is introduced to enable the buckling.

The geometry for the circular blister is similar to that of the straight blister except that the unbounded zone is circular of radius R_0 and that the plate has a circular geometry of radius $R = 2R_0$. The nodes of the lateral edge as well as those of the bottom of the film in contact with the rigid substrate are similarly clamped. A similar initial geometrical defect is introduced.

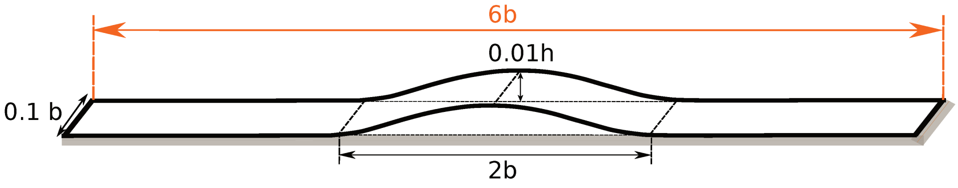

FIGURE 3.2: *Geometry of the straight blister*

Unilateral contact

In order to take into account the presence of an infinitely deep and rigid substrate, we introduce the unilateral contact condition $w(x, y) \geq 0$. This condition is implemented by defining a contact interaction between the surface of a planar rigid substrate and the bottom surface of the film. The interaction is defined as rigid and frictionless to avoid any penetration of the film into the substrate.

Elastic-plastic response

The film is assumed to have an homogeneous elastic-plastic response. In our simulations, we chose to work with a Young's modulus $E = 80\,\mathrm{GPa}$ and a Poisson's ratio $\nu = 0.44$ [33, 51]. The mechanical characterization of the sample α, showed that the film has a yield stress of a few hundred MPa and does not strain harden significantly which is in accordance with literature results [27, 90]. To model the elastic plastic behaviour of the film, we chose to mainly work with a Von Mises criterion along with perfect plasticity or Ludwik law with small hardening rates. The equation of Ludwik hardening is given by:

$$\forall \sigma_{eq} \geq \sigma_y, \sigma_{eq} = \sigma_y + K \left(\epsilon_{eq}^p\right)^n , \tag{3.1}$$

where σ_{eq} is the Von Mises equivalent stress, σ_y is the Yield stress, K is the hardening modulus, ϵ^p_{eq} the equivalent plastic strain and n the strain hardening exponent.

Von Mises equivalent stress σ_{eq} is defined as follow

$$\sigma_{eq} = \sqrt{\frac{3}{2} s_{ij} s_{ij}} \;, \; \bar{\bar{s}} = \bar{\bar{\sigma}} - \frac{1}{3}\mathrm{tr}(\bar{\bar{\sigma}})\bar{\bar{\mathrm{Id}}}, \tag{3.2}$$

where s_{ij} are the components of the stress deviator tensor $\bar{\bar{s}}$ and $\bar{\bar{\sigma}}$ the stress tensor.

The equivalent plastic strain ϵ^p_{eq} is defined as

$$\epsilon^p_{eq} = \sqrt{\frac{2}{3}\epsilon^p_{ij}\epsilon^p_{ij}}. \tag{3.3}$$

where ϵ^p_{ij} are the components of the plastic strain tensor.

Ludwik hardening law is generally suitable for metals ongoing small plastic deformation [60, 68]. In our case, we chose to work with small values of K. Typically, we worked with $K = 50$ MPa and $n = 0.25$. We also performed simulations using a higher hardening modulus $K = 130$ MPa to study the influence of hardening on the buckling response. The elastic-plastic responses that have been tested in the frame of our work are presented in figure 3.3.

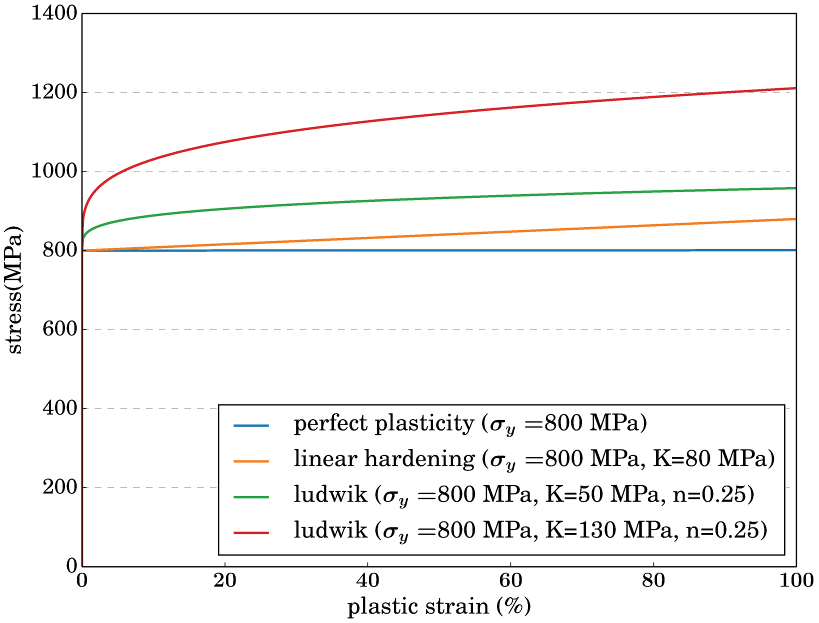

FIGURE 3.3: *Different elastic-plastic responses: Perfect plasticity, linear hardening and Ludwik law with different hardening moduli.*

Loading conditions

The loading consists of an thermal eigenstrain $\epsilon_0 > 0$ applied uniformly to the film via a non-zero expansion coefficient α and an applied change in temperature ΔT. The thermal strain ϵ_0 can be linked to the the applied temperature ΔT:

$$\epsilon_0 = \alpha \Delta T \tag{3.4}$$

For the sake of simplicity, we take $\alpha = 1$, which leads to $\epsilon_0 = \Delta T$. As mentioned before, this is mimicking the deposition strain, which is formally completely equivalent.

Because of the clamped conditions, the total strain in the film ϵ_{tot} remains equal to zero during the loading. It can be decomposed into three components: the elastic strain ϵ_{el}, the plastic strain ϵ_{pl} and the thermal strain ϵ_0 as given in the following equation:

$$\epsilon_{tot} = \epsilon_{el} + \epsilon_{pl} + \epsilon_0 = 0 \tag{3.5}$$

We consider σ_0, the final amplitude of the compressive stress in the unbuckled region of the film, with $\sigma_0 > 0$. Then $\sigma_{xx} = \sigma_{yy} = -\sigma_0$ and $\sigma_{xy} = 0$ in this unbuckled part.

Let us derive the temperature variation ΔT that must be set to have a uniform equibiaxial compression state of amplitude σ_0 in the planar, bounded part of the film, i.e $\sigma_{xx} = \sigma_{yy} = -\sigma_0$. In this case, we have thus $\sigma_{eq} = |\sigma_{xx}| = \sigma_0$.

As long as $\sigma_{eq} < \sigma_y$, we have $\epsilon_{el} + \epsilon_0 = 0$. As $\epsilon_0 = \alpha \Delta T$ and $\sigma_{xx} = -\sigma_0$ we have:

$$\Delta T = \frac{1-\nu}{E}\frac{\sigma_0}{\alpha} \tag{3.6}$$

When $\sigma_{eq} > \sigma_y$, some plastic strain is generated. We have $\epsilon^p_{xx} = \epsilon^p_{yy}$ for symmetry reasons and $\epsilon_{zz} = -2\epsilon^p_{xx}$ because of plastic incompressibility ($\mathrm{tr}(\bar{\bar{\epsilon}}^p) = 0$). In these conditions, $\epsilon^p_{eq} = \sqrt{\frac{2}{3}\epsilon^p_{xx}(1+1+4)} = 2|\epsilon^p_{xx}|$.

Hence, $\epsilon^p_{xx} = -\frac{1}{2}\epsilon^p_{eq} = -\frac{1}{2}\left(\frac{\sigma_{eq}-\sigma_y}{K}\right)^{\frac{1}{n}} = -\frac{1}{2}\left(\frac{\sigma_0-\sigma_y}{K}\right)^{\frac{1}{n}}$.

Because of the clamped type boundary conditions, we have $\epsilon^{el}_{xx} + \epsilon^p_{xx} + \epsilon_0 = 0$. By replacing each of the terms by in the equality by their respective expressions computed above, we obtain:

$$\Delta T = \left(\frac{1-\nu}{E}\frac{\sigma_0}{\alpha}\right) + \frac{1}{2\alpha}\left(\frac{\sigma_0-\sigma_y}{K}\right)^{\frac{1}{n}} \tag{3.7}$$

To sum up:

$$\Delta T = \begin{cases} \frac{1-\nu}{E}\frac{\sigma_0}{\alpha}, & \text{if } \sigma_0 \leq \sigma_y \\ \\ \left(\frac{1-\nu}{E}\frac{\sigma_0}{\alpha}\right) + \frac{1}{2\alpha}\left(\frac{\sigma_0-\sigma_y}{K}\right)^{\frac{1}{n}}, & \text{otherwise} \end{cases} \tag{3.8}$$

Resolution method

Implicit and Explicit are two types of approaches that can be used to solve finite element problems and in particular non-linear problems. In our problem, non-linearities can arise from large-displacement effects (buckling), material non-linearity or also boundary conditions such as contact. The implicit approach uses Newton-Raphson method to solve the non-linear equilibrium equations and has generally the advantage of providing a bigger control on precision of the results than explicit methods. However, when dealing with highly non-linear problems, this method can encounter convergence issues. In the case of buckling problems without delamination, using implicit integration along with small increments ($\frac{\Delta t}{\text{total step time}} \leq 1e-5$) proved sufficient to handle convergence issues with relatively reasonable calculation time when using parallel computing.

3.2 The limits of an elastic model

The aim of this part is to test and understand to which extend it is possible to describe the buckling of ductile thin films using a purely elastic model.

To do so, we use a FEM model that accounts for non-linear geometry as described in section 3.1, to model the buckling structures observed in gold thin film deposited on silicon substrate. A linear elastic constitutive law is assumed for the film. The first case study consists of a circular blister observed on the $630\,\mathrm{nm}$ thick gold thin film referred to as sample γ. The second case study consists of a straight blister observed in a $400\,\mathrm{nm}$ thick gold thin referred to as sample α. Both cases are presented in subsection 2.1.1.

The geometry of the plate is hence chosen to be rectangular in the case α and circular in the case γ. The elastic properties are taken from the characterization of gold thin films (subsection 3.1.2), the geometry such as the thickness of the film (h) and the blister's width ($2b$) are also taken from the experimental observations of samples α (figure 2.3) and γ (figure 2.4). These parameters are summarized in table 3.1.

-	E (GPa)	ν (-)	h (nm)	$2b$ (µm)	σ_0 (MPa)
circular blister (sample γ)	85	0.44	630	53	500
straight blister (sample(α)	85	0.44	400	11	300

TABLE 3.1: *Summary of the gold thin film elastic properties (E: Young's modulus, ν: Poisson's ratio), blisters geometries (h: thin film's thickness, $2b$: blister's diameter) and thin film residual stresses (σ_0) for both samples α and γ*

We have conducted various simulations for both straight and circular blisters using their respective parameters given in table 3.1. The aim is to compare in each case, the experimental profile to the one predicted by the FEM calculation. The results are presented in figure 3.4.

We recall that in the experimental case of the circular blister (γ), the residual stress is estimated to be around $500\,\mathrm{MPa}$ and the buckle has a maximum deflection of approximately $2500\,\mathrm{nm}$. Numerical predictions obtained using identical initial stress values ($500\,\mathrm{MPa}$) show significantly lower buckling profiles (figure 3.4) with a maximum deflection of roughly

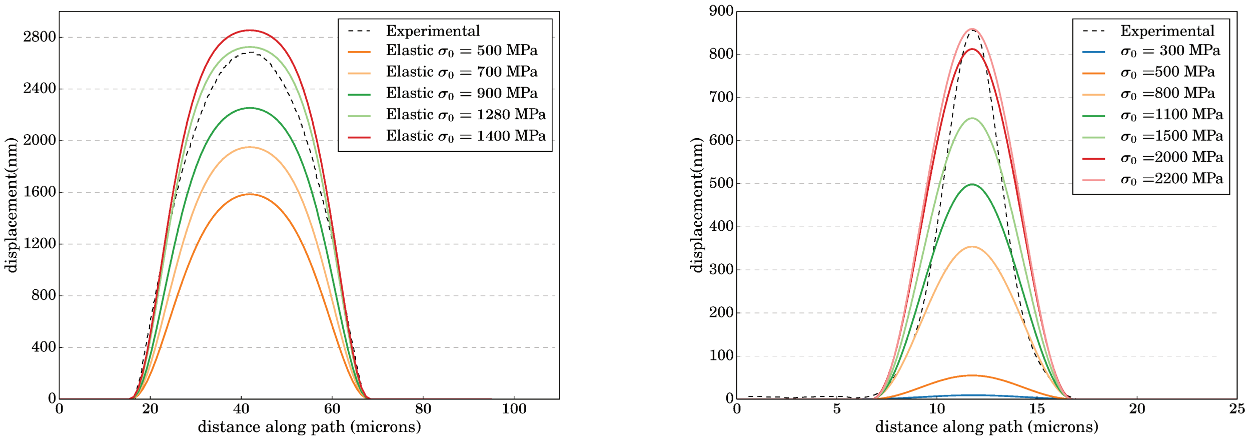

FIGURE 3.4: *Comparison between the experimental profiles of circular (left) and straight (right) buckles with results of FEM simulations assuming a linear elastic behavior of the film, obtained for several values of* σ_0.

$1600\,\mathrm{nm}$. In order to reach the maximum deflection observed experimentally using an elastic FEM model, we need to apply an initial stress of $1280\,\mathrm{MPa}$, which is more than twice the value of experimentally measured internal stresses.

In the case of α, the residual stress of the experimental case was estimated to be around $300\,\mathrm{MPa}$ and the buckle had a maximum deflection of approximately $850\,\mathrm{nm}$. The prediction obtained using the same stress does not show any buckle. This is due to the fact that the critical stress calculated using equation 1.8 ($\sigma_c \simeq 515$ MPa) is larger than σ_0. Thus using an elastic buckling model, we need a stress of at least $515\,\mathrm{MPa}$ to have a buckling structure. In order to get a blister's profile as high as the experimental one, a stress of $2200\,\mathrm{MPa}$ is necessary as shown in figure 3.4. Furthermore, the $2200\,\mathrm{MPa}$ elastic profile and the experimental one are different: The profile obtained using elastic FEM model shows a classical cosine-like profile (equation 1.7), whereas the experimental case shows a "slimmer" curve with a smaller slope at the base. This particularity of the shape can be interpreted as the sign of a plastic response in the film and/or the interface.

In conclusion, experimental profiles obtained from sample α and sample γ exhibited higher deflections and a notable difference in morphology compared to those predicted in the frame of a purely elastic model and under identical geometrical and loading conditions. Thus, a purely elastic model captures neither the height of the experimental blisters nor their profiles. As gold thin films are shown to have ductile behaviour, we propose in the next section to account for film's plastic response and study the effect of the different hardening parameters on the buckling profile.

3.3 Elastic-plastic model

In this section, we will present and discuss our most significant results accounting for elastic-plastic buckling of thin films. We will first study the effects of plasticity on the buckling of thin films. We will study the effect of the ratio $\frac{\sigma_0}{\sigma_y}$ as well as the hardening type on the buckling morphology and the distribution of plastic deformation in the film. Then, we will study of the influence of the loading history on the final buckle.

3.3.1 Influence of elastic-plastic behaviour on the buckling of thin films

We will first compare the buckling profiles of purely elastic and elastic-plastic films to investigate the effect of plasticity on the morphology of the blister and in particular its maximum deflection and folding angle. Then, we will examine the influence of plasticity on the onset of buckling (i.e the critical buckling stress). Eventually, we will investigate the influence of hardening through a parametric study. For the sake of clarity and in order to minimize simulations running times, we chose to perform this study using only a straight blister geometry.

Effect of the elastic-plastic behaviour on the maximum deflection

In this section, emphasis is laid on the examination of the effect of plasticity and in particular the effect of the ratio $\frac{\sigma_0}{\sigma_y}$ on the buckling morphology. The effect of hardening on elastic-plastic response will be studied later in section 3.3.1.

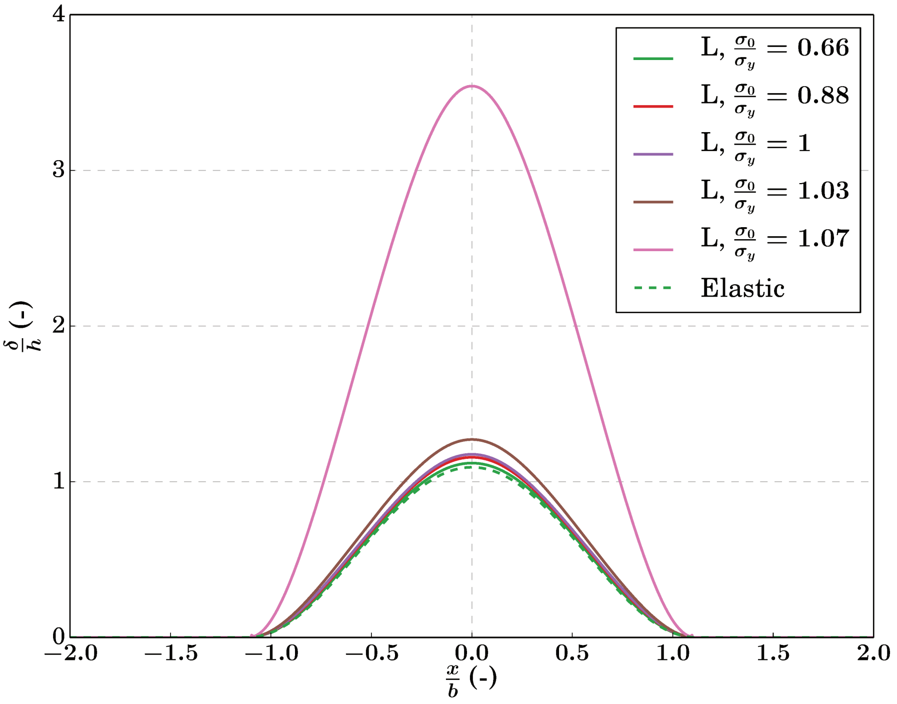

FIGURE 3.5: *Comparison between elastic and elastic-plastic straight blisters' profiles. The y-axes represents normalized deflection* $\frac{\delta}{h}$*, where* δ *is the out-of-plane displacement of the film and* h *the thickness of the film (fixed). All cases are subject to the same residual stresses (*$\sigma_0 = 800$ MPa*). The elastic-plastic behaviour is described by Ludwik hardening with the following fixed parameters* $K = 130$ MPa*,* $n = 0.25$*. We vary* σ_y

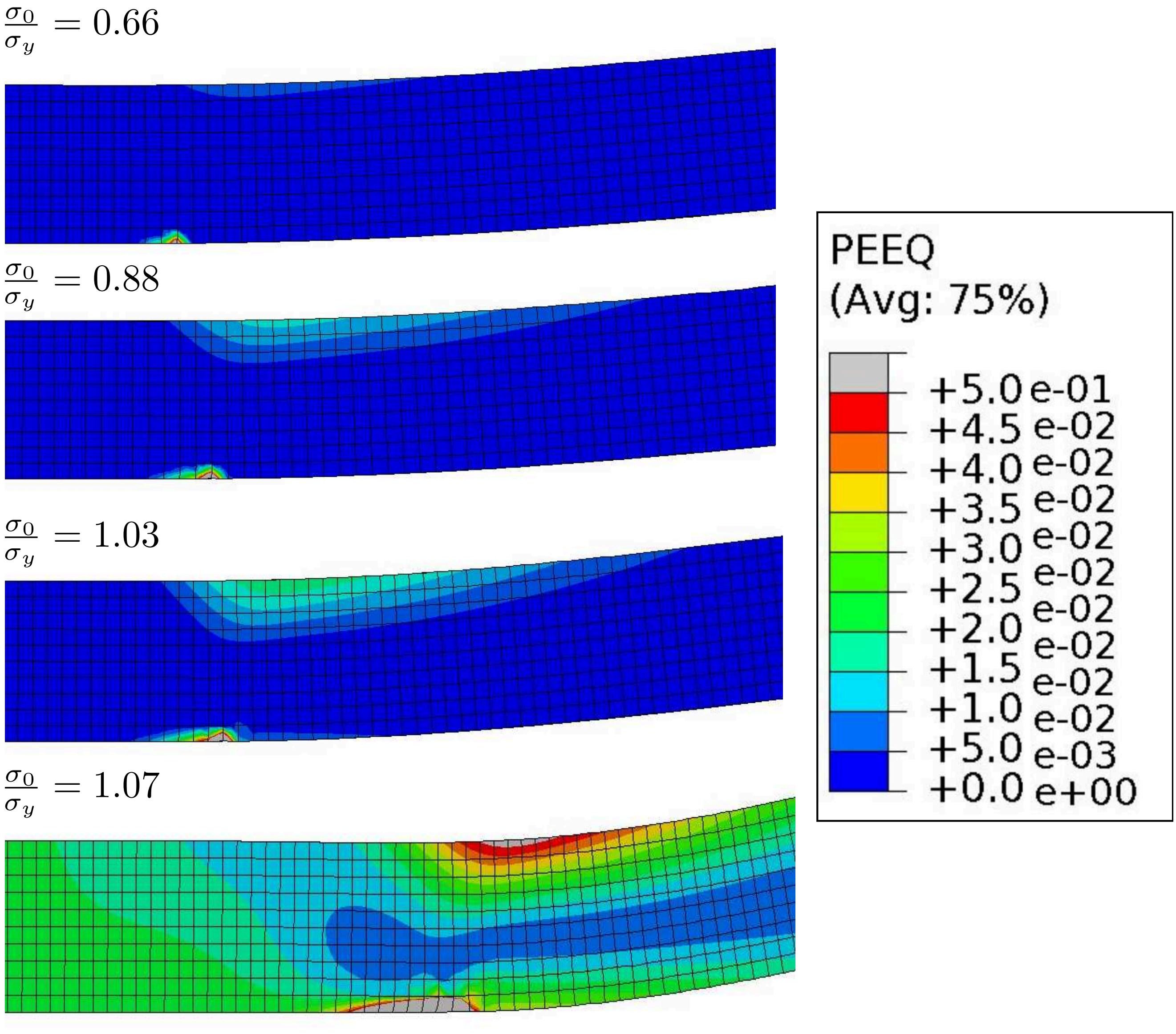

FIGURE 3.6: *Equivalent plastic strain mapping for the cases* $\frac{\sigma_0}{\sigma_y} = 0.66$*,* $\frac{\sigma_0}{\sigma_y} = 0.88$ *and* $\frac{\sigma_0}{\sigma_y} = 1.03$*. All cases are subject to the same residual stresses (*$\sigma_0 = 800$ MPa*). The elastic-plastic behaviour is described by Ludwik hardening with the following fixed parameters* $K = 130$ MPa*,* $n = 0.25$*. We vary* σ_y

To do so, we considered the same geometrical configuration (film thickness $h = 400\ \mathrm{nm}$ and $2b = 11\ \mu\mathrm{m}$) and the same final stress in the unbuckled area ($\sigma_0 = 800\ \mathrm{MPa}$) in all our simulations. We chose to use Ludwik hardening law (its expression is given by equation 3.1) with low hardening rate. We fixed the hardening modulus $K = 130$ MPa and the strain hardening exponent $n = 0.25$. Then, we tested various values of the yield stress so that we have different values of $\frac{\sigma_0}{\sigma_y}$ varying form 0.66 to 1.07.

The predicted profiles are presented in figure 3.5. In figure 3.6, we present for each case the mapping of plastic strain distribution at the base of the blister. We notice that for an identical final stress ($\sigma_0 = 800\ \mathrm{MPa}$), thin films with elastic-plastic behaviour exhibit buckling structures with larger maximum deflections compared to the purely elastic case. The difference in maximum deflection is observed for values of $\frac{\sigma_0}{\sigma_y}$ as low as 0.66 and is more spectacular for $\frac{\sigma_0}{\sigma_y} \geq 1$. This tendency is thus closely linked to the plastic strain generated inside the film. Indeed, for $\frac{\sigma_0}{\sigma_y} = 0.66$, the equivalent plastic strain does not exceed 5% and is confined in a small area near the base of the buckle while the rest of the film remains free of plastic strain (see figure 3.6). This observation is not true for $\frac{\sigma_0}{\sigma_y} \geq 1$. In particular, in the case $\frac{\sigma_0}{\sigma_y} = 1.07$, the equivalent strain mapping shows a global plastic deformation with values that do not exceed 3% in the unbuckled area but reach 41% locally at the folded area (figure 3.6(d)).

When $\frac{\sigma_0}{\sigma_y} \leq 1$, the unbuckled area of the film naturally shows no plastic deformation since $\sigma_{eq} < \sigma_y$. However, there is plastic deformation mainly localized at the folded area of the buckle. For instance, the case with $\frac{\sigma_0}{\sigma_y} = 0.66$ shows very little plastic deformation exclusively near the folded area (figure 3.6(a)). Its maximum value reaches roughly 5% and the effect on the maximum deflection of the buckle is small, with a deflection very close to the one obtained in the purely elastic case.

To summarize, depending on the ratio $\frac{\sigma_0}{\sigma_y}$, plastic deformation can either be exclusively localized near the folded area ($\frac{\sigma_0}{\sigma_y} \leq 1$) or global ($\frac{\sigma_0}{\sigma_y} \geq 1$) with maximum plastic strain near the folded area. However, the results obtained for $\frac{\sigma_0}{\sigma_y} \geq 1$ should be considered cautiously as Ludwik hardening law is not meant to describe high plastic deformation in metals. Extreme cases such as $\frac{\sigma_0}{\sigma_y} = 1.07$ may then not reflect to full extend what occur in metallic thin films undergoing large plastic strain.

Effect of the elastic-plastic behaviour on folding angle on the blister base

As noted previously, the profiles predicted in the case of purely elastic and elastic-plastic buckling models can be different in particular with regards to their shape and maximum deflection. Recent studies [18] suggest that the buckling structures observed in ductile thin films can exhibit higher folding angles compared to elastic thin films. Such structure have especially been observed for circular blisters.

In order to evaluate if there plasticity cause a noticeable rotation at the base of the straight blister, we compare the profile obtained with a purely elastic film and the one obtained with an elastic-plastic film with high deformation ($\frac{\sigma_0}{\sigma_y} = 1.07$). Even if the angle at the edge ($\theta = (\frac{d\omega}{dx})_{(x=-b)}$) seems higher for the plastic film, it is interesting to compare the normalized profiles ($\frac{\omega}{\delta_{max}} = f(\dfrac{x}{b})$) in both cases. This is done in figure 3.7, and it is clear that the normalized profiles are nearly identical which results in identical normalized angles ($\overline{\theta} = \dfrac{b}{\delta_{max}}(\dfrac{d\omega}{dx})_{(x=-b)}$). We can conclude that, in the case of elastic-plastic buckling of straight blister, with a monotonic loading and without delamination, the generic sinusoidal shape of the blister is not modified, even if large plastic deformation occurs.

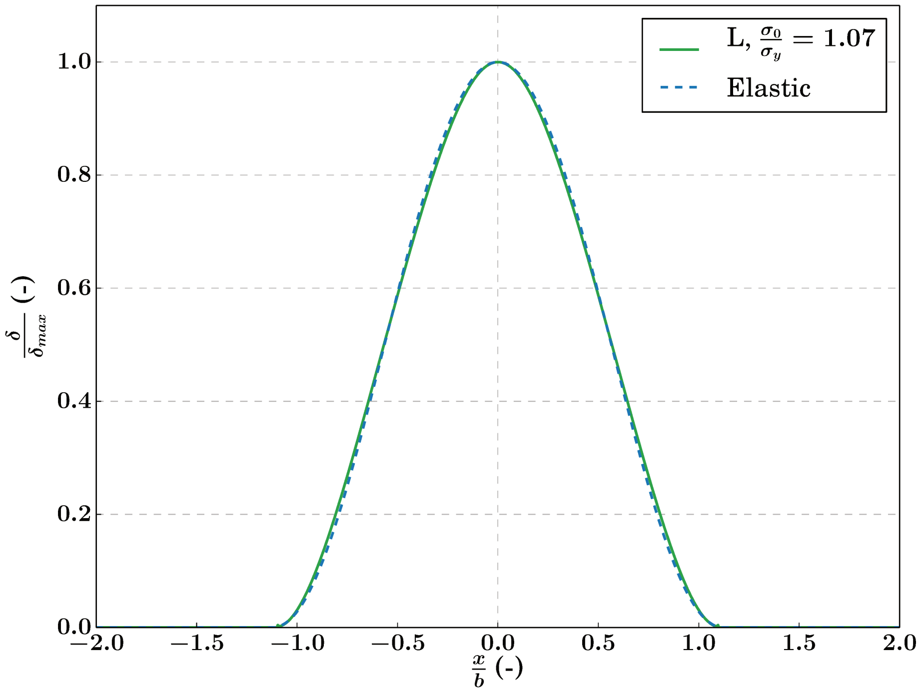

FIGURE 3.7: *Comparison between the profiles of elastic and elastic-plastic ($\frac{\sigma_0}{\sigma_y} = 1.07$) straight blisters obtained for the same final stress $\sigma_0 = 800$ MPa. The y-axes represents $\frac{\delta}{\delta_{max}}$ where δ_{max} is the maximum deflection for elastic and elastic-plastic cases respectively. This representation allows the comparison between the morphologies of two cases even if they have different maximum deflection. (The elastic-plastic behaviour is described by Ludwik hardening $\sigma_y = 775$ MPa, $K = 130$ MPa, $n = 0.25$)*

Could plasticity influence the onset of buckling?

We have discussed in the previous section the influence of plasticity on the final buckling profile of straight blisters. However, we did not consider its influence on the onset of buckling. In section 2.3.2, we demonstrated that the residual stresses in the post-buckled structure observed for sample α are lower than the critical stress calculated in the frame of purely elastic buckling. An interesting question here is whether the elastic-plastic behaviour of thin films can affect the critical buckling stress for a given geometrical configuration. To address this question, we performed several FEM analyses with different $\frac{\sigma_0}{\sigma_y}$ ratios and plotted the function $\frac{\delta}{h} = f(\frac{\sigma_0}{\sigma_c})$, where σ_0 is the stress in the film, σ_c the critical buckling stress, δ is the maximum out-of-plane displacement and h the film's thickness . The elastic-plastic law used is a Ludwik hardening law with $\sigma_y = 800$ MPa, $K = 130$ MPa and $n = 0.25$. The function f can be derived in the case of a purely elastic thin film using Föppl von Kármán plate theory. Its analytical expression is given by equation 1.10 and is represented in figure 3.8 using dashed lines. In graph 3.8, we also plotted in grey line the f-curve obtained using a purely elastic FEM model. These results are in good agreement with FVK theory.

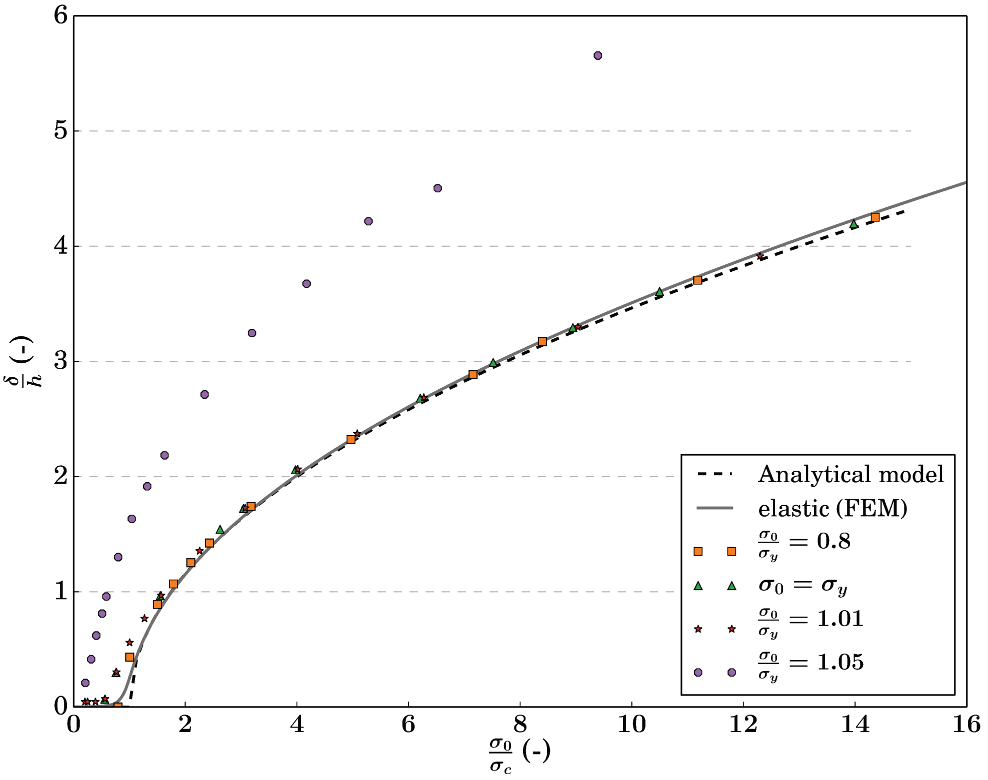

FIGURE 3.8: *Normalized deflection for straight blisters as a function of the loading ratio for the following for elastic analytical solution, elastic numerical solution and elastic-plastic numerical solutions:*$\frac{\sigma_0}{\sigma_y} = 0.8$, $\sigma_0 = \sigma_y$, $\frac{\sigma_0}{\sigma_y} = 1.01$ *and* $\frac{\sigma_0}{\sigma_y} = 1.05$. *The simulations were made using the same elastic-plastic law (*$\sigma_y = 800$ MPa, $K = 130$ MPa, $n = 0.25$*).*

For elastic-plastic modelling, we considered four different cases: $\frac{\sigma_0}{\sigma_y} = 0.8$, $\frac{\sigma_0}{\sigma_y} = 1$, $\frac{\sigma_0}{\sigma_y} = 1.01$ and $\frac{\sigma_0}{\sigma_y} = 1.05$. The first case corresponds to the lowest local plastic deformation values (at the folded area of the films) while the last one has the highest local plastic strain values with a global plastic deformation of the film.

For the case $\frac{\sigma_0}{\sigma_y} = 0.8$, the film shows a small local plastic strain of roughly 2% at the folded area of the film with no plastic deformation over the unbuckled area. The corresponding data points seem superimposed with the analytical curve. We can thus conclude that such levels of plastic strain are not sufficient to cause a noticeable change in maximum deflection values compared to purely elastic case.

Similarly, for the case $\frac{\sigma_0}{\sigma_y} = 1.01$, even-though the film undergoes a general plastic deformation, the plastic strain levels in both the unbuckled area ($\epsilon_p < 0.5\%$) and the folded area ($\epsilon_p = 5\%$) seem to be not sufficient to cause higher maximum deflection compared to the elastic case. For $\frac{\sigma_0}{\sigma_y} \leq 1.01$, the data points remain very close to those of a purely elastic film and the critical buckling stress can still be predicted using Föppl von Kármán plate theory.

On the contrary, for the case $\frac{\sigma_0}{\sigma_y} = 1.05$, the data points do not fit the analytical case and buckling seem to occur at stresses as low as $0.2\sigma_c$. Figure 3.9 provides a mapping of the equivalent plastic strain for the datum point $\frac{\sigma_0}{\sigma_y} = 1.05$ and $\frac{\sigma_0}{\sigma_c} = 0.5$. We notice that the equivalent plastic strain in the unbuckled area of the film is around 2% while it reaches the value of 16% in the folded area. This gives clear evidence that high plastic deformation can trigger earlier buckling of the thin film.

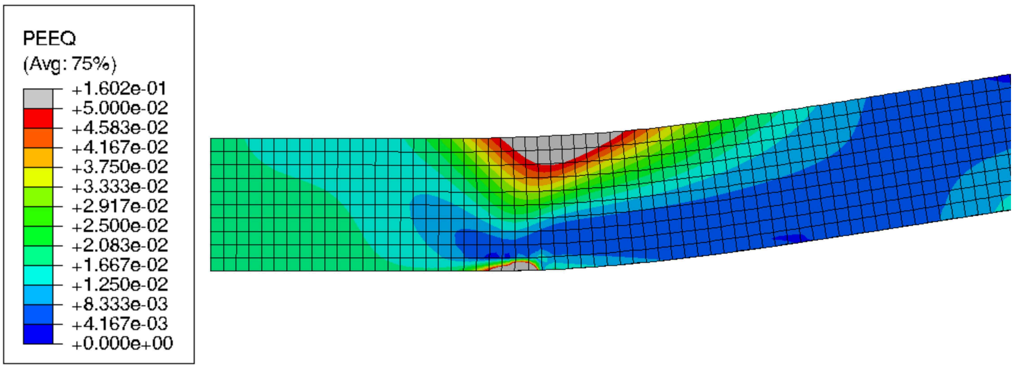

FIGURE 3.9: *Equivalent plastic mapping of the case* ($\frac{\sigma_0}{\sigma_c} = 0.5$, $\frac{\sigma_0}{\sigma_y} = 1.05$)

In figure 3.10, we plotted the buckling profiles corresponding to the case of purely elastic buckling and elastic-plastic buckling with $\frac{\sigma_0}{\sigma_y} = 1.05$ for the loading ratios $\frac{\sigma_0}{\sigma_c} = 0.5$ and $\frac{\sigma_0}{\sigma_c} = 9.4$. In the case $\frac{\sigma_0}{\sigma_c} = 0.5$, the elastic thin film is clearly unbuckled while the elastic-plastic film is buckled with a maximum deflection approximating the thickness of the film. In the case $\frac{\sigma_0}{\sigma_c} = 9.4$, both elastic and elastic-plastic models show buckled structures with sensibly higher maximum deflection in the later case.

To gain better insight into the influence of plasticity on the onset of buckling and the profile of the blister, we carried out various simulations with different ratios $\frac{\sigma_y}{\sigma_c}$ collecting over 5000 different data points $(\frac{\sigma_0}{\sigma_c}, \frac{\sigma_y}{\sigma_c}, \frac{\delta}{h})$. By plotting these points into a $3D$ graph and using a Delaunay triangulation, we generated the surface corresponding to the function $\frac{\delta}{h} = f(\frac{\sigma_0}{\sigma_c}, \frac{\sigma_y}{\sigma_c})$ as shown in figure 3.11.

We can notice that the curve can be decomposed visually into two parts: a part for which $\sigma_y > \sigma_0$ and a part where $\sigma_y \leq \sigma_0$. The two parts are separated by the plane $\frac{\sigma_0}{\sigma_c} = \frac{\sigma_y}{\sigma_c}$ (i.e. $\sigma_0 = \sigma_y$) plotted in figure 3.11. In the part $\sigma_y > \sigma_0$, plasticity has little influence on the final deflection of the blister and the curve has the typical square root form of the analytical solution of pure elastic buckling given by equation 1.10. However, in the part corresponding to $\sigma_y \leq \sigma_0$, the material undergoes high plastic deformations and normalized deflection increases sharply as function of $\frac{\sigma_0}{\sigma_c}$.

Thus, as we tend towards high values of $\frac{\sigma_y}{\sigma_c}$, the fraction of the curve described by a square root function becomes more important and we tend towards a purely elastic behaviour. Conversely, as the ratio $\frac{\sigma_y}{\sigma_c}$ decreases, we tend towards a purely plastic behaviour and buckling can occur for $\sigma_0 < \sigma_c$.

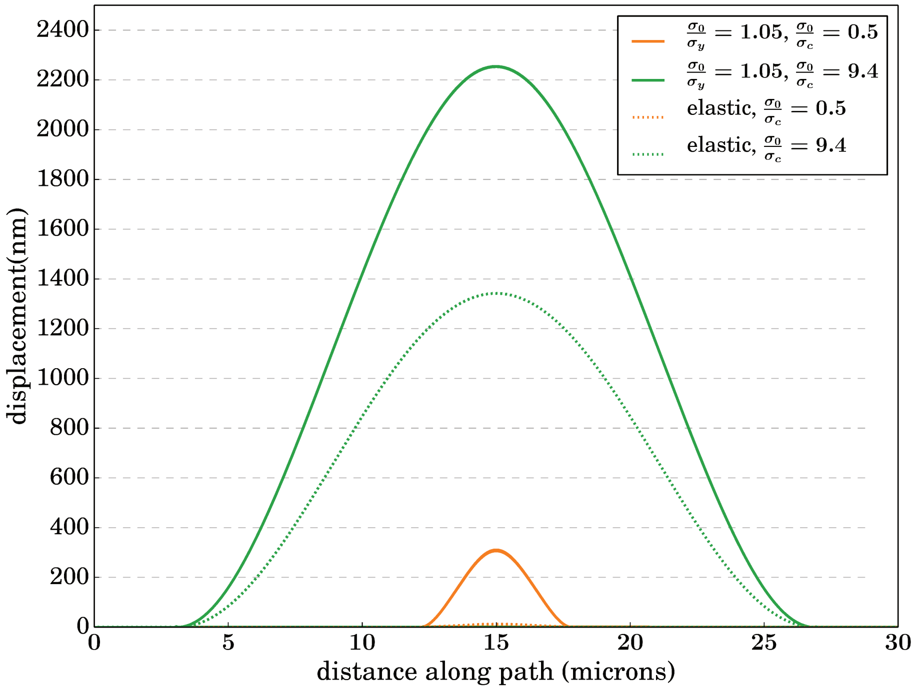

FIGURE 3.10: *Comparison between elastic and elastic plastic (Ludwik* $\sigma_y = 800$ MPa, $K = 130$ MPa, $n = 0.25$*) profiles for* $\frac{\sigma_0}{\sigma_c} = 0.5$ *and* $\frac{\sigma_0}{\sigma_c} = 9.4$.

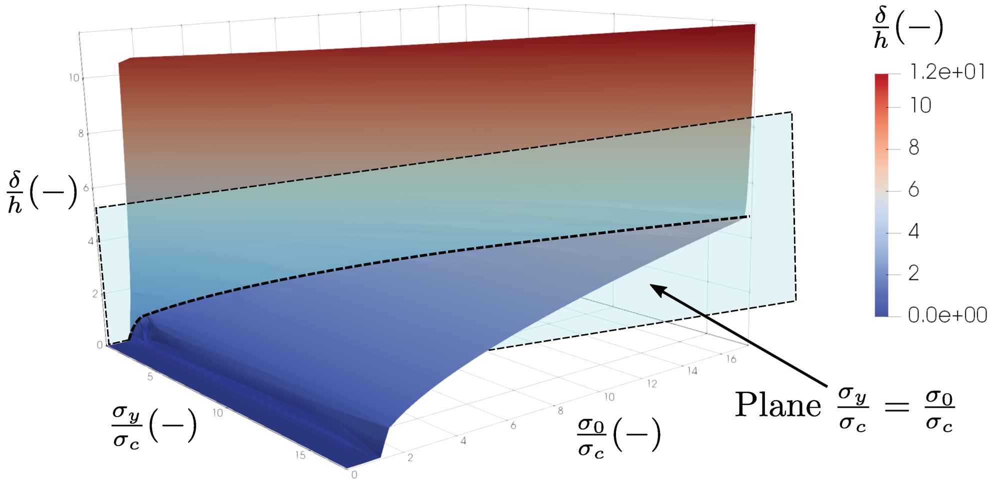

FIGURE 3.11: *3D representation of the normalized deflection* $\frac{\delta}{h}$ *as function of* $\frac{\sigma_y}{\sigma_c}$ *and* $\frac{\sigma_0}{\sigma_c}$. *This curve is plotted using the following Ludwik hardening:* $K = 130$ MPa *and* $n = 0.25$.

Another important observation is that for a given sinusoidal profile of a straight blister, the maximum deflection can be reached by mean of purely elastic buckling of by elastic-plastic buckling with different possible couples $(\frac{\sigma_0}{\sigma_c}, \frac{\sigma_y}{\sigma_c})$. In particular, for a given value of maximum deflection δ_0, the plane $z = \frac{\delta_0}{h}$ intercepts the surface $\frac{\delta}{h} = f(\frac{\sigma_0}{\sigma_c}, \frac{\sigma_y}{\sigma_c})$ along a line and we have an infinite number of solutions.

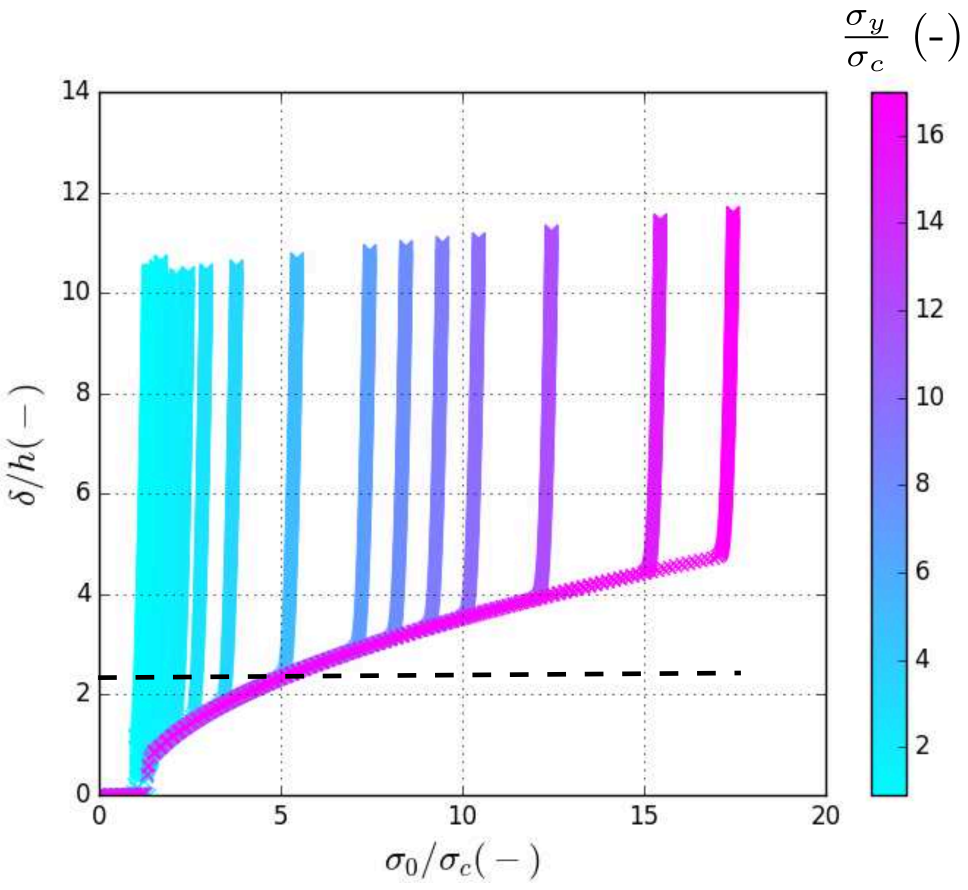

FIGURE 3.12: *2D projection of normalized deflection $\frac{\delta}{h}$ as function of $\frac{\sigma_0}{\sigma_c}$. The graph features different level lines of $\frac{\sigma_y}{\sigma_c}$. These curve are plotted for a Ludwik hardening: $K = 130$ MPa and $n = 0.25$.*

This observation can be made more easily if we consider the projection of the $3D$ curve on the plane $x - z$ as shown in figure 3.12. The figure features the function $\frac{\delta}{h} = f(\frac{\sigma_0}{\sigma_c})$ plotted for different iso-value lines $\frac{\sigma_y}{\sigma_c}$. For instance, if a straight blister with a sinusoidal shape is observed experimentally, by plotting the horizontal line corresponding to its normalized maximum deflection, we obtain a variety of possible elastic-plastic solutions that could possibly lead to its formation. An example is given in figure 3.12), where the elastic-plastic buckling solutions obtained correspond to a Ludwik hardening with a coefficient $K = 130$ MPa and a strain hardening exponent n of 0.25. For the amplitude of a straight sided blister corresponding to the horizontal dashed line, the residual stress value σ_0 that be identified varies of a ratio from 1 to 5.

A Ludwik law with a larger hardening coefficient, for example $k = 500$ MPa, leads to a more curved surface for the part corresponding to $\sigma_y \leq \sigma_0$ in the $3D$ plot as presented in figure 3.13.

These observations lead us to the conclusion that the simple observation of a blister with a sinusoidal shape is not sufficient to state that the films has undergone a purely elastic deformation. In this case, the residual compressive stresses in the film should be measured and the value of the analytically predicted deflection of the blister ($\delta_{analytical}$) should be

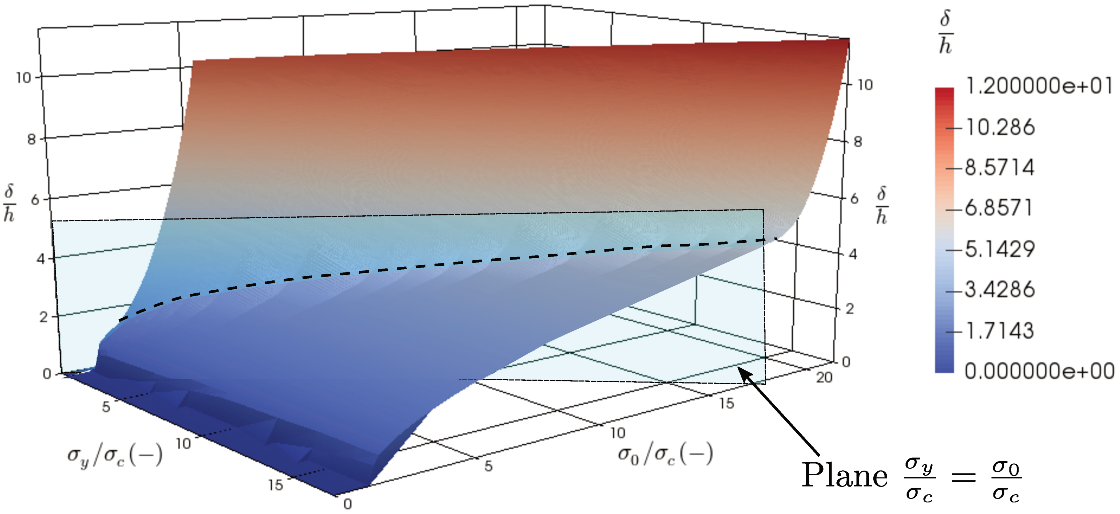

FIGURE 3.13: *$3D$ representation of the normalized deflection $\frac{\delta}{h}$ as function of $\frac{\sigma_y}{\sigma_c}$ and $\frac{\sigma_0}{\sigma_c}$. This curve is plotted using the following Ludwik hardening: $K = 500$ MPa and $n = 0.25$.*

compared with the deflection measured experimentally ($\delta_{experimental}$). We can conclude that the buckling of the thin film occurred elastically, only if the two values $\delta_{experimental}$ and $\delta_{analytical}$ are comparable. If the deflection levels are different, it should give us a clue about the presence of plastic deformation of the film.

As it will be explained later in section 3.3.2, measuring the yield stress and the residual compressive stresses and comparing them may not even be sufficient to conclude whether the process of buckling occurred elastically or not. In certain cases (including in sample α), the film can undergo plastic deformation and exhibit final residual stresses that are lower than the yield stress.

Influence of hardening law on the morphology of elastic-plastic buckles

In order to study the influence of the hardening law on elastic-plastic buckling, we chose to implement either Ludwik hardening or linear hardening with different values of parameters. Ludwik's hardening has been described in part 2.1 and its expression is given by equation 3.1. It should be noted that linear hardening is a particular case of Ludwik hardening and is obtained for $n = 1$

$$\forall \sigma \geq \sigma_y, \sigma_{eq} = \sigma_y + K\epsilon_{eq}^p \tag{3.9}$$

where σ_{eq} is the stress in the material, σ_y its yield stress, K the hardening modulus and ϵ_{eq}^p the plastic strain. For both hardening laws, we set $\sigma_y = 800$ MPa according to our experimental measurements. We chose $n = 0.25$ for Ludwik's law which is a typical value for metals [2]. We finally tested different values of the hardening modulus K to understand the effect of hardening rate on the buckling response. The different parameters are summarized in table 3.2 and the corresponding laws are represented in figure 3.14.

Plasticity with Ludwik hardening						Linear hardening	
L1			L2			LH	
σ_y (MPa)	K (MPa)	n (-)	σ_y (MPa)	K (MPa)	n (-)	σ_y (MPa)	K (MPa)
800	50	0.25	800	130	0.25	800	80

TABLE 3.2: *Summary of the parameters' values used in linear and Ludwik hardening.*

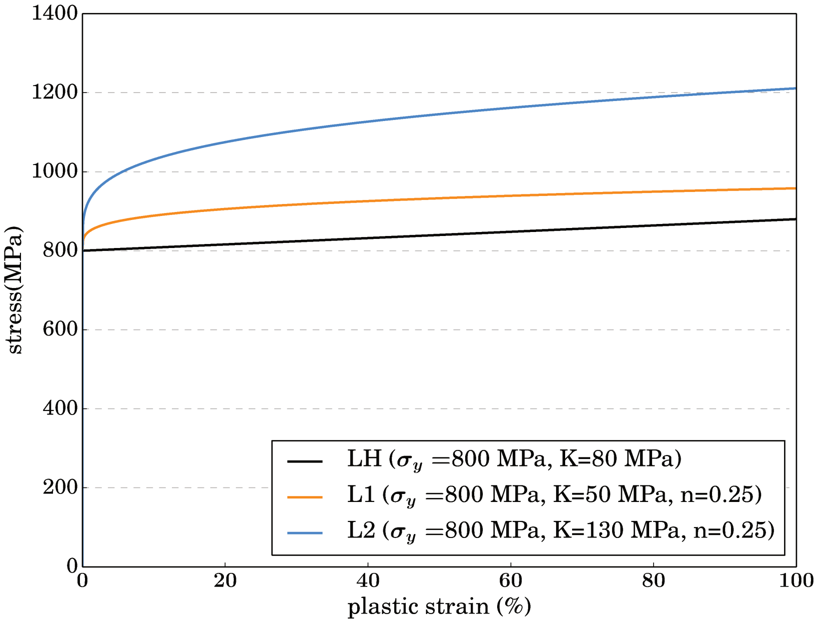

FIGURE 3.14: *Stress as a function of plastic strain for Linear plasticity and Ludwik laws*

The parameters are chosen so that we have different levels of hardening in each elastic-plastic response. The biggest hardening rate is associated with the Ludwik law L2, followed by L1 and finally by the linear hardening law (LH). It is expected then for case studies using LH law to exhibit the largest plastic deformation if the same value of final stress σ_0 is considered. It is recalled that for a film submitted to an equibiaxial compression stress of amplitude σ_0, the equivalent Mises stress is $\sigma_{eq} = \sigma_0$ (it is the stress state in the flat part of the film). We chose to compare the influence of hardening for two different stress states: A case corresponding to $\sigma_0 < \sigma_y$ in which plastic strain is supposed to occur only in high stress concentration area i.e the folded area and a case corresponding to $\sigma_0 > \sigma_y$ in which an extended plastic area is expected. The values chosen for these cases are $\frac{\sigma_0}{\sigma_y} = 0.875$ ($\sigma_0 = 700$ MPa) and $\frac{\sigma_0}{\sigma_y} = 1.0025$ ($\sigma_0 = 802$ MPa) respectively.

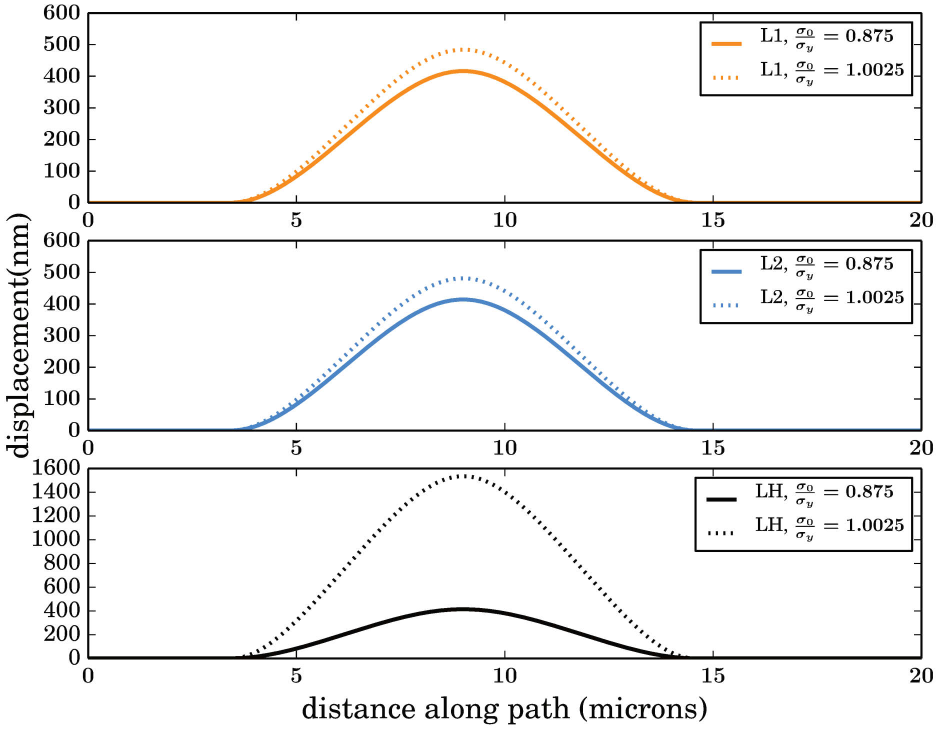

FIGURE 3.15: *Straight blisters' profiles for different elastic-plastic behaviours: L1 (Ludwik:*$\sigma_y = 800$ MPa, $K = 50$ MPa, $n = 0.25$*), L2: (Ludwik:*$\sigma_y = 800$ MPa, $K = 130$ MPa, $n = 0.25$*), LH (Linear hardening:*$\sigma_y = 800$ MPa, $K = 80$ MPa*)*

In figure 3.15, we plotted the different buckling response for each of the elastic-plastic behaviours detailed in table 3.2 and for $\frac{\sigma_0}{\sigma_y} = 0.875$ and $\frac{\sigma_0}{\sigma_y} = 1.0025$ in each case. We notice that the buckling responses for L1 and L2 are very similar for both loading ratios. However, in the case of linear hardening, the buckling shape has the same height as the previous cases for the loading $\frac{\sigma_0}{\sigma_y} = 0.875$, but is much higher in the case $\frac{\sigma_0}{\sigma_y} = 1.0025$. This is due to the difference in plastic strain distribution represented in figure 3.16. The figure shows the equivalent plastic strain mapping for each hardening law L1, L2 and LH in the case $\frac{\sigma_0}{\sigma_y} = 1.0025$. We notice that the strain distribution is very similar in cases L1 and L2 and exhibits small plastic strain in the unbuckled area of the film (0.03%). However, in the case of linear hardening, the film exhibits an equivalent plastic strain of 5% in the unbuckled area of the film and pretty large values at the folded area (over 100% deformation). In addition, the area of material with an equivalent plastic strain larger than 5% is much more extended than in the case of Ludwik hardening. This causes higher bending of the film and a maximum deflection that is four times the one obtained with Ludwik hardening.

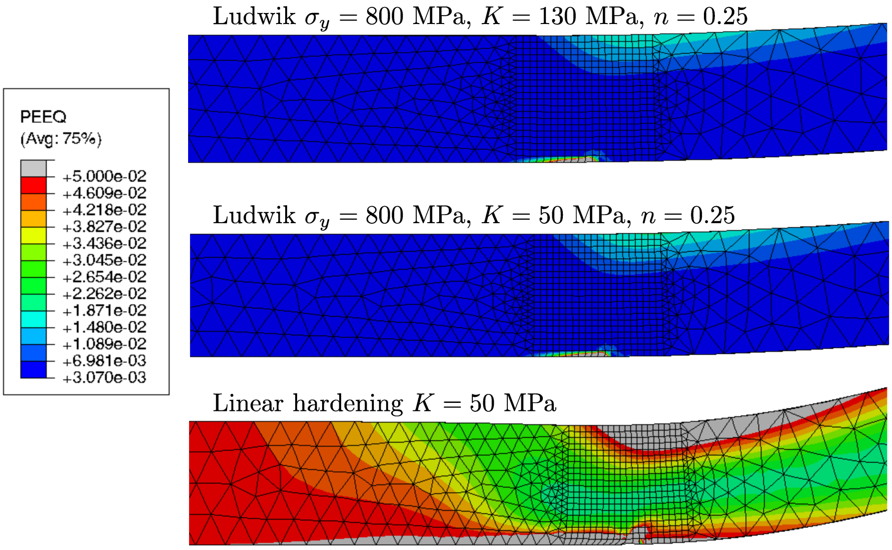

FIGURE 3.16: *Effect of the hardening law on plastic strain at the base of straight blisters* ($\sigma_0 = 802$ *MPa*)

It should be noted that in figure 3.15, the influence of hardening is studied for $\sigma_0 > \sigma_c$. Indeed σ_0 is equal to either 700 or 802 MPa which is larger than the value of critical stress corresponding to this configuration ($\sigma_c \simeq 550$ MPa). To have a complementary understanding of the effect of hardening for cases with $\sigma_0 < \sigma_c$, we carried out similar a similar study with an elastic limit $\sigma_y = 400$ MPa and the same hardening laws presented in table 3.2. For each of the hardening laws, we considered a case corresponding to $\sigma_0 < \sigma_y$ ($\frac{\sigma_0}{\sigma_y} = 0.875$) and a case corresponding to $\sigma_0 > \sigma_y$ ($\frac{\sigma_0}{\sigma_y} = 1.01$). In figure 3.18, we present the different buckling responses.

In all cases corresponding to $\sigma_0 < \sigma_y$, no buckling occurred and there seem to be no plastic deformation in the film. The materials characterized by a Ludwik type hardening exhibit small plastic deformation that does not exceed 0.5% even for $\sigma_0 > \sigma_y$ (see figure 3.17). These low levels of plastic deformation seem to be correlated with small buckling structures. However, in the case of linear hardening, the levels of plastic deformation are at least 10 times more important than in the cases of Ludwik hardening (around 8%) and result in higher buckling structure. Indeed in the case of linear hardening we evolved from the absence of buckling for $\sigma_0 < \sigma_y$ to a buckling structure with a maximum deflection that exceeds the thickness of the film!

Finally, the difference in profiles between the cases $\sigma_0 < \sigma_y$ and $\sigma_0 > \sigma_y$ is more spectacular for $\sigma_0 < \sigma_c$ (figure 3.18) compared to $\sigma_0 > \sigma_c$ (figure 3.15). Precise characterization of the hardening of ductile thin films is extremely important especially if the film exhibits residual stress values that are lower than the critical stress calculated in the frame of elastic buckling.

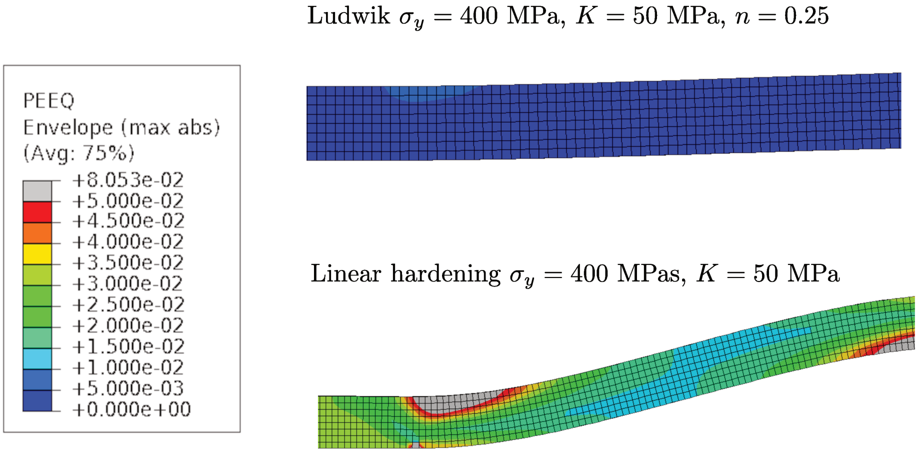
Ludwik $\sigma_y = 400$ MPa, $K = 50$ MPa, $n = 0.25$

Linear hardening $\sigma_y = 400$ MPas, $K = 50$ MPa

FIGURE 3.17: *Effect of the hardening law on plastic strain at the base of straight blisters ($\sigma_0 = 404$ MPa)*

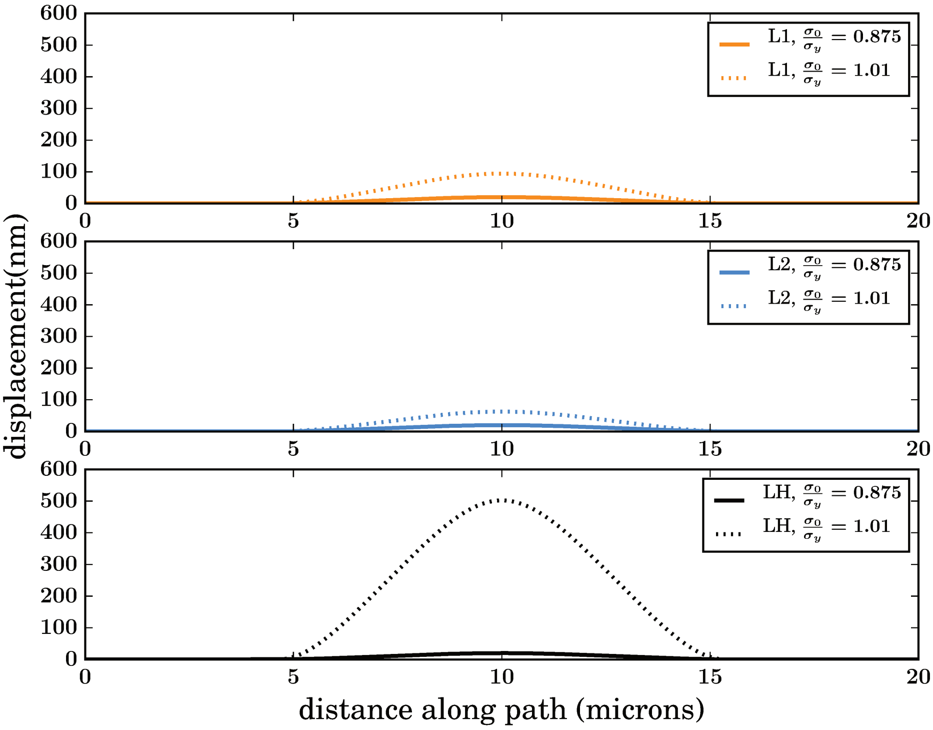

FIGURE 3.18: *Straight blisters' profiles for different elastic-plastic behaviours: L1 (Ludwik:$\sigma_y = 400$ MPa, $K = 50$ MPa, $n = 0.25$), L2: (Ludwik:$\sigma_y = 400$ MPa, $K = 130$ MPa, $n = 0.25$), LH (Linear hardening:$\sigma_y = 400$ MPa, $K = 80$ MPa)*

3.3.2 Considering the internal stresses evolution during the deposition process

Experimental evidence of non monotonic variations of internal stress during thin films' deposition

Thin films grown by plasma vapour deposition (PVD) often exhibit large intrinsic stresses that can lead to film failure. Measurements of stresses during the early stages of polycrystalline thin films deposition have been widely studied in literature [10, 29, 58, 61, 98]. It is largely acknowledged that the physical origins of growth induced stresses are related to the film micro-structural evolution during deposition. Two different types of growth can take place depending on adatoms/surface interaction: if the interaction between adatoms are stronger than between atoms of the substrate and adatoms, then we have a Volmer-Weber (VW) growth characterized by the formation of 3D islands. On the contrary, if the interaction between the substrate surface and adatoms is stronger than that between adatoms, we have Frank-Van der Merwe (FM) growth which is a layer-by-layer film growth [73].

In this part, we will consider the Volmer-Weber (VW) growth mechanism as it corresponds to our case study (gold thin film grown by magnetron sputtering at room temperature). In VW growth, discrete islands of different crystallographic orientations form at the beginning of the deposition process. Upon additional deposition, these isolated islands grow in diameter and new islands may nucleate which eventually leads to the formation of a continuous polycrystalline thin film. These different stages are depicted in figure 3.19

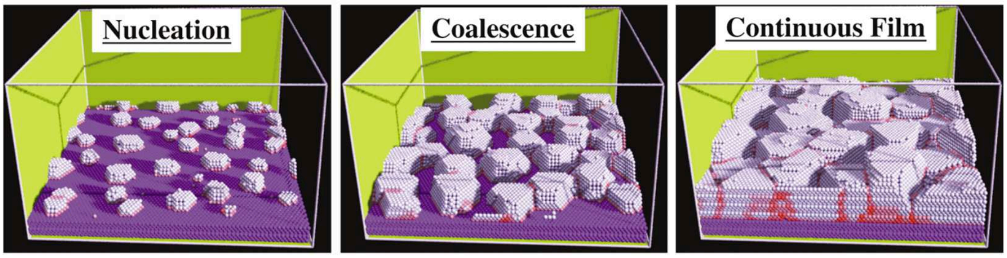

FIGURE 3.19: *The regimes of microstructural evolution during Volmer-Weber film growth. [35]*

Depending on the homologous temperature of the system (defined by $T_h = \frac{T_s}{T_m}$ where T_s is the substrate temperature during growth and T_m is the melting temperature of the films material) and the adatom mobility, two types of intrinsic behaviours have been identified in VW grown films [35, 61]. On the one hand, refractory materials with low adatom mobility such as Molybdenum (Mo) at room temperature exhibit tensile stresses that increase monotonicly during deposition and reach a plateau once the film becomes fully continuous. On the other hand, FCC materials with high adatom mobility such as gold (Au), silver (Ag) or copper (Cu) at room temperature have tensile stresses that peak in the early stages of film growth before decreasing and becoming compressive for thick continuous films. The measurements of intrinsic stresses are generally performed by substrate curvature measurements which can be linked to intrinsic stresses using Stoney equation [94]. Precise real-time stress measurements during the growth of thin films has been only made possible due to the development of in-situ curvature measurement such as multiple beam optical stress sensor

(MOSS) [1, 29, 34]. In-situ stress evolution curves during deposition process at room temperature of Au, Pd and Ag are presented in figure 3.20. In the case of gold thin film, we clearly notice the formation of tensile stresses for low film thickness that reach a peak at h_{cont} before decreasing and becoming compressive.

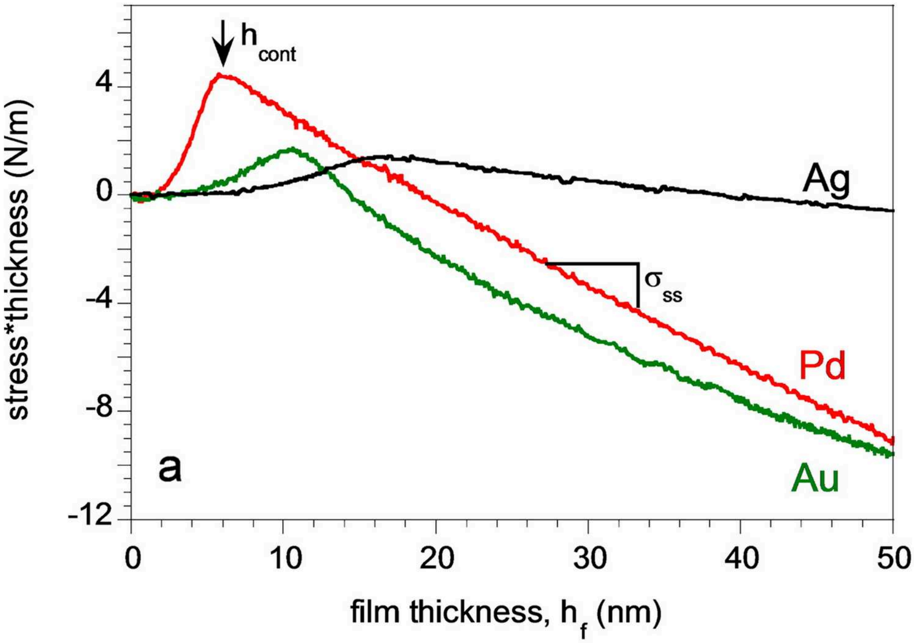

FIGURE 3.20: *Film force evolution during sputter deposition of Ag, Au and Pd films on a-SiOx. The film thickness corresponding to the tensile peak is referred as* h_{cont} *[1].*

It should also be noted that stress evolution in thin films can be highly dependent on the deposition parameters such as substrate potential or oxygen doping of the film as highlighted in [29]. Indeed, figure 3.21 shows clearly how the shape of real-time stress evolution curve as well as maximum compressive stresses values can vary depending on the sputtering parameters.

To conclude, stress variation during thin film deposition is not necessarily monotonic. It can reach a maximum value in the compressive regime before decreasing. This means that the stress value measured by XRD technique and presented in section 2.3.2 only depicts the final stress state of the film and is thus not indicative of the history of stress evolution.

Limits of monotonic loading: Experiments versus modelling results

We first perform calculations accounting for a monotonic increase of the intrinsic stress distribution. The stress loading starts from zero and reaches the final stress values predicted from curvature measurements. For both straight and circular blisters, final stress values, materials properties and thickness inputs are presented in table 3.3.

For each configuration (circular and straight blister), we consider different yield stress values varying from $\sigma_y = 400$ MPa to $\sigma_y = 800$ MPa. As a reminder, the value $\sigma_y = 400$ MPa corresponds to the yield stress measured using nanoindentation technique in sample α where the straight blister has been observed. For the experimental case of the circular blister

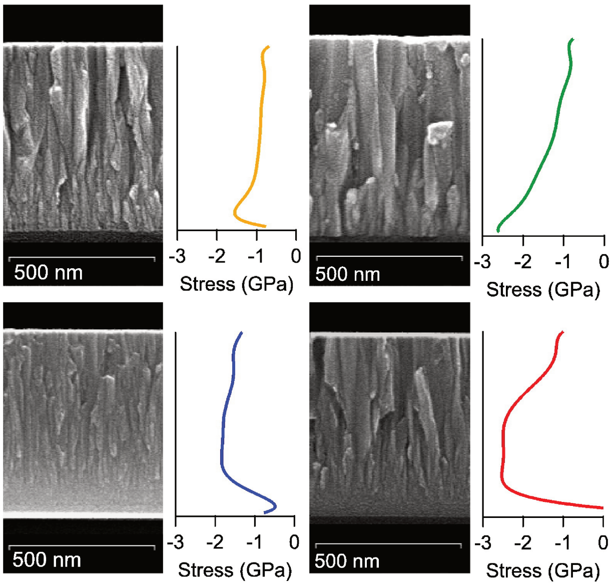

FIGURE 3.21: *FEG-SEM images showing the influence of substrate potential and oxygen doping on the microstructure of molybdenum thin films. Top left: Mo at floating potential, top right: Mo at -75 V, bottom left: Mo with 2 sccm of O_2 at floating potential and bottom right:Mo with 2 sccm of O_2 at -75 V.* [29]

-	E (GPa)	ν (-)	h (nm)	$2b$ (µm)	σ_0 (MPa)
circular blister (sample γ)	85	0.44	630	53	500
straight blister (sample(α)	85	0.44	400	11	300

TABLE 3.3: *Summary of the gold thin film elastic properties (E: Young's modulus, ν: Poisson's ratio), blisters geometries (h: thin film's thickness, $2b$: blister's diameter) and thin film residual stresses (σ_0) for both samples α and γ*

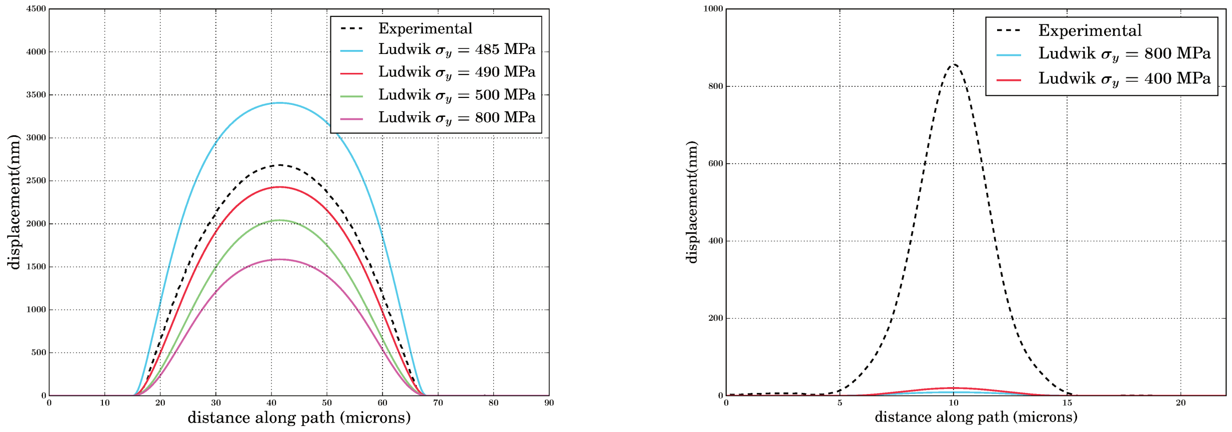

FIGURE 3.22: *Comparison between the experimental blister's profile and elastic-plastic numerical model results for both circular (left) and straight (right) blisters using the same conditions but with different yield stresses (Ludwik strain hardening* $K = 50$ MPa, $n = 0.25$

in sample γ, the paper from which the profile of the blister is derived [18] does not provide us with a characterization of the elastic behaviour of the film. However, studies of the elastic-plastic behaviour of gold thin films found in the literature [27, 44] show values of yield stress reaching up to 700 MPa which is consistent with the range of values of yield stress chosen in this study. We also chose to work with a low value of hardening coefficient $k = 50$ MPa as suggested by the nano-indentation tests. In figure 3.22, we report the experimental and predicted profiles with monotonic loading, by applying in the simulation the stress that have been experimentally measured in the final state. The curves on the left correspond to the circular case while those on the right describe the straight one. We notice that for the circular case, a linear loading with a final value of $\sigma_0 = 500$ MPa is not sufficient to reach the experimental height for $\sigma_y = 800$ MPa. However, a yield stress value around 490 MPa seems to be sufficient to produce a circular blister with a profile that is similar to the experimental one in the case of monotonic loading. In the case of the straight blister, an intrinsic stress of $\sigma_0 = 300$ MPa is not sufficient to induce the buckling of the film for both values of yield stress: 400 and 800 MPa. We can thus conclude that prescribing a linearly increasing loading with the final value of σ_0 could possibly capture the blister's experimental profile in the case of the circular blister. However, this is not the case for the straight blister and the prescribed stress could hardly trigger the buckling of the film.

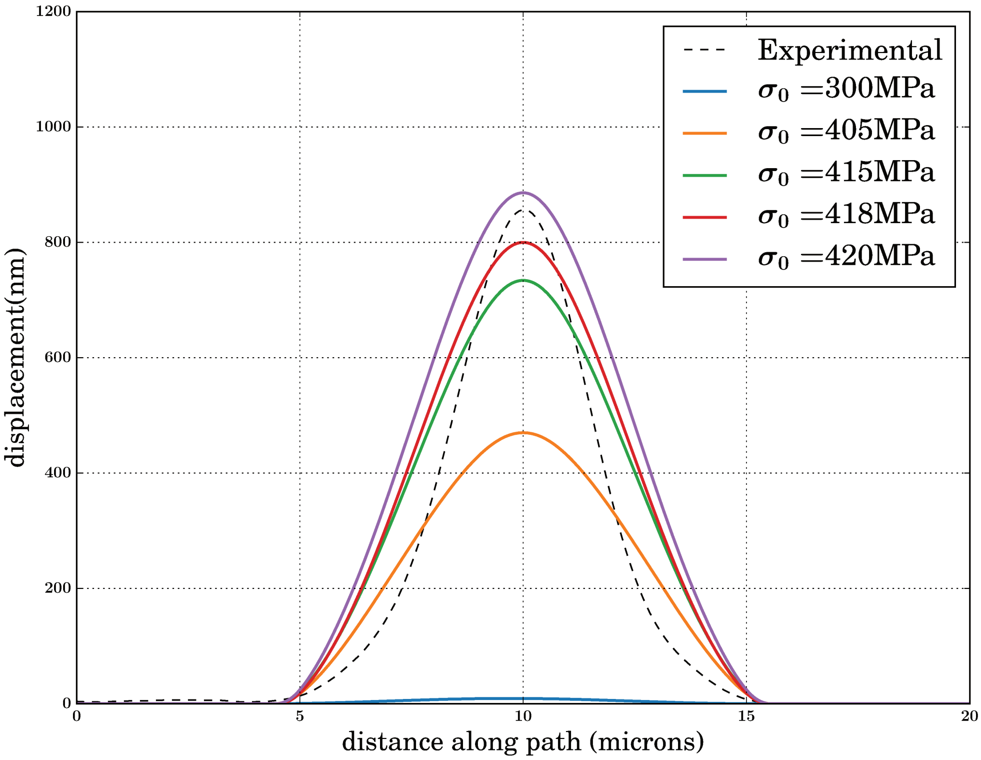

FIGURE 3.23: *Comparison between the experimental blister's profile and elastic-plastic numerical model results in the case of straight blister (Ludwik strain hardening* $\sigma_y = 400$ MPa, $K = 50$ MPa, $n = 0.25$*) for different* σ_0 *values*

In order to have an idea of the stress needed to reach the maximum deflection of the straight blister observed experimentally with FEM modelling using monotonically increasing loading, we performed a parametric study with an elastic-plastic film and values of σ_0 varying from 300 MPa to 4200 MPa.

Figure 3.23 shows that a stress slightly beyond the yield stress ($\sigma_y = 400$ MPa) is needed for the straight blister to reach the experimental height. It should be noted that these simulations were performed using ludwik hardening ($K = 50$ MPa, $n = 0.25$). If a lower hardening rate is used, similar results with lower stresses σ_0 would be expected to reach the same maximum deflection.

To summarize, the study of thin films buckling using an elastic-plastic model for the film and a monotonically increasing loading provide profiles of straight blister that are different from those observed experimentally, even if the applied stress σ_0 is the one measured experimentally in the final state of the system. To reach deflection values that are close to the experimental ones, *residual stresses at least as high as the yield stress are needed*. In the case of circular blister, the uncertainty concerning the value of yield stress make it difficult to state whether the measured final stress in the film is sufficient to capture the experimental profile or not. These results considered along with the experimental aspects of stress evolution during the deposition process as discussed in the previous paragraph, invite us to consider an elastic-plastic FEM model with non-monotonic loading in terms of intrinsic stresses during deposition.

monotonic versus non-monotonic loading

In order to test the influence of non-monotonic intrinsic stress loading on the final morphology of the blister, we propose a preliminary model which accounts for a non-monotonic stress variation during deposition. This model does not account for thickness change during deposition but a non-monotonic variation of σ_0 is considered during deposition which is a good starting point to test this hypothesis. In this section, we propose to test two different loading histories: the former loading represented in figure 3.24 by an orange line, and a non-monotonic one plotted in blue. During the non-monotonic loading, the stress in the film first reaches linearly a maximum stress value σ_{max} which is slightly above the yield stress before decreasing until the final stress corresponding to the experimental measurements. For the sake of discussion, we applied non-monotonic loading not only for the case of the straight blister but also for the case of the circular blister. For the straight blister case, we used an elastic-plastic response with the yield stress $\sigma_y = 400$ MPa while for the circular blister, we chose a yield stress of $\sigma_y = 800$ MPa. In both cases a Ludwik hardening with small hardening is applied $K = 50$ MPa and $n = 0.25$.

The corresponding predicted profiles are plotted in figure 3.25. Different values for σ_{max} have been tested. The main challenge is to choose the proper value of σ_{max} that maintains the structure of the buckle at the right height at the end of the unloading phase. We noticed that if σ_{max} is set to a lower value than σ_y, the buckling structure quickly collapses during unloading and regains a similar profile to the one obtained using monotonic loading to the value σ_0. As shown in section 3.3.1, a target stress lower than the yield stress generates plastic deformation that is only localized in the folded area of the blister. We can

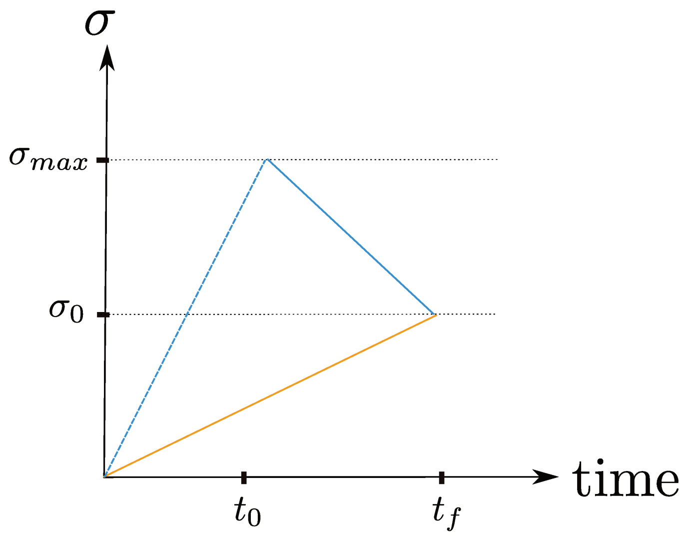

FIGURE 3.24: *Different loading histories: Linear loading (orange) and bi-linear loading (blue).*

then conclude that such localized plastic deformation is not sufficient to maintain a buckling structure during stress relaxation. Also, if σ_{max} is too large, then, the blister would maintain a maximum deflection that is higher than the experimental one even after stress relaxation. After analysing the results for different σ_{max} values for the elastic-plastic laws detailed above, values of σ_{max} equal to 810 MPa in the case of circular blister and to 421 MPa in the case of straight blister were able to capture the experimental height of the blister.

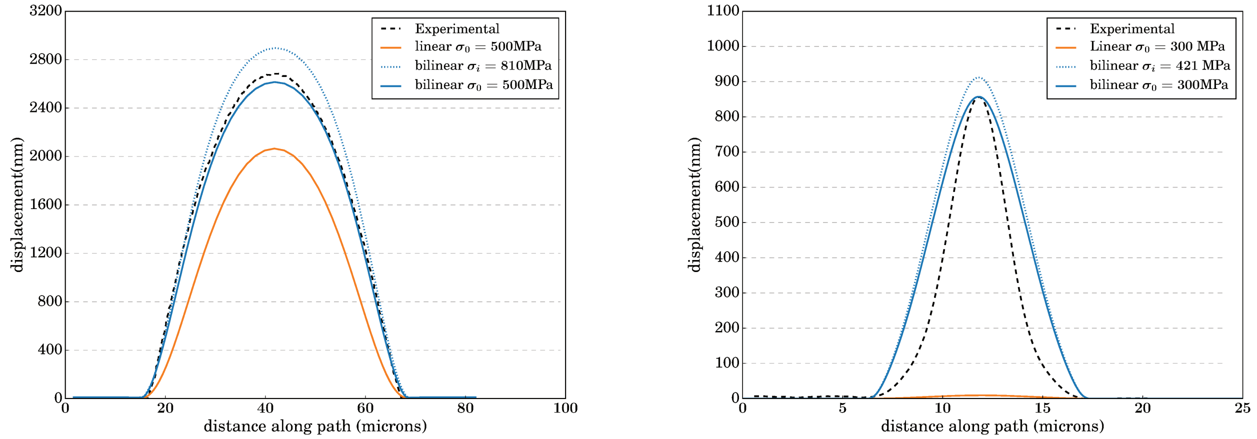

FIGURE 3.25: *Effect of non-monotonic loading on elastic-plastic buckling in the case of circular blister (left $\sigma_y = 800$ MPa) and straight blister (right $\sigma_y = 400$ MPa) (Ludwik strain hardening $K = 50$ MPa, $n = 0.25$)*

In order to have an idea of the height reached before stress relaxation, we plotted in figure 3.25 the intermediate state at σ_{max} in dotted line and the final state in plain line. We notice that for circular blister, the plane curve seem to match the experimental profile. However, in the case of straight blister,the experimental profile is different from the one predicted numerically, especially at the basis of the blister. The difference might be due to the absence of delamination in the present model.

To sum up, the non-monotonic loading model, that can be justified on physical grounds (physics of the deposition process), have shown promising results even-though it does not take into account thickness variation during the deposition process. It showed consistent results with experimental observations especially in the case of the circular blister. Nevertheless, in the case of the straight blister, the numerically obtained profile differs from the experimental one. This model can be enhanced by taking into account thickness variation during deposition process. It might also provide more accurate results if we account for a possible delamination between the film and the substrate. The later option will be examined in the next chapter.

3.4 Conclusion

In this chapter, we focused on the study of buckling of ductile thins films on rigid substrates, without delamination. We discussed the influence of plasticity on the buckling mechanism. We have first studied the influence of the ratio $\frac{\sigma_0}{\sigma_y}$ on the buckling of thin film subject to monotonic loading. We have evidenced that the elastic-plastic behaviour of the film causes higher deflections of the blister compared to the elastic case. In particular, the deflection of the blister is an increasing function of $\frac{\sigma_0}{\sigma_y}$. This behaviour is due to the increase in the plastic deformation levels and their concentration at the basis of the blister with increasing values of $\frac{\sigma_0}{\sigma_y}$. Another interesting observation is that for $\frac{\sigma_0}{\sigma_y} > 1$, we could cause the buckling of the film even if the value of residual stresses σ_0 are lower than the critical buckling stress derived in the frame of non-linear elastic mechanics. However, even for high values of $\frac{\sigma_0}{\sigma_y}$ and a finely meshed plate, the generic sinusoidal shape of the blister seems to be maintained. This last point is somehow treacherous as someone could conclude from the experimental observation of a blister profile on a ductile film that the linear elastic theory of buckling is valid for their particular system and deduce a wrong value of the stress in the film from the use of formula 1.10. However, as we showed in our analysis, a given value of the normalized buckle height δ/h can be associated to a whole set of σ_0 values depending on the yield stress in the film. So we can strongly recommend a nanoindentation test to estimate the yield stress, especially in the case of notoriously ductile films (e.g. gold, silver, copper).

Then, we have focused on the experimental cases and demonstrated that the use of monotonic loading with the experimental values of residual and yield stresses seems to be sufficient to form circular buckles with profiles that are (under certain conditions) sufficiently close to the the experimental case in terms of deflection and shape. However, in the case of the straight blister, the use of monotonic loading is not even enough to trigger the buckling of the film. In order to solve this issue, we proposed a model that takes into account the evolution of stress during the deposition of thin films by using non-monotonic loading. During the non-monotonic loading, the stress in the film first reaches linearly a maximum stress value σ_{max} which is slightly above the yield stress before decreasing until the final stress corresponding to the measurement of the final curvature. This method aims at triggering the buckling of the straight blister (because σ_0 is higher than σ_c). During the unloading of the film, the plastic deformation of the film helps maintain the structure of the blister which allowed as to generate buckling structures that have a similar maximum deflection to the experimental case.

The only issue that remained unsolved using an elastic-plastic buckling model is the elongated shape of the observed straight blister, since as discussed just above the addition of plasticity to the buckling problem does not seem to alter the generic sinusoidal shape of the blister. In order to solve this problem, we decided to account for delamination in the buckling model and study the influence of the interface along with the elastic-plastic behaviour of the film on the equilibrium shape of the blister.

Chapter 4

Coupling buckling, delamination and plasticity

Contents

Residual stresses in thin films can be a driving force for delamination. When the strain energy of a compressed film and the related energy release rate exceeds the interface toughness, the buckling of the thin film can occur concomitantly with the advancement of the crack front. This phenomenon is referred to as buckling-driven delamination and can result in various buckling shapes ranging from circular to telephone cord blisters [16]. Linear symmetric configurations, such as circular or straight-sided buckles [18, 71] are rarely observed experimentally and tend to destabilize into non-linear and asymmetric morphologies such as telephone cord buckles [71, 117], varicose (row of bubbles) [12, 41], wavy-circular buckles [30, 49] or more complex buckled configurations like snail-shaped buckles [18, 46] and branching blisters [43, 116]. Straight-sided and circular blisters are post buckling solutions of an initially flat plate, and are thus referred to as "primary buckling" equilibria. Some configurations enumerated above derive from a destabilization of the first buckling configurations themselves, ad are thus referred to as "secondary buckling" equilibria.

The growth and destabilization of buckling structures have also been investigated both analytically and numerically. Analytical studies enabled better understanding on the condition for buckling driven delamination [48]. By using a perturbation analysis, it has been evidenced that telephone cord blisters, varicose and wavy-circular blisters are manifestations of the configurational instability of the interface crack front of primary buckling structures [3, 4, 48, 49]. Numerical investigations by means of finite element method performed for elastic configurations has proven to be valuable in gaining insight on the mechanisms of thin film secondary buckling and in particular the role of interfacial toughness and mode mixity in the formation of secondary buckling [31, 32, 53]. This approach allowed the derivation of delamination morphology phase diagram in the case of elastic thin films on rigid substrates [53, 78].

In order to explain some observations such as the stability of circular blisters or the presence of snail-like structures in ductile thin films, assumptions of an elastic-plastic buckling-driven delamination [13, 17, 18] and of plasticity at the interface have been suggested [14]. Different approaches such as molecular dynamics, has been used to study the contribution of plasticity to the deformation of thin films during buckling [25, 26]. Other works, focused on studying the effect of interface plasticity on the buckling of thin films by mean of atomistic simulations [87, 88] and coupled finite-strain elasticity and phase-field modelling [89]. Up-to-date, in the frame of finite element analysis, elastic-plastic buckling of thin films has only been investigated by inducing a high folding angle to model the elastic-plastic behaviour of the film [46] and the the modelling of elastic-plastic buckling-driven delamination of thin films remains an open issue.

In this chapter, we will first present the mechanical model of elastic-plastic buckling-driven delamination of thin films and its underlying assumptions. We will mainly focus on presenting the constitutive laws used to describe the interface delamination and its implementation. Then, we will consider the typical case of the straight blister, and study the effect of plasticity on the buckling shapes and the energy equilibrium during its propagation.

Finally, we will consider the case of circular blisters and study the effect of plasticity on their propagation and destabilization.

4.1 Mechanical model

This section aims at presenting the mechanical problem of buckling-driven delamination of thin films and its numerical implementation. For the sake of clarity, our efforts will go towards presenting the problem of buckling-driven delamination of straight blisters. The main difference between the implementation of straight and circular blisters is strictly geometric and consists of the shape of the initial defect which is rectangular for straight blisters and circular for circular blisters. Further details concerning the two models are provided in the following subsections.

4.1.1 Presentation of the analytical problem

We consider an elastic-plastic thin film, deposited on a rigid substrate. The plasticity of the film is modelled using J_2 plastic flow theory with an isotropic hardening and the film is described as a $3D$ solid.

The interface between the film and the substrate is described by a cohesive model presented in section 4.1.2. In order to trigger the buckling delamination, a defect area of width $2b$ in the case of straight blisters (see figure 4.1) and of radius R in the case of circular blisters is introduced. These areas are not only debonded zones, they also exhibit a very small out of plane displacement ($\delta = 0.01\ h$) which triggers the buckling driven delamination of the film provided that the film presents enough residual stress.

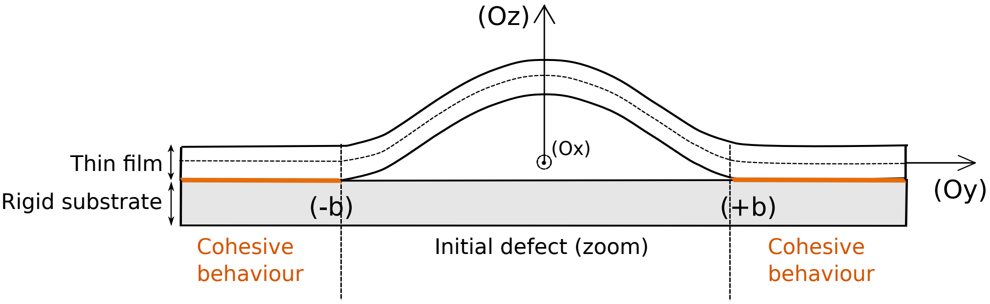

FIGURE 4.1: *Mechanical model of buckling-driven delamination of thin film on rigid substrate.*

The film is subjected to an initial isotropic compressive stress that mimics the residual stresses due to the deposition process. Due to the large values of the out-of-plane displacement of buckled structures, the analysis is carried out within the framework of large displacements using the Green Lagrange strain tensor.

4.1.2 Implementation of the numerical model

In this section, we present the finite element model used to analyse the effect of plasticity on buckling-driven delamination of thin films. Compared to the buckling model presented in chapter 3, the main difference consists in the implementation of a cohesive model to allow delamination of the film from the substrate along the interface. In the following section, we will thus mainly focus on the implementation of cohesive behaviour and mode mixity and provide only a quick reminder concerning the geometry, elastic-plastic behaviour, loading and boundary conditions.

Geometry,loading and boundary conditions

The film is modelled by a rectangular plate in the case of straight blister and by a squared plate in the case of circular blister to allow axisymmetric growth. The plate is deposited on a rigid substrate with an unilateral contact condition ($w(x,y) \geq 0$). Nodes that are part of the lateral edges parallel to x axis have fully built-in conditions. For the edges parallel to the y axis, the displacement is only allowed along the z axis and no rotation is allowed about the y and z axis (see figure 4.1).

The elastic-plastic behaviour of the thin film is modelled using a J_2 flow theory with an isotropic hardening law that is adapted for the elastic-plastic response of the film. The value of the yield stress is set according to the experimental results presented in section 2.2 while we investigate the influence of the hardening response (see section 3.1.2).

The loading consists of a thermal eigenstrain $\epsilon_{th} = \alpha_{th}\Delta T > 0$ applied uniformly to the plate ($\epsilon_{xx} = \epsilon yy = \epsilon_{th}$) at time $t = 0$. The magnitude of ΔT and the equibiaxial compressive stresses generated in the flat adherent part of the film are related by equation 3.8. The loading is performed following two steps:

- 1^{st} step: We perform a linearly increasing loading of the film until reaching the target value for internal stresses σ_0. The loading is performed fast enough to prevent the onset of buckling-driven delamination during the loading.
- 2^{nd} step: The beginning of this step corresponds to the time $t = 0$. The internal stress values have reached their final value σ_0 and buckling driven-delamination can thus occur under constant loading.

The aim of this strategy is to mimic at best experimental conditions where the buckling occurs usually after the deposition process, at a constant internal stress. Another similar method tested in this chapter consists of a two steps loading. During the first step, the film displacement in the out-of-plane direction is blocked to prevent any buckling. This constraint is released at the beginning of the second step, and the film can then buckle-delaminate under a constant compression stress.

The buckling is triggered thanks to a small out-of-plane imperfection of very small amplitude $0.01\ h$ of the film in the initial defect region. This region is rectangular in the case of straight blisters and circular in the case of circular blisters. It allows the nucleation of the delamination front during the 2^{nd} step.

In order to accurately capture plastic deformation, solid elements of a size smaller than $\frac{h}{5}$ are used (see the study conducted in Appendix A about the influence of mesh size on the plastic deformation distribution). Quadrilateral cohesive elements are used in order to model the interface behaviour. These elements are inserted along the interface between the film and the substrate except in the defect area. The upper surface of the cohesive elements is tied to the lower surface of the film, whereas the lower surface of cohesive elements has fully-built in condition since the substrate is rigid.

Cohesive zone implementation

An essential ingredient in the modelling of the buckling-driven delamination process is the description of the interfacial behaviour as damage is occurring between the film and the substrate. To do so, we chose to introduce cohesive elements between the film and the substrate. Cohesive element formulation is detailed in [21]. In this section, we will first introduce the formulation of a traction-separation law to describe the cohesive behaviour. Then we will explain the implementation of a mode mixity dependent interface energy.

Traction-separation law The interface constitutive law used for our model, consists of a bi-linear traction-separation relationship which represents the evolution of the traction $\vec{T}$ as a function of the relative displacement $\vec{\delta}$ between the two separating surfaces or "crack lips" as depicted in figure 4.2.

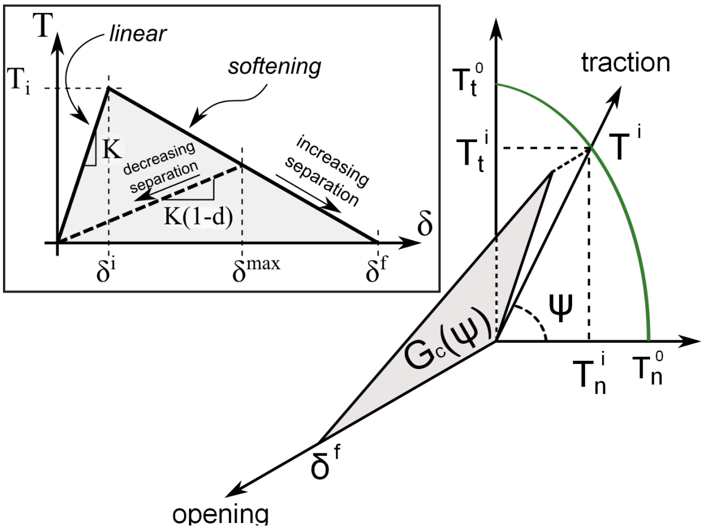

FIGURE 4.2: *Schematic representation of the linear traction-separation law used to model the interfacial damage occurring between the film and the substrate.The interfacial toughness is mode-mixity dependent ($G_c(\psi)$) and represents the total energy needed to break a cohesive element (grey area).*

Starting from the reference state where the two surfaces are perfectly bounded, the relationship between the traction and the opening δ stays linear and reversible until an initiation criterion is fulfilled (described bellow). This linear relationship writes:

$$\vec{T} = K\vec{\delta} \tag{4.1}$$

with K a spring constant, T the traction and δ the opening.

The nominal traction stress and corresponding opening vectors $(\vec{T}, \vec{\delta})$ can be decomposed into normal and shear components: The normal components (T_n, δ_n) are used to describe the normal opening process (mode I contribution), while their shear components (T_t, δ_t) are used to describe the shear opening process (mode II contribution). The traction component that corresponds to a mode III contribution can be neglected in comparison to mode I and mode II contributions.The amplitude T of the traction and δ of the separation writes:

$$\begin{cases} T = \sqrt{{T_n}^2 + {T_t}^2} \\ \delta = \sqrt{\delta_n^2 + \delta_t^2} \end{cases} \tag{4.2}$$

For the initiation, we chose to use a quadratic criterion. Thus, the peak traction T^i will be reached by any value of the traction $\vec{T^i} = (T_n^i, T_t^i)$ verifying[1]:

$$\left(\frac{< T_n^i >}{{T_n}^0}\right)^2 + \left(\frac{T_t^i}{{T_t}^0}\right)^2 = 1 \tag{4.3}$$

where T_n^0 is the maximum mode I traction and T_t^0 the maximum mode II traction.

Once the maximum traction is reached ($< T >= T^i$), debonding and irreversible damage takes place. Thus, if the condition expressed equation 4.3 is reached for any given combination of the traction components (T_n, T_t), irreversible damage will occur as the opening continues increasing .

To implement irreversible decohesion, linear softening is used by allowing the cohesive traction T to irreversibly and linearly decrease from T_i to 0 as the interfacial separation δ continues increasing from δ^i to δ^f. The softening can thus be expressed as a reduction of the cohesive zone stiffness K by a factor $(1-d)$ where d represents a damage variable. This leads to the formulation of the following definition for the cohesive traction during the softening:

$$T = K(1-d)\delta \tag{4.4}$$

the variable d is defined as

$$d = \frac{\delta^f}{\delta}\frac{\delta - \delta^i}{\delta^f - \delta^i}, \text{for } \delta > \delta^i \tag{4.5}$$

where δ is the amplitude of the opening as expressed in 4.2 and δ^i the amplitude of the opening at maximum traction T^i. $\delta = \delta^i$ corresponds to the onset of debonding while the separation between the two surfaces is complete at $\delta = \delta^f$.

Mode mixity As highlighted in section 1.3, mode mixity dependence of the interface energy is a necessary condition to understand the stabilization of growing buckles. Thus the separation energy per unit surface, $G_c(\psi)$, is assumed to follow a mixed mode dependency characterized by the following relationship:

$$G_c(\psi) = G_{Ic}(1 + \tan^2(\eta\psi)) \tag{4.6}$$

where G_{Ic} is the mode I separation energy, ψ the mode mixity angle and η a parameter that varies between 0 and 1 and characterizes the dependence upon mode mixity. When $\eta = 0$, the interface has a brittle-like behaviour, and as η increases, the dependence upon mode mixity increases. This means that it becomes much harder to break the interface in shear than in normal mode (see figure 4.3).

It should be noted that the definition of ψ we use here differs from the one classically used in linear elastic fracture which can only be expressed at a reference distance l ahead of the crack. The mode mixity angle definition we use here is $\tan(\psi) = T_t^i/T_n^i$ and can be expressed in any point of the interface as long as the separation process is not completed.

---

[1] Here, <> stands for the Macaulay brackets, which are leaving the quantity unchanged if positive, but return 0 when the quantity is negative. Indeed, a compressive value of the normal traction can not trigger damage.

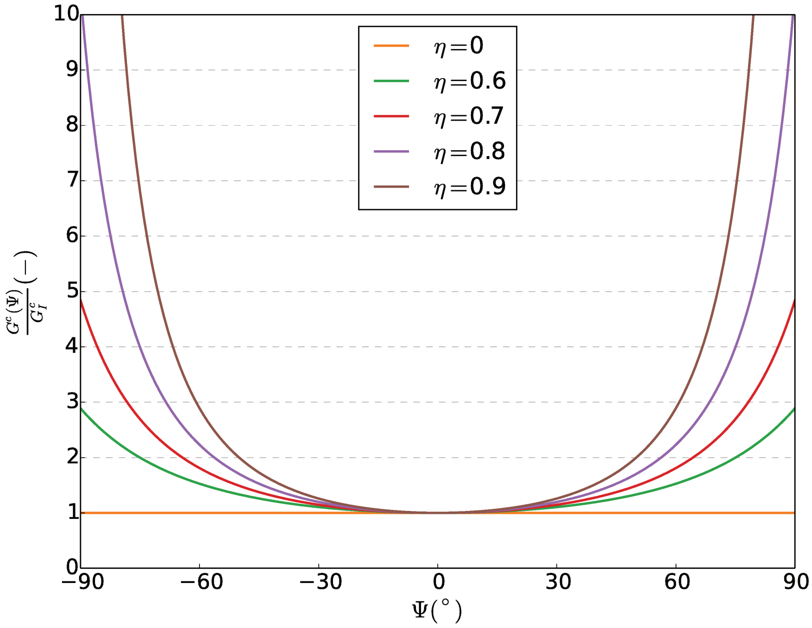

FIGURE 4.3: *Interfacial toughness ratio* $\frac{G^c(\Psi)}{G_I^c}$ *as function of the mode mixity angle* Ψ *for several values of* η

The parameters are interconnected by the shape of the bilinear traction separation law. The area beneath the triangle represented in figure 4.2 represents the interfacial separation energy as expressed bellow:

$$G_c(\psi) = \frac{1}{2}\delta^f T^i \tag{4.7}$$

where $T^i = \sqrt{T_n^{i\,2} + T_t^{i2}}$ is the amplitude of the maximum traction resulting from normal and shear tractions and δ^f the opening at which complete separation occurs.

4.2 Buckling-driven delamination of straight blisters

The aim of this part is to study and compare elastic and elastic-plastic buckling-driven delamination of thin films in the case of straight blisters. As observed in chapter 3, neither the elastic nor the elastic-plastic model of thin film buckling are able to capture the particular morphology of the straight blister observed experimentally and described in section 2.1.1. To do so, we will focus in the first subsection on studying elastic buckling-driven delamination of thin films deposited on rigid substrate. We will focus on studying the effects of cohesive parameters and mode mixity on the final morphology of the blister and the energy balance during the blister's propagation. In the second subsection, we will account for an elastic-plastic behaviour of the film and study the effect of plasticity on the morphology of the blister as well as the energy balance during the propagation. Eventually, we will compare profiles of blisters resulting from elastic-plastic buckling, elastic buckling-driven delamination and elastic-plastic buckling-driven delamination. We will also study the effect of cohesive zone parameters on straight blister's morphology. The last subsection will be dedicated to the study of the effect of the loading history on the morphology of straight blisters.

4.2.1 Elastic buckling driven delamination

The study presented in this subsection aims at understanding the effects of cohesive parameters and mode mixity on the process of buckling-driven delamination of thin films deposited on rigid substrate.

To do so, we implemented the numerical model presented in subsection 4.1.2. For the parameters, we fixed the material properties, the geometry of the plate and performed a parametric study with regards to interfacial properties. The fixed parameters are presented in table 4.1.

Elastic properties		Geometry				Loading	Interface
E (GPa)	ν (-)	h (nm)	$2b_0$ (µm)	L (µm)	l (µm)	σ_0 (MPa)	G_{Ic} (J/m^2)
85	0.44	400	9	135	1.2	700	0.3

TABLE 4.1: *Parameters used in the elastic buckling-driven delamination simulations. The described parameters are the following: Gold thin film elastic properties (E: Young's modulus, ν: Poisson's ratio), blisters geometries (h: thin film's thickness, 2b: blister's diameter, L: film's length, l: film's width), final residual stresses in thin film (σ_0) and mode I interfacial toughness (G_{Ic}).*

The elastic properties including Young's modulus (E) and Poisson's ratio (ν) are set as in chapter 3 and correspond to the gold thin film elastic properties. The thickness of the film is derived from the experimental measurements performed on sample (α) and presented in section 2.1. The length of the defect area is set to a smaller value than the final width of the experimental blister in sample α to allow some delamination before reaching the experimental width.

The thin film is modelled by a rectangular plate of solid elements. The length of the plate is set to $L = 40b_0$, which allows growth and propagation of the blister with little influence of the borders of the computational cell. As the solution is invariant along the x-axis (see figure 4.1), the width of the plate can be set to a small value to minimize calculation costs. We fixed the width to ($l = 0.25b_0$). To allow buckling, the final stress in the film is chosen to be larger than the corresponding critical stress ($\sigma_c = 637$ MPa). We set $\sigma_0 = 700$ MPa.

Concerning the value of mode I interfacial toughness of the 630 nm gold thin film on silicon substrate, no measurements of interfacial energy have been conducted within the frame of our experimental work. So, we chose values of G_{Ic} in accordance with the values found in literature. For instance, values of work of adhesion (W_A) of metal thin films on silicon are reported to be in the range of 0.2 to 5 J/m^2 in the literature [38, 109]. Other interesting examples include air-bonded gold thin film on sapphire for which the work of adhesion is reported to be between 0.6 and 0.9 J/m^2 [66, 82], and Cu/SiO_2 system with a $40 - 1000$ nm copper thin film thickness variation for which the interfacial toughness varies from 0.6 to $10\ \mathrm{J/m^2}$ [109]. In accordance with the results presented above, we set G_{Ic} to a relatively low adhesion ($G_{Ic} = 0.3\ \mathrm{J/m^2}$) which is a middle range adhesion regarding experimental values.

The remaining parameters including maximum mode I traction (T_n^0), maximum mode II traction (T_t^0) as well as the mode mixity dependence parameter η, will be subject to a parametric study to understand their effect on the propagation and the equilibrium profile of straight blisters.

Influence of the cohesive parameters on the morphology of the blister

For a matter of clarity, we chose in this section to study elastic buckling-driven delamination using only two different values of mode mixity dependence: $\eta = 0.65$ and $\eta = 0.7$. These values have been chosen in agreement with the study of plexiglass/epoxy interface mode mixity dependence which can be estimated to $\eta = 0.65$ [48]. In our case, modelling the interfacial behaviour with a mode mixity dependence parameter η of 0.6 or lower resulted a total delamination of the film. On the contrary, choosing values higher or equal to $\eta = 0.75$ resulted in little delamination ($b_f < 0.1 b_0$) which does not allow interface damage study. These observations can be confirmed by the diagram presented in figure 4.4. The graph presents the evolution of the ratio $\dfrac{G_c(\Psi)}{G_{Ic}}$ as function of the mode mixity angle Ψ for several values of η ranging form 0.6 to 0.9. The horizontal dotted line represents the ratio $\dfrac{G_0(\Psi)}{G_I^c}$ (see equation 1.40) calculated using the parameters presented in table 4.1. We can notice that for $\eta = 0.6$, $\dfrac{G_c(\Psi)}{G_{Ic}} \leq \dfrac{G_0(\Psi)}{G_{Ic}}$, which means that the blister can propagate indefinitely. On the contrary, for high values of η (for example $\eta = 0.9$), the horizontal line $\dfrac{G_0(\Psi)}{G_I^c}$ intercepts the toughness curve at small values of mode mixity angle ($\Psi \leq 60°$) which means that the propagation stops at smaller values of b_f.

Concerning the values of maximum tractions, we fixed the maximum mode I traction T_n^i to an arbitrary value of 75 MPa which corresponds to a critical normal opening δ_n^f of $2\%h$ and we varied the values of maximum mode II traction T_t^0. The values chosen for T_t^0 are 80 MPa and 120 MPa. In the case of $\eta = 0.65$, these values correspond to a critical shear opening δ_n^f of $5\%h$, $3\%h$ and $2\%h$ respectively.

The different profiles are presented in figure 4.5. The blue curves correspond to an interfacial mode mixity dependence of 0.65, while the red curves correspond to an interfacial mode mixity dependence of 0.6.

According to equation 1.35, the interfacial toughness $G_c(\psi)$ is a monotonously increasing function of η for a given mode mixity angle. This means that it is harder to break the interface in the case $\eta = 0.7$ compared to the case $\eta = 0.65$ and explains why the delamination area is more important in the blue curves compared to the red ones. Let us consider now a given value of η, for instance 0.65. We notice that as the value of maximum shear traction

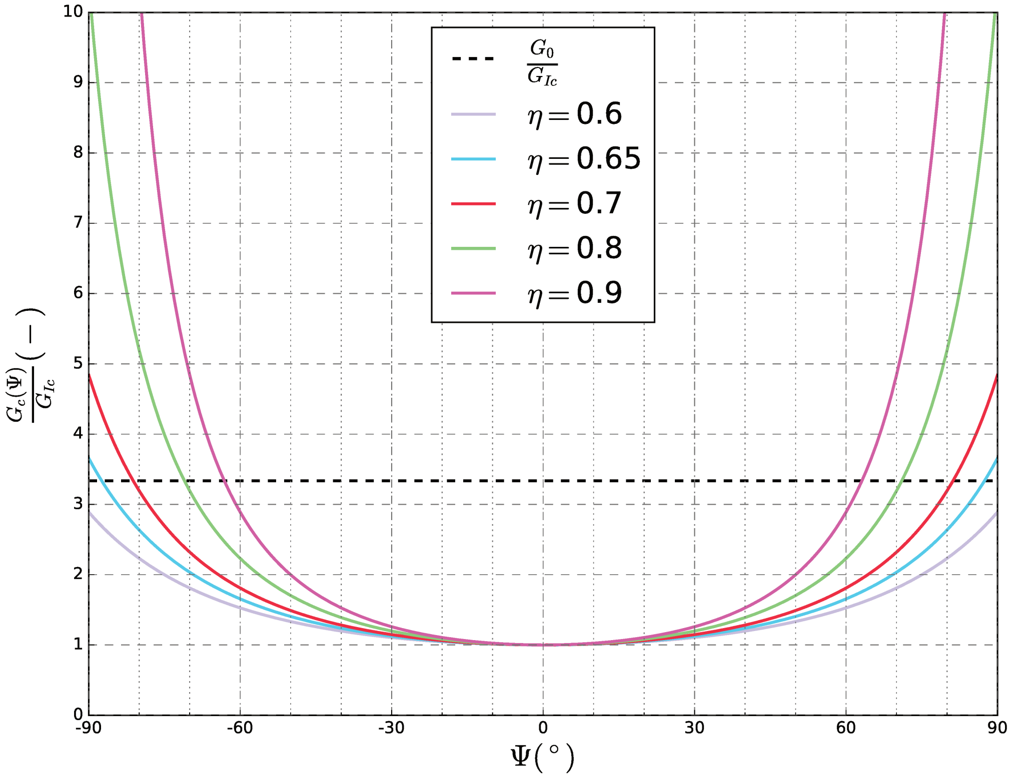

FIGURE 4.4: *Interfacial toughness ratio* $\frac{G_c(\Psi)}{G_{Ic}}$ *as function of the mode mixity angle* Ψ *for several values of* η

decreases, the final delamination area increases [2].

Another important parameter linked to T_t^0 value is the length of the process zone l_{PZ}. The different values of l_{PZ} for the case of $\eta = 0.65$ are gathered in table 4.2 and are expressed in term of fraction of the final half-width of the blister. We can notice that as T_t^0 decreases, the length of the process zone increases. As observed by Faou in [30], taking smaller values of T_t^0 while keeping the same definition of $Gc(\psi)$ leads to a bigger opening slip at the interface (i.e. bigger values of δ_t along the process zone). In this configuration, the cumulated slip along the process zones causes the blister height to increase significantly.

T_t^0 (MPa)	80	120
l_{PZ} (% $\mathrm{b_f}$)	12	9

TABLE 4.2: *Summary of the process zone length as function of* T_t^0 *for the case of* $\eta = 0.65$.

In order to avoid large deviation from the analytical solution of elastic buckling, we chose to work with process zone lengths lower than 10% $\mathrm{b_f}$ which corresponds to either

---

[2] To discard any mesh size dependency, we have rerun the simulation corresponding to $T_t^0 = 120$ MPa with 100 times more elements in the film and the CZ. The comparison showed no significant difference in the final morphology or in the total delamination areas.

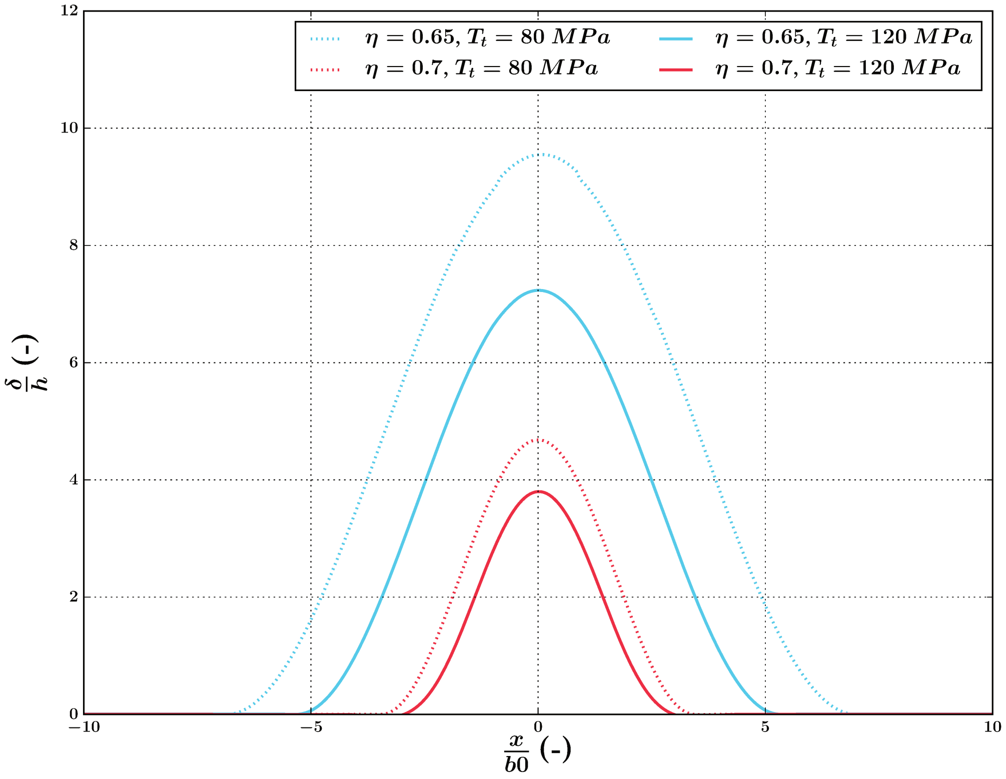

FIGURE 4.5: *Equilibrium profiles of different elastic buckling-driven delamination conditions. The y-axes represents normalized deflection* $\frac{\delta}{h}$*, where* δ *is the out-of-plane displacement of the film and* h *the thickness of the film (fixed). The straight blisters presented are obtained for the same final stress* $\sigma_0 = 700$ MPa*, mode* $- I$ *interfacial toughness* $G_{Ic} = 0.3\ \mathrm{J/m^2}$ *and maximum normal traction* $T_n = 75$ MPa*. The varied parameters are mode mixity dependence* η *and maximum shear traction* T_t^0*.*

$T_t = 120$ MPa in the case of $\eta = 0.65$. The parameter T_t^0 is thus set to 120 MPa in the following simulations.

Energy balance

The aim of this section is to check the accuracy of the solutions obtained using our elastic buckling-driven delamination model with the parameters specified above. To this end, we chose to consider two elastic buckling-driven cases with identical geometries, material properties and loadings but different interface responses particularly in terms of mode mixity dependence ($\eta = 0.65$ and $\eta = 0.7$).The maximum normal and shear tractions are given by $(T_n^0, T_t^0) = (75, 120)$ MPa and the remaining parameters are specified in table 4.1. The buckling profiles of these cases correspond to the plain red and blue curves in figure 4.5.

In the case of the buckling-driven delamination of an elastic film deposited on a rigid substrate, the energy conservation can be expressed in the following way:

$$E_e + E_{sep} = E_{tot}. \tag{4.8}$$

where E_e is the elastic energy of the film, E_{sep} the damage fracture dissipated at the interface and E_{tot} the total energy of the system.

The elastic and interface damage energy as well as their sum are presented in figure 4.6 for each of the cases $\eta = 0.65$ and $\eta = 0.7$.

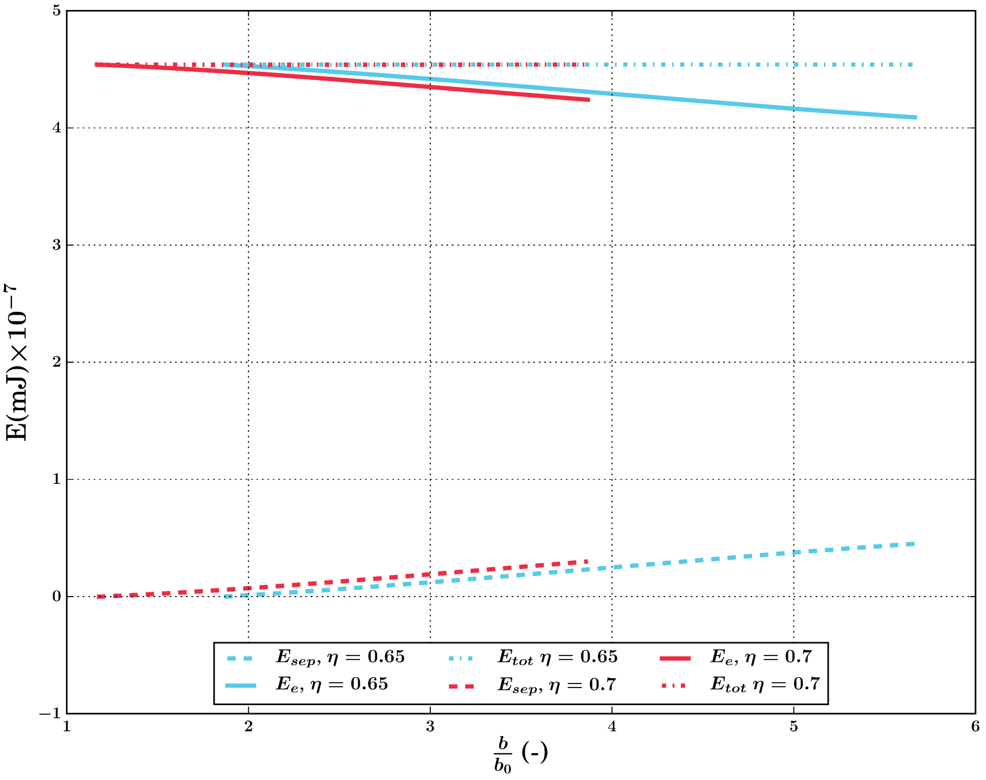

FIGURE 4.6: *Energy as a function of the normalized position of the crack front* $\frac{b}{b_0}$, *where* b *is the half width of the blister and* b_0 *the half width of the initial defect.* E_e *represents the elastic energy and* E_{sep} *the energy used to fracture the interface.*

Let us first examine the general tendencies of the separation and elastic energy. As explained in section 4.1.2, the stress loading of the system is performed so that the buckling-driven delamination process occurs at constant loading and thus constant total energy. Thus, as the crack front advances, the energy used to fracture the interface E_{sep} increases while the elastic energy stored in the system E_e is consumed. These observations are consistent with the curves presented in figure 4.6. We can notice that for both case studies $\eta = 0.65$ and $\eta = 0.7$, the separation energies increase with $\frac{b}{b_0}$ while the elastic energy decreases with $\frac{b}{b_0}$. We can also notice that the sum of the elastic E_e and separation E_{sep} energies in the case $\eta = 0.65$ and $\eta = 0.7$ are equal and remain constant during the blister's propagation. The energy balance equation (eq. 4.8) is thus verified in the case of elastic buckling-driven delamination.

Another interesting observation concerns the energy values. When comparing for instance the fracture energy values during propagation for cases $\eta = 0.65$ and $\eta = 0.7$, it

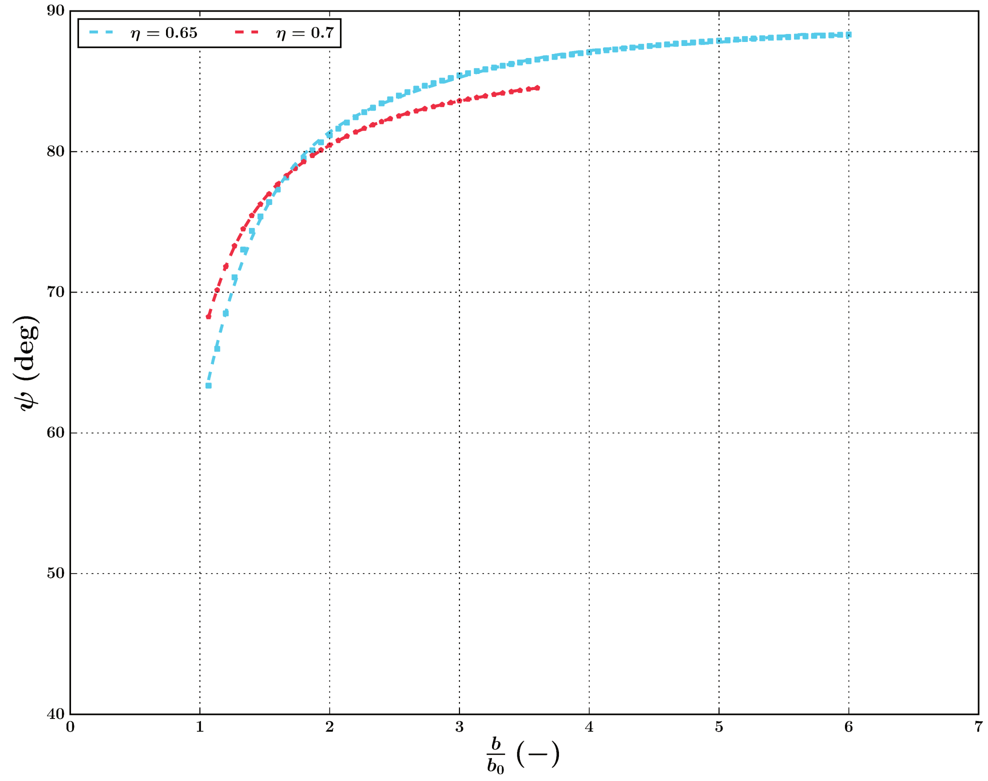

FIGURE 4.7: *Mode mixity angle ψ as a function of the normalized position of the crack front $\frac{b}{b_0}$, where b is the half width of the blister and b_0 the half width of the initial defect.*

seems that these curves are superimposed which means that for a given loading, the same energies are spent during the advancement of the blister's front. This observation might give place to the following question: if the same fracture energy is spent in both cases then why does the propagation stops in the case $\eta = 0.65$ while it continues further in the case $\eta = 0.7$? The key ingredient in answering this question is the mode mixity dependence parameter. Indeed, as depicted in figure 4.4, the horizontal line of $\frac{G_0}{G_{Ic}}$ intercepts the curve of $\frac{G_c(\psi, \eta = 0.7)}{G_{Ic}}$ at $\psi \simeq 81°$ while it intercepts the curve $\frac{G_c(\psi, \eta = 0.65)}{G_{Ic}}$ at $\psi \simeq 88°$. This, means that for $\eta = 0.65$ and $\eta = 0.7$ the blister's propagation stops at the half width b corresponding to $\psi \simeq 87°$ and $\psi \simeq 81°$ respectively.

To check if the value of the mode mixity angle ψ at equilibrium point complies with the analytical predictions, we measured the mode mixity angle locally at the crack front during propagation using the energy criterion, which is readily recovered by using output data in the followign way: $\psi = \frac{1}{\eta} \arctan\left(\sqrt{\frac{G_c}{G_{Ic}} - 1}\right)$. The curves $\psi = f(\frac{b}{b_0})$ for $\eta = 0.65$ and $\eta = 0.7$ are plotted in figure 4.7.

To conclude, the energy and mode mixity angle studies allowed the comparison between the analytical predictions and the corresponding numerical results in the case of elastic buckling-driven delamination. The cohesive zone model with mode mix dependency shows good consistency with the linear elastic fracture mechanics approach, both qualitatively and quantitatively.

4.2.2 Choice of element and integration type in the case of buckling driven delamination

The aim of this section is to determine the appropriate element type and numerical integration method for the study of buckling-driven delamination of thin films with an elastic-plastic behaviour.

Limits of implicit approach

According to the study presented in appendix A, solid quadratic bricks (C3D20) seem to capture accurately the elastic plastic deformation at the basis of the buckle compared to quadratic tetrahedrons (C3D10) or continuum shell elements (linear interpolation). Thus we decided at first to test the same elements (quadratic bricks) along with implicit method as in chapter 3.

It should be noted that the problem of buckling-driven delamination has $four$ sources of non-linearity rather than $three$:

- Geometric non-linearities due to the large values of the out-of-plane displacement. This type of non-linearity can be accounted for by performing the calculations within the framework of large displacements using the Green Lagrange strain tensor.
- Unilateral buckling, i.e. the equilibrium must satisfy $\omega > 0$ on the whole film domain. This is done by implementing a rigid contact between the film and the substrate.
- The elastic-plastic behaviour of the film.
- The bi-linear traction-separation law that describes the cohesive behaviour of the interface

In particular, the debonding part of the traction-separation law, may cause convergence difficulties at the point where the crack first initiates. To avoid these instabilities, a viscous regularization of the constitutive equations defining cohesive behaviour can be used [21]. This regularization scheme works by introducing a viscous damage variable d characterized by a relaxation time of the viscous system μ which provides a dissipating mechanism during unstable debonding. When used, values of viscosity should be chosen much smaller than the total time step τ in order to ensure the convergence of the model without compromising the results [40]. The amount of energy associated with viscous regularization should also remain small compared to the total energy of the system ($< 1\%$) to ensure the accuracy of the solution.

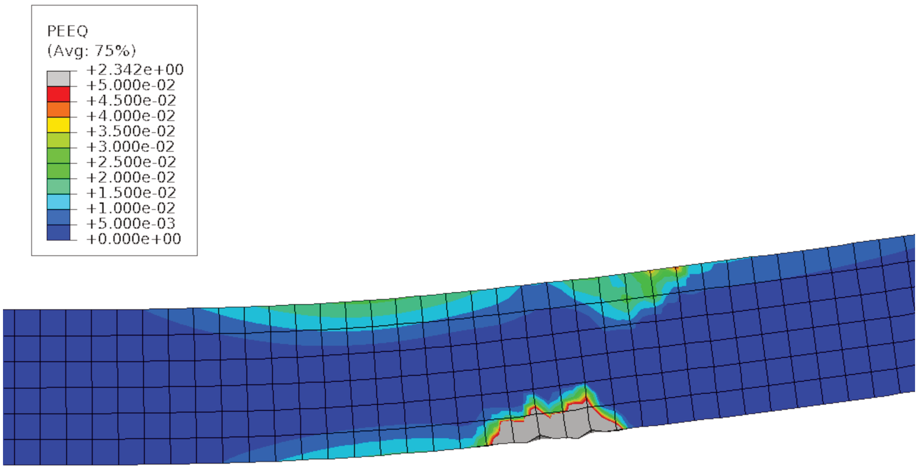

FIGURE 4.8: *Equivalent plastic strain mapping obtained at the last increment before non-convergence for an implicit analysis for a buckling-driven delamination problem using* $3D$*, quadratic bricks. The loading conditions are the follow:* $\sigma_0 = 700$ MPa*,* $\sigma_y = 720$ MPa*,* $K = 50$ MPa *and* $n = 0.25$*. The remaining parameters are specified in table 4.1.*

In our case study, we tested values of μ ranging from $10^{-4}\ \tau$ to $10^{-1}\ \tau$, where τ is the total time step. Despite the use of viscous regulation, numerical instabilities seem to persist during the debonding of the interface causing high concentration of plastic deformation and severe distortion of solid elements. For instance, in figure 4.8, we present a mapping of the equivalent plastic strain obtained at the last increment before non convergence of a buckling-driven delamination simulation. The geometry, the elastic-plastic properties, the interface properties as well as the loading are detailed in table 4.3. A viscous relaxation time $\mu = 10^{-3}\ \tau$ was used.

Geometry		Elastic properties		Hardening		
h (nm)	$2b_0$ (µm	E (GPa)	ν (-)	σ_y (MPa)	K (MPa)	n (-)
400	9	85	0.44	720	50	0.25

Interface				loading
G_{Ic} (J/m^2)	η (-)	T_t^i (MPa)	T_n^i (MPa)	σ_0 (MPa)
0.3	0.65	120	75	700

TABLE 4.3: *Summary of the parameters' values used in the modelling of elastic-plastic buckling-driven delamination.*

We can notice in figure 4.8 that the equivalent plastic strain reached in this case extremely high values (234%) near the interface which caused the distortion of the elements. Similarly, the cohesive elements showed also some distortions (hourglass effect) and their traction-separation response is not consistent with the implemented traction-separation law as specified in figure 4.9. It should be noted that similar distortion levels were obtained for other values of viscous relaxation time and even for higher values of σ_y including $\sigma_y = 850$ MPa. However, such a distortion problem does not seem to occur in the cases of buckling-driven delamination of purely elastic thin films using the same viscous regulation ($\mu = 10^{-3}\ \tau$).

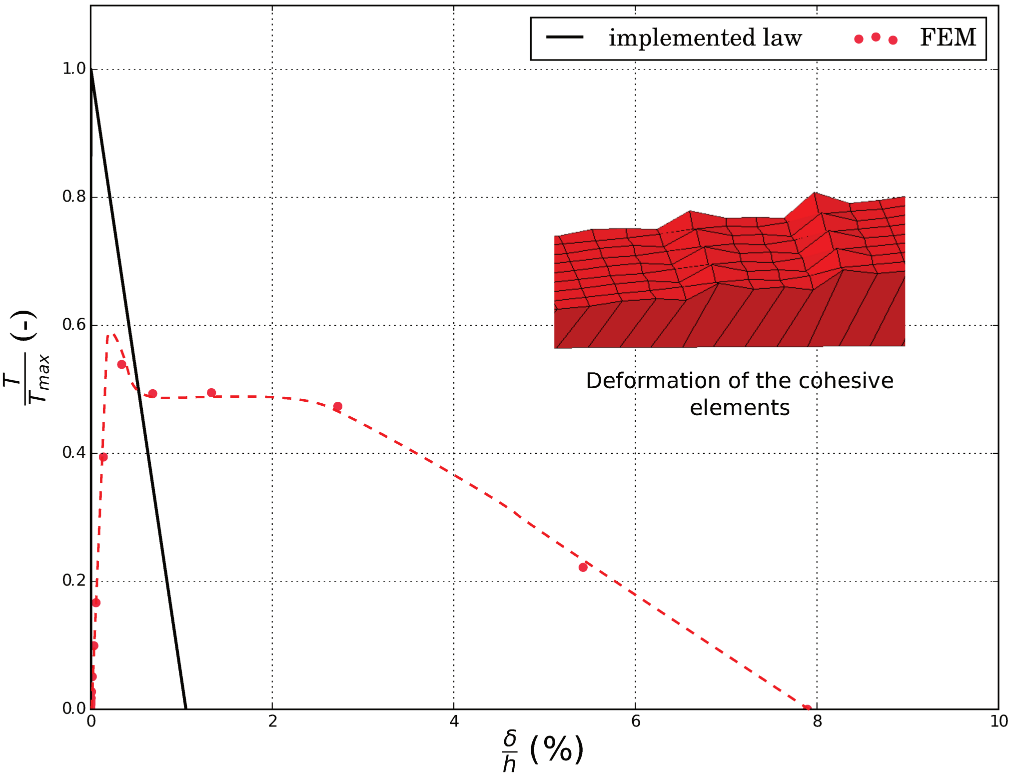

FIGURE 4.9: *This graph features the implemented cohesive law and the corresponding cohesive response obtained via FEM implicit analysis with a time step* $\tau = 0.1$ *and a viscous relaxation time of* $\mu = 1.e{-}4$. *The graph also shows the state of cohesive elements in contact with the distorted* $3D$ *elements showed in figure 4.8.*

The cause of this distortion is thus likely due to a combination of the non-linear response of the cohesive elements and that of the solid elements.

Explicit analysis

Even though the buckling-driven delamination is a static problem, it involves a contact and has high non-linearities. So, it can be solved more efficiently with an explicit solver [21] in which inertia effects are considered. Indeed, in the explicit procedure, a central-difference time integration scheme is used and there is no need to reconstruct and invert the global mass and stiffness matrices unlike the implicit method. Increments in explicit procedure are thus relatively less costly compared to an implicit analysis even if the method is not conditionally stable and needs thus smaller increments to ensure the accuracy of the solution.

It should be noted however that the explicit procedure in Abaqus offers fewer element types compared to implicit procedure. In particular, second order bricks (C3D20) are not available in explicit procedure. Only first order bricks including solid (C3D8) and shell elements (SC8R) as well as second order tetrahedron are available. The aim of this section is to determine the most suitable element types from the above in terms of the accuracy of the solution and the computational cost. To this end, we tested the different element types

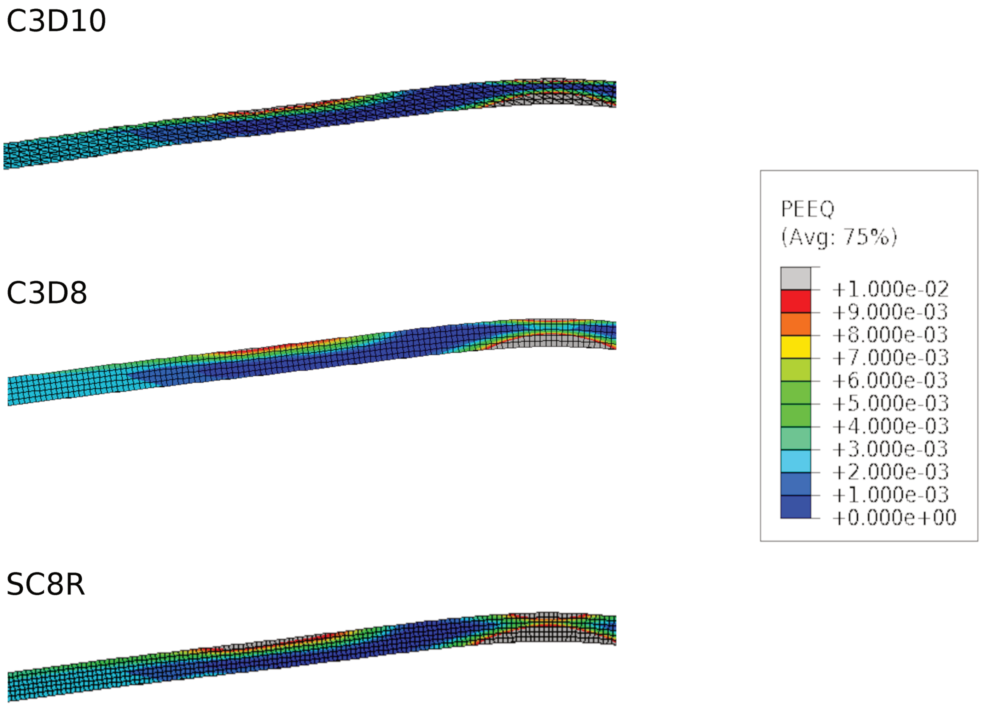

FIGURE 4.10: *Equivalent plastic strain mapping obtained using quadratic tetrahedrons (C3D10), linear bricks (C3D8) and linear shell elements (SC8R) in the frame of explicit integration scheme.*

available in the explicit library and compared their respective equilibrium solutions and computational costs.

We aim at making quasi-static calculation within a dynamic framework. To ensure that the damage of the cohesive elements is controlled by the plate displacement, we chose to set the values of cohesive elements mass density 100 times smaller than that of the plate. Also, a possible way in the framework of dynamic analysis to increase the stable time increment is to artificially increase the material's density. This method is known as 'mass scaling'. It is necessary to verify a posteriori that the inertial forces are small compared to the mechanical ones and restricted to a localized region.

An important issue encountered when implementing a dynamic analysis is the presence of vibrations of the plate due to the second order derivative (acceleration). The use of high loading rates to ensure that the delamination of the film occurs at constant residual stresses plays an important role in the occurrence of these vibrations. The dynamic effects can be damped out by implementing a "viscous pressure" to the plate. The value of the viscous pressure should be set carefully to ensure low values of kinetic energy (less than 1% of the total energy) without compromising the accuracy of the solution by the presence of large viscous dissipation terms.

Once the different parameters tuned, we performed the same explicit finite element calculations using first order and second order elements. The geometry, the elastic-plastic properties, the interface properties as well as the loading are identical to those used in section 4.2.2 and are detailed in table 4.3. The final equilibrium profiles as well as the equivalent plastic strain mapping are presented in figure 4.11 and figure 4.10 respectively.

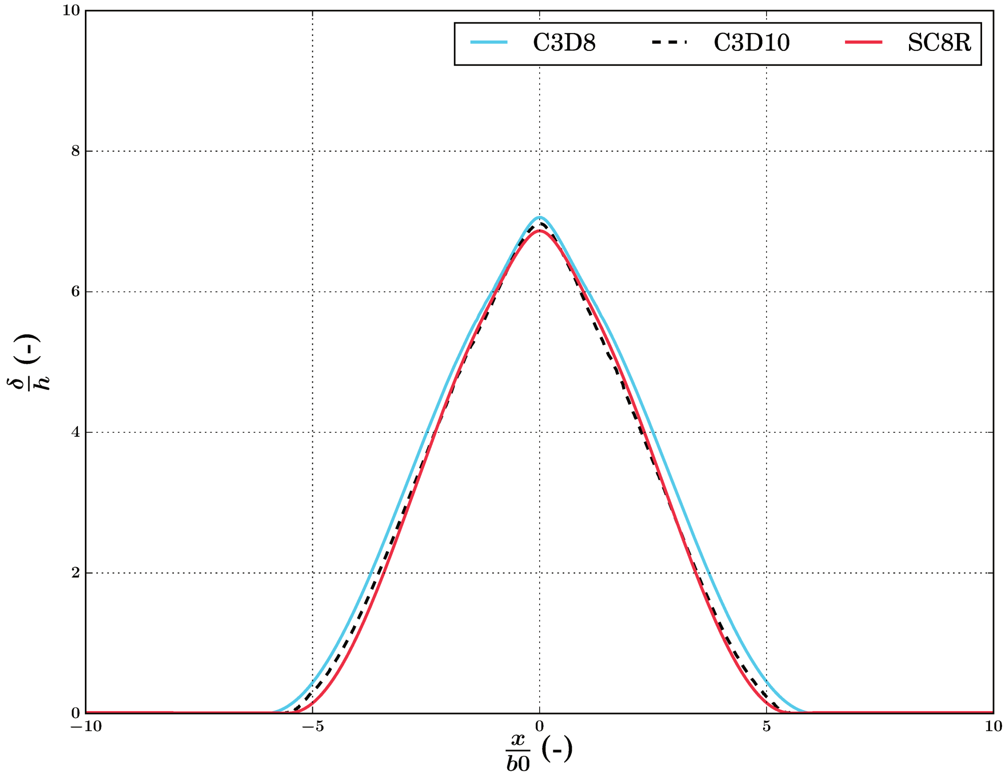

FIGURE 4.11: *Comparison between the equilibrium profiles obtained using quadratic tetrahedrons (C3D10), linear bricks (C3D8) and linear shell elements (SC8R) in the framework of explicit integration scheme. The corresponding parameters are presented in table 4.3*

The equivalent plastic strain distributions have similar patterns and values in the case of linear and quadratic elements. In the three cases, the maximum plastic strain is reached at the part of the film corresponding to the initial defect area and corresponds to a value of approximately 2%. The plastic distribution is thus quite different from the pure buckling case where the maximum deformations are reached at the folding angle of the blister. Furthermore, the equilibrium profiles corresponding to the linear and quadratic elements are also very similar and seem to have a sharper tip compared to the sinusoidal elastic buckling shape.

To conclude, in the frame of dynamic analysis and given that a sufficient number of elements through thickness is used (at least 5 as explained in appendix A), there is little difference between equilibrium states using linear or quadratic elements. The only significant difference lies in computational costs that are minimized in the case of shell elements. In the following sections, we will thus mainly use a stack of at least 5 shell elements through thickness along with an explicit dynamic analysis. However, when changing the loading cycles or boundary conditions, the results are always double checked using quadratic tetrahedrons.

4.2.3 Elastic-plastic buckling-driven delamination using linear loading

The aim of this section is to study the influence of plasticity on the growth and the final morphology of straight blisters. To this end, we will first study the influence of different values of the yield stress (or different values of the ratio $\frac{\sigma_0}{\sigma_y}$) on the final morphology of a straight blister under a fixed loading σ_0. We will then try to explain the difference in the final equilibrium shape between elastic and elastic-plastic thin film by comparing their energy balance during the propagation of the blister and by examining the values of mode mixity angles ψ at the crack front. Eventually, we will study the effect of plasticity on the onset of buckling-driven delamination and determine under which conditions buckling-driven delamination can occur in configurations with compressive residual stress σ_0 lower than the critical buckling stress σ_c computed for an elastic film.

In this section, we will exclusively use a linearly increasing loading. Simulations are usually composed of two steps:

- 1^{st} step: we perform linear loading of the film until reaching the target value for internal compressive stress of amplitude σ_0. The loading is performed fast enough to prevent the onset of delamination during the loading. The loading rate should however be performed at reasonable rate to avoid undesirable dynamic effects.
- 2^{nd} step: the beginning of this step corresponds to the time $t = 0$ of delamination. The internal stress values have reached their final value σ_0 and buckling driven-delamination can thus occur under constant loading.

Influence of yield stress on the morphology of the blister

To study the influence of the yield stress on the morphology of straight blisters, we chose to work with a single value of internal stresses σ_0 and vary the yield stress to obtain different $\frac{\sigma_0}{\sigma_y}$ values. The values tested range from 0.5 to 1. The parameters used to model the decohesion between the film and the substrate are the same as those used in the previous section and are given in the table below.

The different blisters' profiles are presented in figure 4.12 for the case $\sigma_0 < \sigma_y$ along with the profile of a purely elastic that serves as a reference. The plasticity seems to modify the equilibrium profile. Indeed, the upper part of the blister (its peak) seems to be sharper in the case of elastic-plastic buckling. This is likely due to the plastic deformation that is mainly concentrated at the top and the base of the straight blister as shown in figure 4.13. As the ratio $\frac{\sigma_0}{\sigma_y}$ decreases, the influence of plasticity is less important and the maximum value of equivalent plastic deformation decreases. This results on a rounder tip of the blister.

Geometry		Elastic properties		plasticity		
h (nm)	$2b_0$ (µm	E (GPa)	ν (-)	σ_y (MPa)	K (MPa)	n (-)
400	9	85	0.44	variable	50	0.25

Interface				loading
G_{Ic} (J/m^2)	η (-)	T_t^i (MPa)	T_n^i (MPa)	σ_0 (MPa)
0.3	0.65	120	75	700

TABLE 4.4: *Summary of the parameters' values used in the modelling of elastic-plastic buckling-driven delamination.*

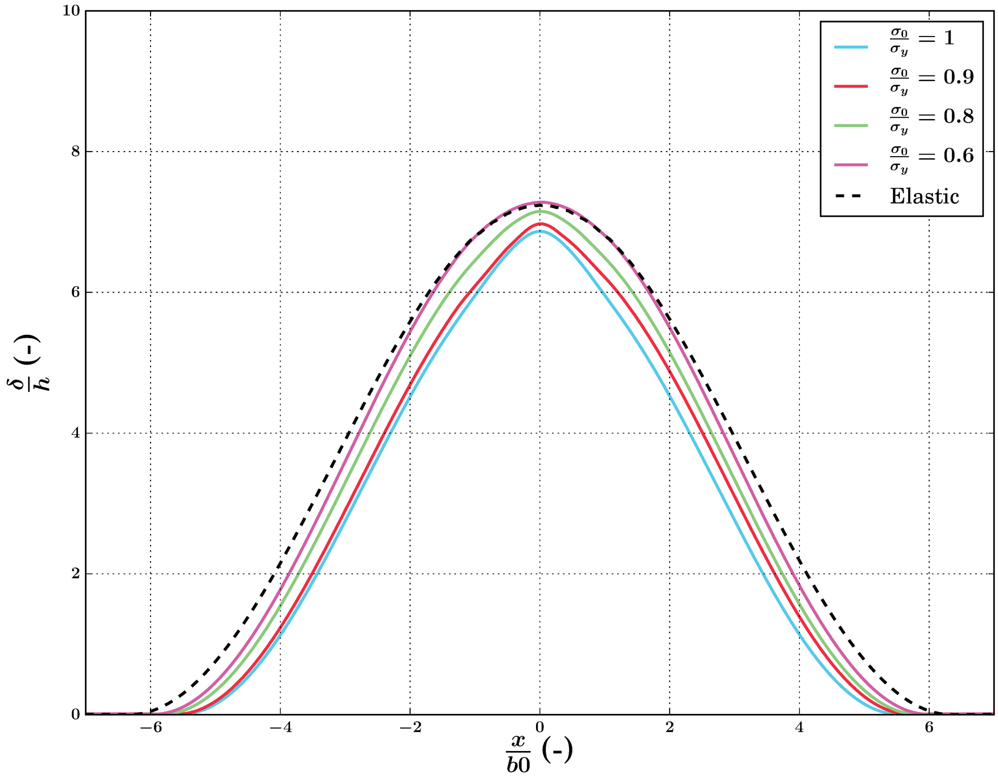

FIGURE 4.12: *Influence of plasticity on the equilibrium profile of straight blisters obtained by means of buckling-driven delamination. The parameters used are those given in table 4.4.*

For instance, in the case $\frac{\sigma_0}{\sigma_y} = 1$ the maximum equivalent plastic deformation is equal to approximately 2% and the tip of the blister is much sharper than in the case $\frac{\sigma_0}{\sigma_y} = 0.8$ for which the maximum equivalent plastic deformation reaches roughly 1%.

For $\frac{\sigma_0}{\sigma_y} = 0.5$, plasticity seems to play marginal effect and the equilibrium profile of the corresponding blister is very close to the equilibrium profile of the elastic case. It should also be noted that plasticity seems to cause the stabilization of the blister at final $2b_f$ lower than that of the elastic case.

Another interesting point comes from the comparison between the influence of plasticity in the case of pure buckling (i.e. without delamination) and in the case of buckling-driven

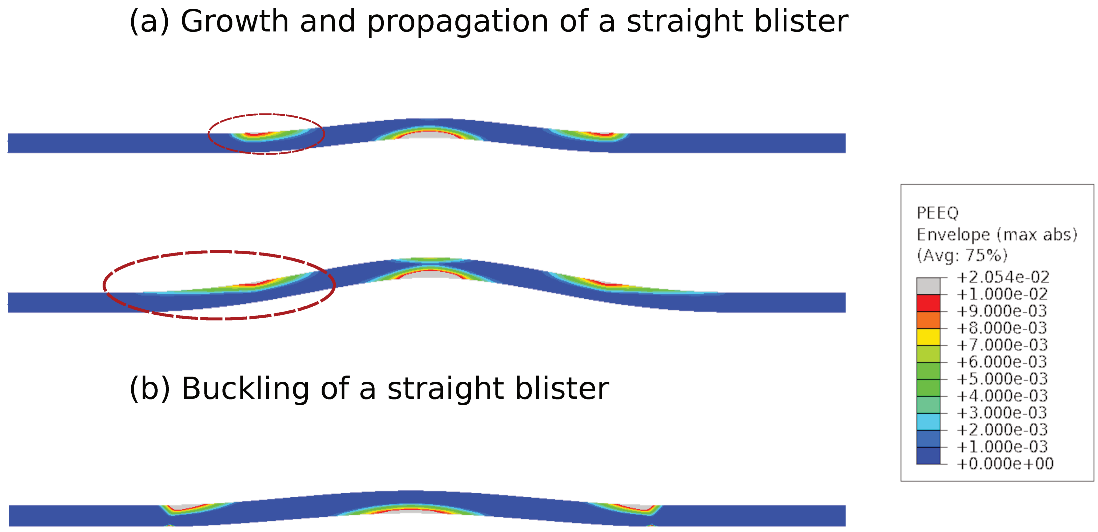
(a) Growth and propagation of a straight blister

(b) Buckling of a straight blister

FIGURE 4.13: *Equivalent plastic deformation mapping in the cases of pure buckling (a) and buckling-driven delamination (b). Both results were obtained for the same load and elastic plastic behaviour. We have $\sigma_0 = \sigma_y = 700$. The remaining parameters are detailed in table 4.4.*

delamination. In figure 4.13, we considered two different cases of buckling and buckling-driven delamination of a ductile thin film. The two plates have the same geometric defect and are submitted to the same loading $\sigma_0 = 700$. Both plates have an elastic-plastic response governed by Ludwik hardening with the parameters detailed in table 4.4. The value of maximum plastic deformation is similar in both cases and is around 2%. In the case of pure buckling, the plastic deformation is confined in a small area at the folding angle and near the tip of the blister. It appears at the early stage of buckling and does not evolve subsequently. Conversely, in the case of buckling-driven delamination, the plastic deformation develops at the basis of the blister and seems also to develop completely through the thickness at the tip of the blister unlike the pure buckling case. Also, in the case of buckling-driven delamination, plastic deformation does not develop only during the early stage of buckling. It also spreads as the buckle delaminate causing thus more plastic dissipation than in the purely buckling case.

The continuously growing plastic deformation especially at the first stages of delamination seems to limit the propagation of the blister. In order to gain a better insight about the mechanism leading to the limitation of the propagation of the blister, we perform an energy study presented in the next section.

Influence of plasticity on the energy balance of the system In order to gain insight into the mechanism of elastic-plastic buckling-driven delamination, we propose to study the energy balance during the propagation of the blister in both cases. We consider two plates with identical geometry. The loading and interface parameters are also identical and detailed in table 4.4. The only difference is the elastic-plastic response of the thin film. The first one is elastic while the second on has an elastic-plastic response characterized by Ludwik hardening with $\sigma_y = 700$ MPa, $K = 50$ MPa and $n = 0.25$. During the 2^{nd} step during which the propagation takes place, we measure at each increment the radius of the delaminated area of the film, the elastic energy that is available E_e, the total separation energy E_{sep} dissipated at the interface and the total energy dissipated plastically in the film E_p. These curves are presented in figure 4.14 for the elastic and the elastic-plastic cases.

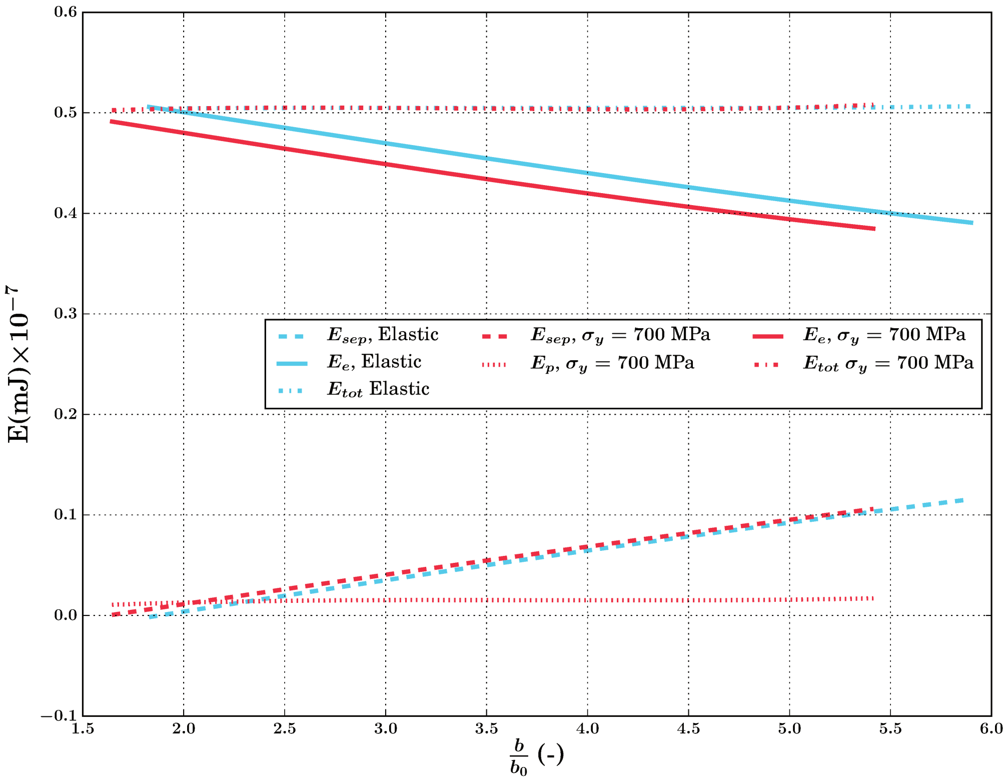

FIGURE 4.14: *Energy as a function of the normalized position of the crack front* $\frac{b}{b_0}$*, where* b *is the half width of the blister during propagation and* b_0 *the half width of the initial defect.* E_e *represents the elastic energy,* E_p *the plastic energy and* E_{sep} *the energy used to fracture the interface. The figure feature two cases: purely elastic thin film (*$\sigma_0 = 700$ MPa*) and elastic-plastic thin film (*$\sigma_0 = \sigma_y = 700$ MPa*).*

We can notice in the case of elastic buckling-driven delamination that the energy used to delaminate the interface does increase during the propagation of the blister causing the elastic energy to decrease. The sum of the elastic and separation energies is also constant through the propagation and is equal to the total energy.

In the elastic-plastic case, the dissipated plastic energy is positive and does not increase significantly during the propagation. This is due to the fact that most of the plastic energy is dissipated during the buckling of the film that occurred in the first step. Conversely, the energy dissipated at the interface does increase during the propagation of the blister and its curve is very similar to the curve of E_{sep} in the elastic case. Finally, the elastic energy decreases during the propagation of the blister and shows a negative shift compared to the corresponding curve in the elastic case. This shift is due to the presence of the plastic dissipation.

Thus, considering the energies dissipated globally does not provide a clear explanation of the origin of the stabilization of elastic-plastic buckling structures at smaller width. The explanation to this behaviour comes when considering the energy dissipated locally at the crack front and calculating the corresponding mode mixity angle ψ given by $\psi = \frac{1}{\eta}\arctan\left(\sqrt{\frac{G_c}{G_{Ic}}-1}\right)$. The curves $\psi = f(\frac{b}{b_0})$ for both elastic and elastic-plastic models are given in figure 4.15.

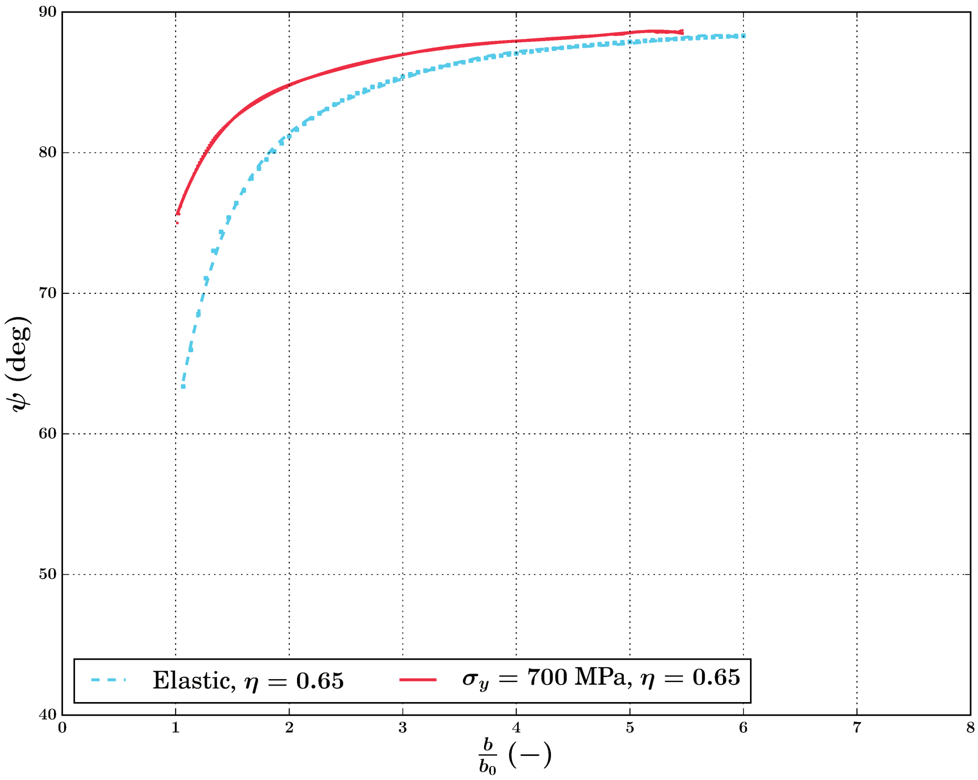

FIGURE 4.15: *Mode mixity angle ψ as a function of the normalized position of the crack front $\frac{b}{b_0}$, where b is the half width of the blister and b_0 the half width of the initial defect in the case of an elastic and an elastic-plastic response of the film.*

In both cases, the value of ψ increases during the propagation of the blister which means that the energy needed to break the interface increases during the propagation. However, we can notice that for a given advance of the crack front $\frac{b}{b_0}$, the value of mode mixity angle (at the crack front) is larger in the case of elastic-plastic behaviour compared to purely elastic case. This means that the plasticity of the film makes the interface harder to break, by modifying the mode mixity at the crack front. As the total available energy is the same in the elastic and the plastic case, the blister in the elastic-plastic case reaches the equilibrium states for a smaller delaminated area. However, it should be noted that when considering the fractured cohesive elements, the process zone seems to be more important in the elastic-plastic case (approximately 10%) compared to the elastic case (8%). The comparison of the energy dissipated at the interface between the elastic and the elastic-plastic case is thus not trivial. Nevertheless, it seems that the stabilization of elastic-plastic blisters at smaller width is related to the increase of the ratio of shear to normal stress at the interface (i.e mode mixity) compared to the elastic case, rather than dissipating by plastic deformation during crack propagation.

4.2.4 Could plasticity influence the onset of buckling-driven delamination?

We demonstrated in the former section how the elastic-plastic response of the film can influence the propagation and the final morphology of the blister. The results considered previously correspond to values of residual stresses (700 MPa) above the theoretical critical limit of buckling in the frame of elastic mechanics ($\sigma_c = 685$ MPa). However, as explained in chapter 2 the residual compressive stresses measured by DRX in the case of the sample α are approximately equal to 300 MPa which is significantly lower than the critical buckling stress calculated in the frame of elastic mechanics.

The aim of this section is to consider a case study with a thermal loading and an yield stress that are the closest possible to the experimental case presented in chapter 2. We will first carry out finite element simulations that account for a yield stress of 400 MPa (the value of yield stress measured by nano-indentation) and values of residual stresses between 300 and 420 MPa to study the effect of the ratio $\frac{\sigma_0}{\sigma_y}$ on the onset of buckling-driven delamination. Then we will study the combined effect of the cohesive parameters and plasticity on the shape of the blister at equilibrium.

Influence of the ratio $\frac{\sigma_0}{\sigma_y}$

In this paragraph, we consider a rectangular plate with an initial defect width $2b_0$ of $9\ \mu$m. The thin film has an elastic-plastic response governed by Ludwik hardening with an yield stress of 400 MPa. The film is subjected to compressive stresses with amplitude ranging from 300 to 420 MPa which is below the critical stress of the system if considered elastically ($\sigma_c = 685$) MPa. The parameters governing the response of the interface have been adapted to allow delamination. All the parameters used in this study are detailed in table 4.5.

Geometry		Elastic properties		Plasticity		
h (nm)	$2b_0$ (µm	E (GPa)	ν (-)	σ_y (MPa)	K (MPa)	n (-)
400	9	85	0.44	400	50	0.25

Interface				loading
G_{Ic} (J/m^2)	η (-)	T_t^i (MPa)	T_n^i (MPa)	σ_0 (MPa)
0.2	0.65	120	60	variable

TABLE 4.5: *Summary of the parameters' values used in the modelling of elastic-plastic buckling-driven delamination.*

We start our study by considering the response of the plate to compressive stresses equal to the experimentally measured compressive stresses $\sigma_0 = 300$ MPa. As shown in figure 4.16, this loading is not large enough to trigger the buckling of the film. Then we consider values of compressive stresses larger than the yield stress. We can notice in figure 4.16 that as the ratio $\frac{\sigma_0}{\sigma_y}$ increases, the maximum deflection of the blister also increases. The experimental maximum deflection is reached for a final stress $415 < \sigma_0 < 420$ MPa corresponding to a maximum plastic deformation of approximately 6% at the tip of the buckle and 3% in the unbuckled part of the film as shown in figure 4.17.

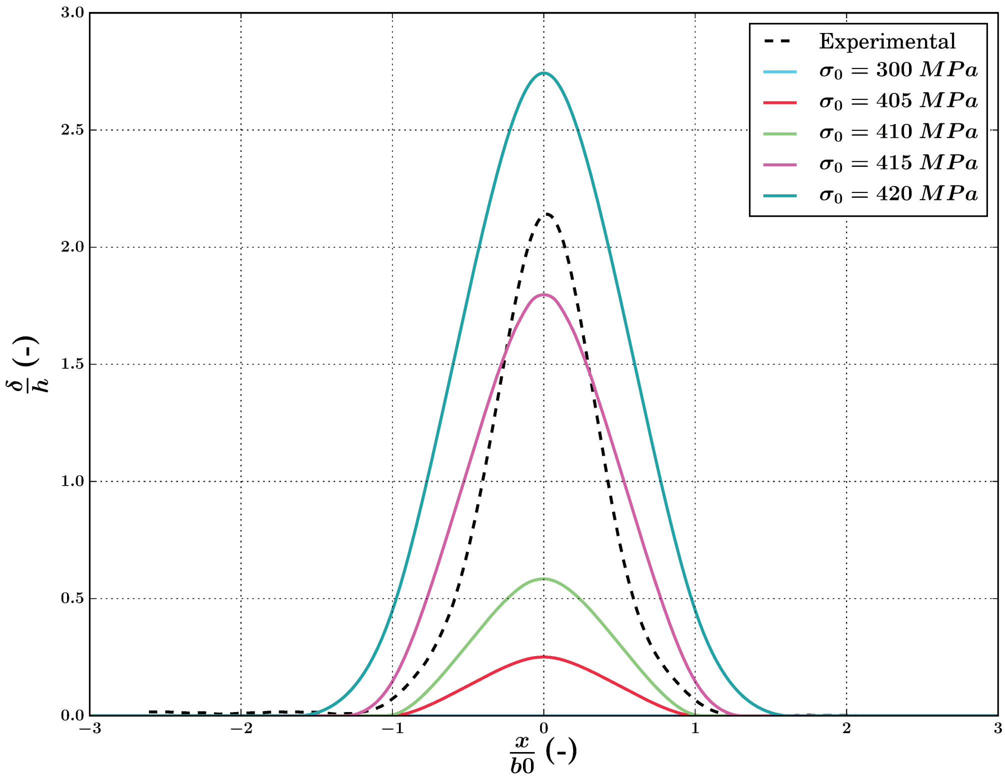

FIGURE 4.16: *Different straight blisters' profiles obtained for different values of compressive stresses for* $\sigma_y = 400$ MPa*. The parameters used are detailed in table* 4.4.

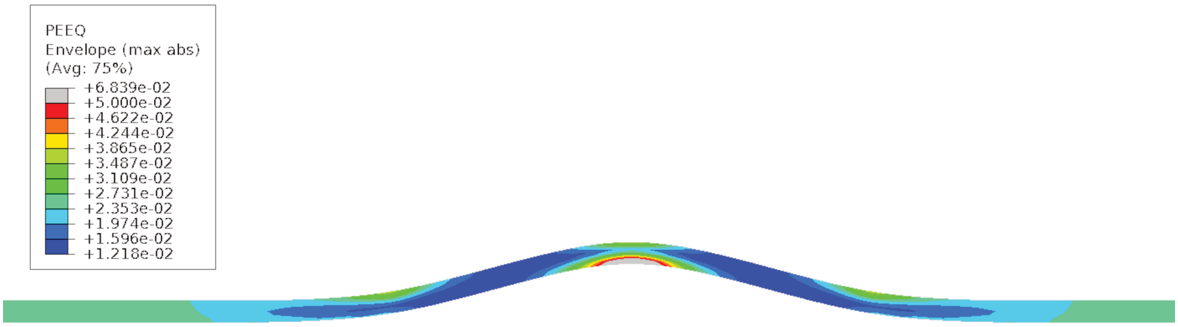

FIGURE 4.17: *Equivalent plastic deformation mapping in the cases* $\sigma_0 = 420$*. The remaining parameters are detailed in table* 4.5.

Another interesting point is that as $\frac{\sigma_0}{\sigma_y}$ increases, the profile of the blister seems to differ more from the sinusoidal shape of elastic blisters. However, varying only the ratio $\frac{\sigma_0}{\sigma_y}$ does not seem to be sufficient to capture the shape of the experimental blister. Indeed the base of the experimental blister seems to be particularly curved compared to the finite element solutions depicted in the same graph. This shape might make the reader think of the occurrence of delamination prior to width $2b_0 = 9\ \mu\mathrm{m}$ used as an initial defect in this paragraph. Thus, the aim in the next paragraph is to modify the width of the initial defect, test different interface configurations and compare the results to the shape of the blister obtained experimentally.

Influence of the cohesive parameters

In this paragraph, we choose to work with an initial defect width of $2b_0 = 6\ \mu\mathrm{m}$. We set the value of the final stress σ_0 to $415\ \mathrm{MPa}$ and chose to vary the values of maximum normal and shear stress which monitor the onset of damage. The remaining parameters are presented in table 4.5.

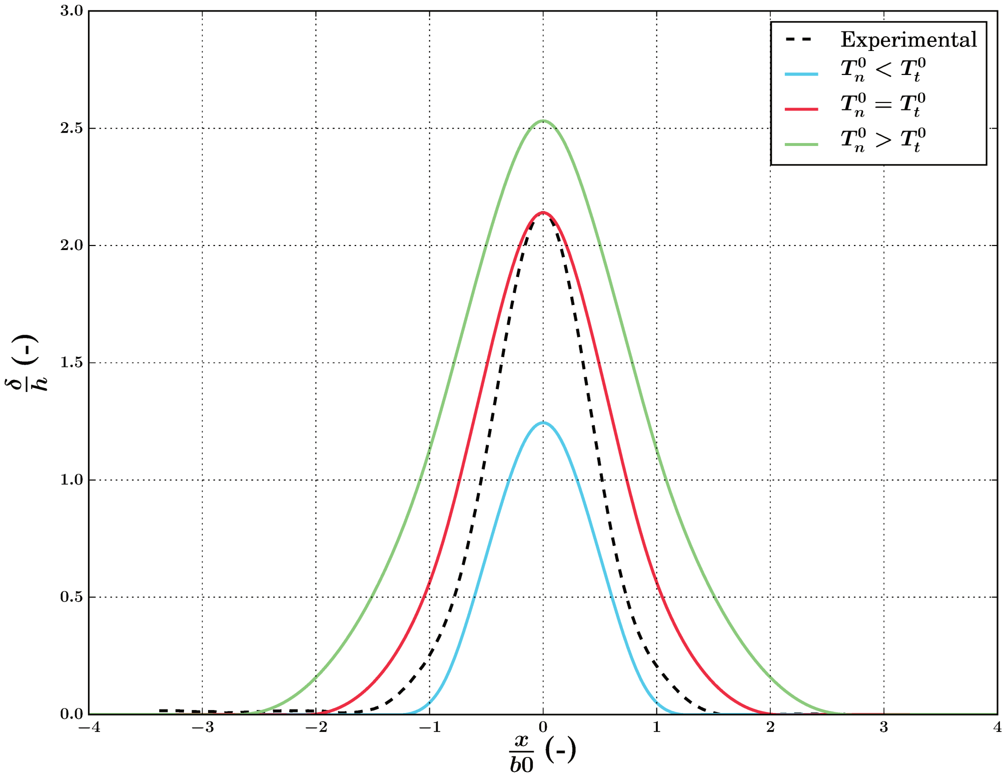

FIGURE 4.18: *Comparison between the profiles obtained for different values of maximum normal and shear stress T_n^0 and T_t^0. The cases $T_n^0 < T_t^0$, $T_n^0 = T_t^0$ and $T_n^0 > T_t^0$ correspond respectively to the following couples (T_n^0, T_t^0): $(60, 120)$, $(60, 60)$ and $(60, 40)$ MPa*

In figure 4.18, we present the profiles of straight blister obtained for the following couples (T_n^0,T_t^0): $(60, 120)$, $(60, 60)$ and $(60, 40)$ MPa where the value of T_n^0 is fixed at $60\ \mathrm{MPa}$ and the value of T_t^0 varies. We notice that as T_t^0 decreases, the maximum deflection increases. This increase in the maximum deflection is correlated to the increases of the ratio of the process zone to the final width of the blister b_f ($\frac{l_{PZ}}{b_f}$) which is consistent with the trend observed in the case of elastic buckling-driven delamination in section 4.2.1. The ratio $\frac{l_{PZ}}{b_f}$ increases from 2% in the case $T_n^0 < T_t^0$ to approximately 27% in the case $T_n^0 > T_t^0$. Although a value of 27% exceeds the order of magnitude of 10% typically used for $\dfrac{l_{PZ}}{b_f}$ to ensure consistency with numerical results obtained using cohesive zone model and the analytical predictions, the presence of an extended process zone is consistent with the apparent damage of the interface observed for values of $\frac{x}{b_0}$ lower than -2 (refer to figure 4.18). This non-planarity of the interface might be the sign of interface damage.

In order to visualize more clearly the effect of interface properties in the case of elastic-plastic buckling on the equilibrium shape of the blister, we re-scaled all the graphs of figure 4.18 and normalized their out-of-plane displacement and the $x-$values by the maximum deflection δ_{max} and the final blister's width b_f respectively. We also plotted a normalized curve corresponding to the sinusoidal shape of elastic analytical profiles. These curves are displayed in figure 4.19.

We can notice that the experimental curve as well as the elastic-plastic FEM solutions are more curved at their basis compared to the sinusoidal shape. The configuration that seems to fit the most the experimental case is obtained for $T_n^0 = T_t^0 = 60$ MPa. Thus, among the tested configurations, the latter seems to be the most adapted to model the buckling-driven delamination that lead to the buckling structure observed experimentally in sample α.

To conclude, in this section, we have pointed out the possibility of the onset of buckling in ductile thin films with values of final compressive stresses that are lower than the critical stress predicted by the elastic analytical model. This result might give us an interesting clue about the conditions that lead to the buckling of the film in sample α. However,experimental measurements showed the presence of residual compressive stresses that are lower than the yield stress. This issues leads to the importance of considering the full history of the loading when modelling the elastic-plastic response of thin films.

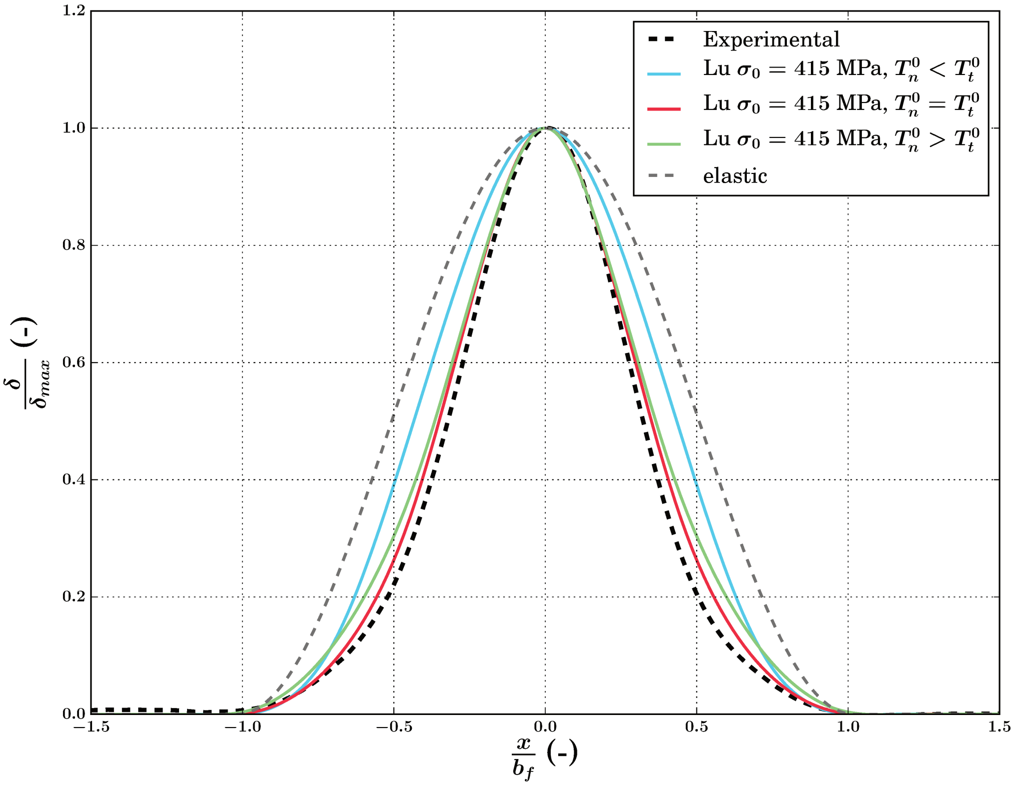

FIGURE 4.19: *Normalized out-of-plane displacement* $\frac{\delta}{\delta_{max}}$ *as a function of* $\frac{x}{b_f}$ *for* $\sigma_0 = 415$ MPa, $\sigma_y = 400$ MPa *and for different values of* (T_n^0, T_t^0)*:* $(60, 120)$, $(60, 60)$ *and* $(60, 40)$ MPa.

4.2.5 Influence of the loading history on the equilibrium profile of the blister

In order to test the assumption of non-monotonic intrinsic stress evolution, we propose a preliminary model which accounts for a non-monotonic stress variation during deposition. We propose thus to test two different loading histories: the former loading represented in figure 4.20 by an orange plain line, and a non-monotonic one plotted in blue. During the non-monotonic loading, the stress in the film first reaches linearly a maximum stress value σ_{max} which is slightly above the yield stress. Then, this stress is maintained allowing the blister to propagate and reach its equilibrium state. Finally, the stress decreases until reaching the final stress corresponding to the experimental measurement of residual stresses in the sample.

It is clear by considering the study presented above, that using a maximum stress σ_{max} lower than the experimental yield stress $\sigma_y = 400$ MPa is not sufficient to trigger buckling. Thus, σ_{max} should be larger than the yield stress and should be sufficient to exceed slightly the maximum deflection of the experimental profile in order obtain a final profile that is close enough to the experimental one after the unloading.

By considering the interfacial parameters introduced in the above section $T_n^0 = T_t^0 = 60$, and $G_{Ic} = 0.2\ \mathrm{J\,m^{-2}}$ as well as the corresponding profile, it is clear that σ_{max} should slightly

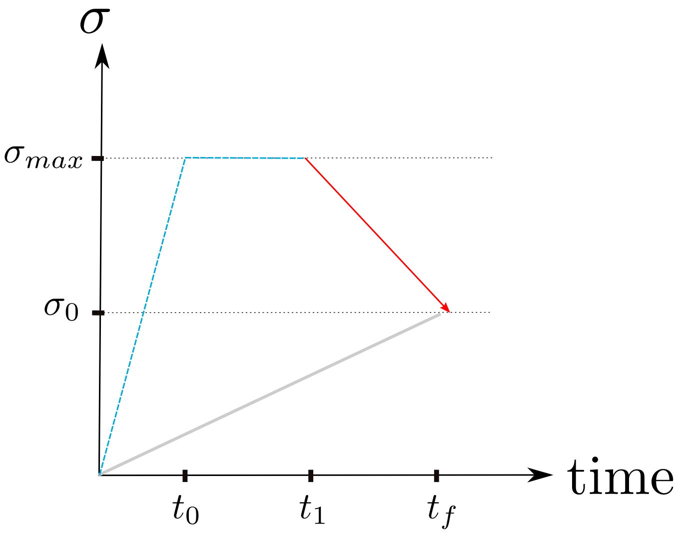

FIGURE 4.20: *Different loading histories: Linear loading (red) and tri-linear loading (blue)*

exceed the value 415 MPa to ensure that the unloading process does not cause the deflection to become lower than the experimental value . We chose to work with a value of maximum stress $\sigma_{max} = 418$ MPa. The corresponding predicted profiles are plotted in figure 4.21. The dotted blue curve corresponds to the profile of the straight blister at equilibrium for $\sigma = \sigma_{max}$ while the plain red curve corresponds to the profile of the blister at the end of the unloading process. The grey curve represents the profile of the unbuckled state obtained if a simple linear loading is performed to reach the final stress value σ_0.

We can notice that due to the high plastic deformation encountered by the film at $\sigma = \sigma_{max}$, the maximum deflection of the film does not vary drastically once the unloading applied. Moreover, the blister's profile obtained after the unloading process is close enough to the experimental shape of the blister.

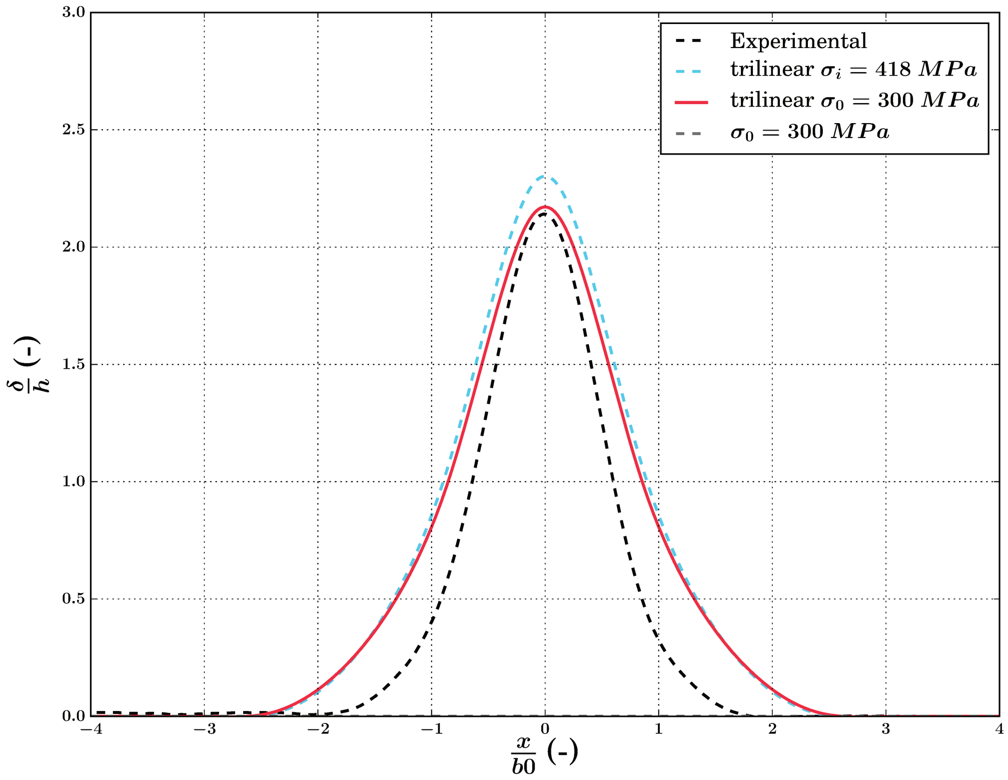

FIGURE 4.21: *Effect of non-monotonic loading on elastic-plastic buckling-driven delamination in the case of straight blister (Ludwik strain hardening $\sigma_y = 400$ MPa, $K = 50$ MPa, $n = 0.25$)*

When compared with the final profile obtained using similar process in pure buckling (see section 3.3.2), we can notice that introducing a cohesive behaviour of the interface helped in minimizing the difference in shape between the modelling results and the experimental observations in the case of straight blister.

4.2.6 Influence of the boundary conditions on the elastic-plastic buckling-driven delamination

At the beginning of the chapter, when presenting the numerical model in section 4.1.2, we pointed out the importance of implementing the thermal loading of the system at a sufficiently high rate to ensure that the buckling-driven delamination process occurs at a constant stress while avoiding dynamic effects. Using this method, we had little buckling during the loading step and achieved most of the delamination during the 2^{nd} step. In the case of the experimentally studied samples, it seems that the buckling of the thin film occurred after the deposition process once the internal stresses in the film have reached their final value [6, 18].

In order to prevent the film's buckling during the "loading", we set to zero the displacement component of the bottom nodes of the defect area of the film along the $z-axis$. Once the loading completed, these boundary conditions are released and a small pressure less

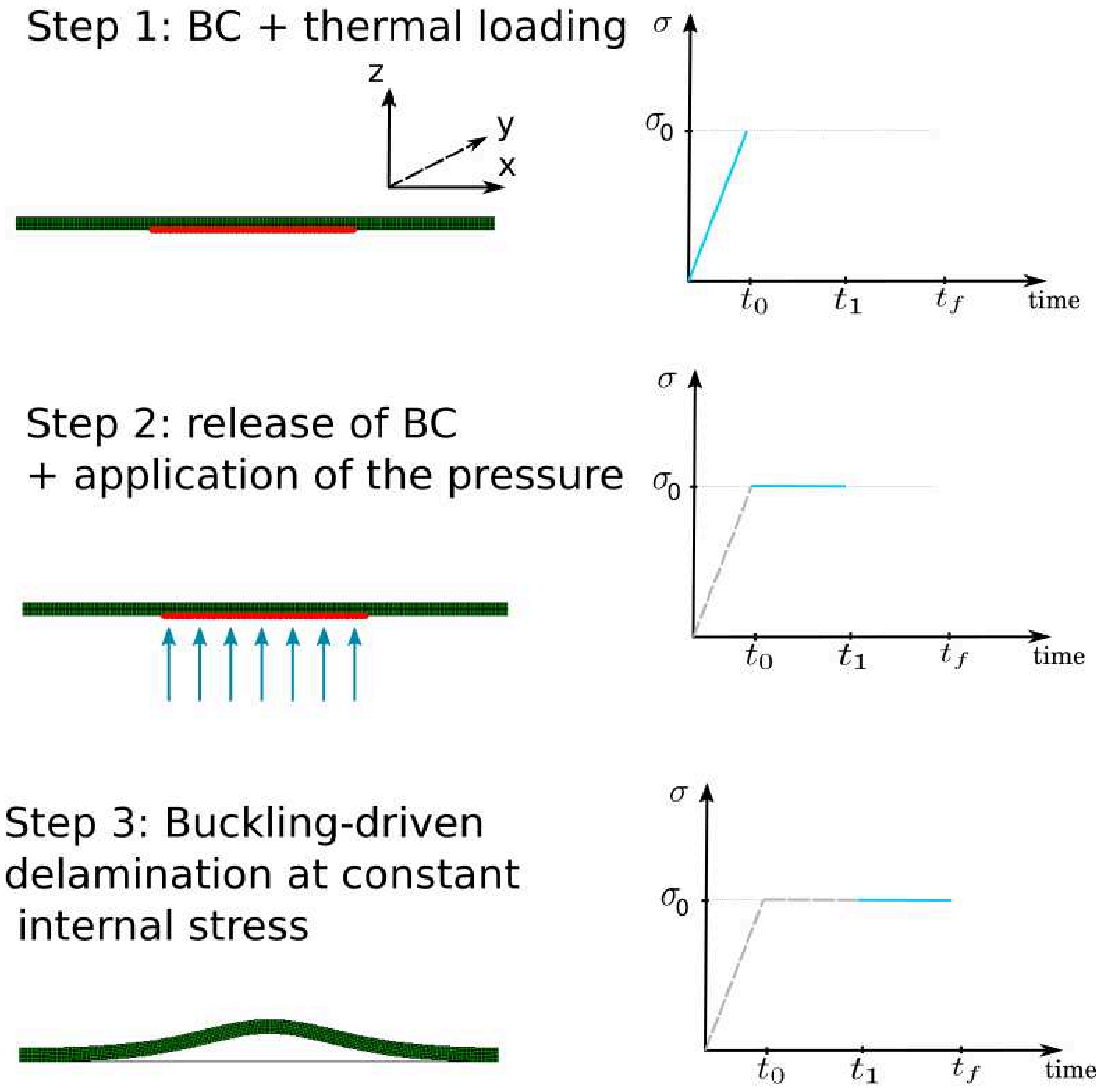

FIGURE 4.22: *Scheme of the steps applied to ensure the occurrence of buckling-driven delamination at constant load* σ_0*. In the first step, the bottom nodes of the defect area of the film are blocked along the* $z - axis$ *and the thermal loading of the film is performed. In the* 2^{nd} *step, the defect nodes are released and a small pressure is applied ton trigger buckling. In the final step, buckling-driven delamination occurs at constant loading.*

then 1% of the residual stress of the film is applied at the bottom of the free part of the film along the $z - axis$ to trigger buckling. During the last step, we can thus observe the buckling-driven delamination of the thin film occurring at constant internal stress. This method is presented schematically in figure 4.22.

To test this method and determine if there is any significant difference between the two loading strategies, we carried out two simulations with the parameters given in table 4.4, $\sigma_0 = 700\ \mathrm{MPa}$ and different loading methods. We compared these results in terms of equilibrium profiles and equivalent plastic distribution presented in figures 4.23 and 4.24 respectively. The profiles shown in figure 4.23 are very similar. They both exhibit a sharp tip

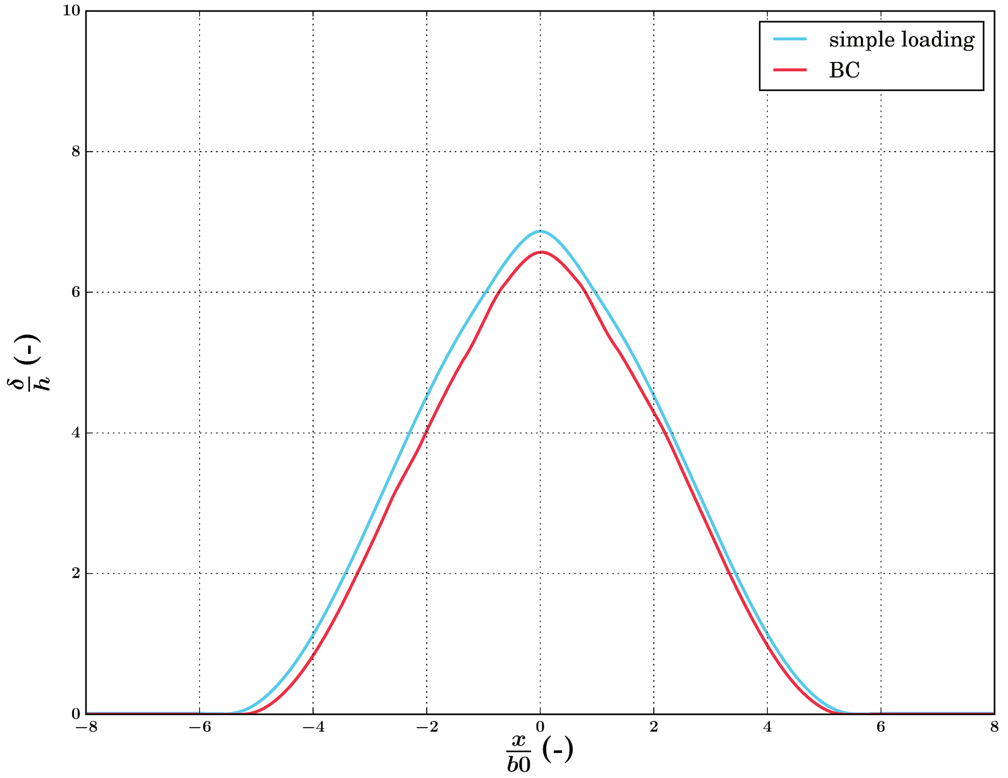

FIGURE 4.23: *Comparison of the equilibrium profiles obtained using the two different loading types presented in this section. 'BC' corresponds to the results obtained by blocking the displacement of the nodes at the bottom of the defect area during the loading. 'Simple loading' correspond to the results obtained without implementing particular displacement restrictions during the loading.*

compared to the sinusoidal shape of elastic solutions. However, there is a small difference in the maximum deflection. This difference might originate from the small out-of-plane displacement that triggers the buckling in the case of simple loading. Finally, in both cases the maximum plastic deformation is of approximately 2% and the distribution of the plastic deformation is also very similar.

To summarize, introducing boundary conditions to prevent the onset of buckling-driven delamination during the thermal loading of the film does not seem to result in significantly different buckling profiles or plastic deformation levels for $\sigma_0 \leq \sigma_y$. This similarity reinforces the validity and accuracy of the results presented in this chapter concerning the buckling-driven delamination of thin films.

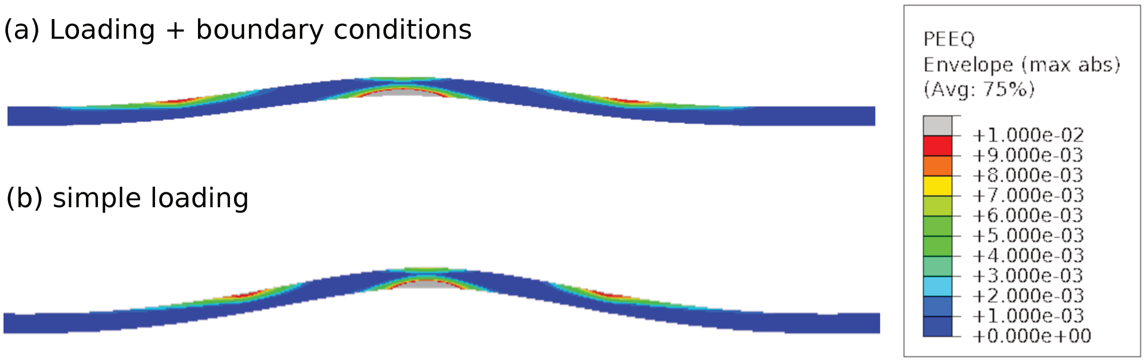

FIGURE 4.24: *Mapping of equivalent plastic deformation. (a) Results obtained by blocking the displacement of the nodes at the bottom of the defect area during the loading. (b) Results obtained using simple loading with no restrictions on the displacement of certain parts of the film.*

4.3 Growth and destabilization of circular blisters

The aim of this part is to study the mechanism of growth and destabilization of circular blisters and understand how the plasticity of the film can influence the equilibrium state. To do so, a finite element model that takes into account the non-linearity of the film and the delamination at the the interface has been elaborated. First, the mechanism of growth and destabilization of circular blisters is considered in the case of a purely elastic thin films and in particular, the influence of interfacial mode mixity η on the equilibrium state is studied. These modelling results are then compared with the analytical results presented in 1.3.2 to assess the accuracy of the model. Finally, the influence of the plasticity of the film on the stability of circular blisters is studied and the results are discussed in the light of elastic predictions.

4.3.1 Presentation of the model and the parameters

In the frame of this study, we adapt the model used to study the propagation of straight blisters to fit the circular case. In particular, we implement a circular defect area (deprived of adhesion) with a squared plate to allow an axisymmetric growth of the blister. The width of the defect and the thickness of the plate are set according to the experimental case study γ ($2b_0 = 50$ µm and $h = 630\ nm$). We use the same elastic properties E and ν as in part 4.2 and choose a relatively moderate adhesion $G_{Ic} = 0.5\ \mathrm{J/m^2}$ to allow for the delamination of the film at values of compressive stresses close to the measured residual stresses (500 MPa). As highlighted in section 4.2.1, this value of mode I interfacial toughness is consistent with values of work of adhesion of metal thin films on silicon substrate which are in the range of 0.2 to 5 $\mathrm{J/m^2}$ [38, 109]. High values of mode mixity dependence (typically $\eta = 0.9$) are used in order to perform a meaningful comparison with the analytical study performed using η close to 1 [49]. Finally values of maximum normal and shear tractions T_n^0 and T_t^0 are set to allow for a maximum process zone of 10% of the width of the blister. These parameters are summarized in table 4.6.

Elastic properties		Geometry		Interface			
E (GPa)	ν (-)	h (nm)	$2b_0$ (µm)	G_{Ic} (J/m^2)	η (-)	T_n^i (MPa)	T_t^i (MPa)
85	0.44	630	50	0.5	0.9	40	180

TABLE 4.6: *Parameters used for the elastic buckling-driven delamination of circular blisters. Gold thin film elastic properties (E: Young's modulus, ν: Poisson's ratio), blisters geometries (h: thin film's thickness, $2b$: blister's radius) and interface parameters (G_{Ic}: interfacial toughness, η: mode mixity dependence, T_n^i: maximum normal traction, T_t^i: maximum shear traction)*

The thermal loading is performed so that the propagation of the blister and its destabilization occur at constant compressive stress σ_0.

4.3.2 Elastic destabilization of circular blisters

In this section, we start by presenting and discussing an example of growth and destabilization of a circular blister obtained by mean of finite element modelling. The results are obtained using a value of final compressive stresses of 800 MPa. The evolution of the blister is shown in Fig. 4.25. The row (a) features the evolution of the out-of-plane displacement and the row (b) shows the corresponding degradation of the interface.

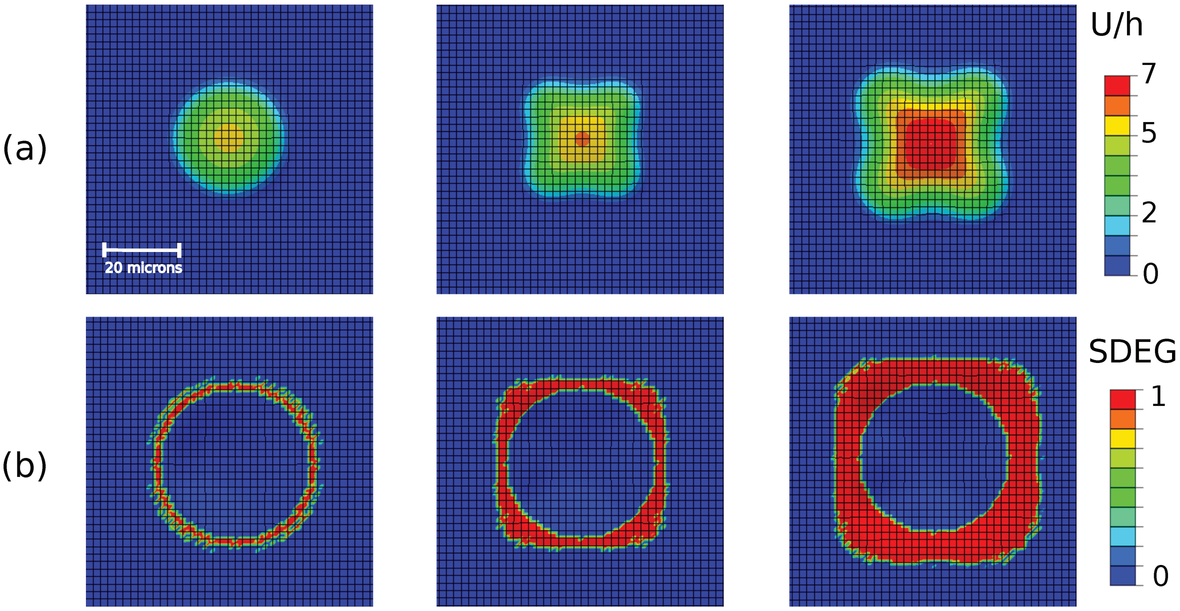

FIGURE 4.25: *Various stages of growth of a circular defect submitted to constant loading σ_0. The row (a) features the evolution of the normalized out-of-plane displacement $\frac{U}{h}$ and the row (b) shows the corresponding degradation variable of the interface SGEG. SDEG=0 means that the interface is intact, SDEG=1 means that the fracture is completed and intermediate SDEG values corresponding to an ongoing fracture process.*

In the first stage of growth, the blister remains circular. Then, the circular front destabilizes and the blister evolves into a non-axisymmetric morphology featuring 4 lobes. The moment at which the blister starts destabilizing is not erratic and is related to the ratio $\frac{\sigma_0}{\sigma_c}$. Indeed, in our case delamination occurs at a constant value of stress σ_0. However, as the blister expands, the blister's radius increases and the value of critical stress σ_c decreases according to equation 1.22. Thus the quantity $\frac{\sigma_0}{\sigma_c}$ increases during the propagation of the blister and the destabilization occurs for a given value of $(\dfrac{\sigma_0}{\sigma_c})_{destab}$. It is the couple $((\dfrac{\sigma_0}{\sigma_c})_{destab}, n)$ where n is the number of lobes that is reported in the destabilization diagram presented in the chapter 1, figure 1.18. For example, in the case presented above, $(\dfrac{\sigma_0}{\sigma_c})_{destab}$ has been measured at the increment just prior to the destabilization and is approximately equal to 21.

Comparison between the numerical and analytical results

To properly compare analytical predictions with numerical results, we iterate the previous process using different stress values ranging from 200 MPa to 1.5 GPa and plot a data point

$((\dfrac{\sigma_0}{\sigma_c})_{destab}\ , n)$ per simulation in figure 4.26. Our results are plotted along with the analytical results to make the comparison easier.

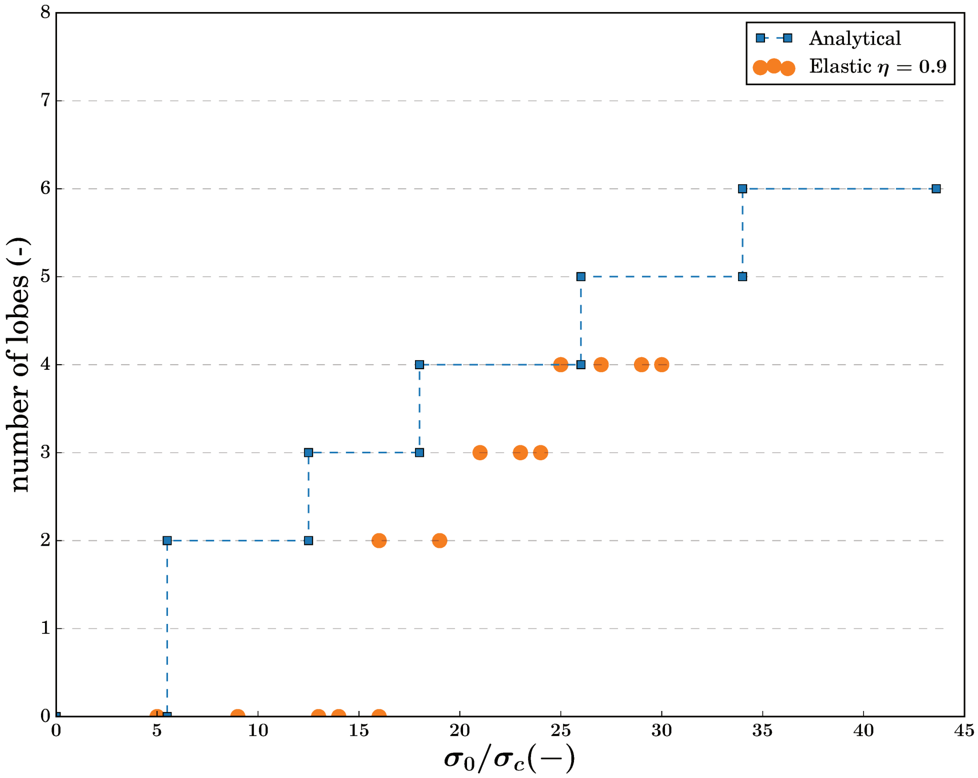

FIGURE 4.26: *Number of lobes n resulting from the destabilization process of an initially circular blister at different loading ratios* $\frac{\sigma_0}{\sigma_c}$. *Numerical results are obtained using cohesive zone model for a mode mixity dependence parameter* $\eta = 0.9$ *and Poisson's ratio of the film* $\nu = 0.44$. *The analytical results are obtained for* $\eta = 1$ *and* $\nu = \dfrac{1}{3}$.

We observe that the number of lobes created upon destabilization is consistent with the analytical trend and increases gradually with $\frac{\sigma_0}{\sigma_c}$. However, we observe a small shift between the numerical and analytical results. The same number of lobes n is formed at a larger loading ratio compared to analytical results, especially for small number of lobes. By measuring the corresponding process zone to blister's width ratio for each number of lobes at the destabilization of the blister $(\dfrac{l_{PZ}}{2b_0})_{destab}$, we notice that it reaches its highest value for $n = 0$ (around 9%) and decreases as n increases reaching 5% for $n = 4$. The extent of the process zone might then cause the stabilization of a certain configuration for larger $\frac{\sigma_0}{\sigma_c}$ values. Another aspect that might contribute to this shift is related to the determination of the ratio $\frac{\sigma_0}{\sigma_c}$. Indeed, for each simulation, we determine visually the first frame at which the destabilization process starts and sometimes it can be quite difficult to figure out exactly at which frame the destabilization starts. To assess the error related to the measurement method, we calculate for each simulation the ratio $\frac{\sigma_0}{\sigma_c}$ at three consecutive frames near the destabilization point. The difference was found to be at maximum 4% between consecutive frames. The values presented in figure 4.26 are the mean values for each simulation. It should be noted that a similar study was performed by Faou et al. in [53] and shows similar results obtained for $\eta = 0.95$ and $\nu = 0.31$.

Influence of mode mixity dependence

In the literature, the question of the stability of circular blisters is only addressed for high values of mode mixity dependence including $\eta = 1$ and $\eta = 0.95$ for elastic thin films on rigid substrates. The aim of this section is to question the effect of mode mixity dependence parameter η on the stability of blisters. To this end, various simulations are performed using the parameters detailed in table 4.6 by varying η from 0.6 to 0.9. The corresponding data points as well as the analytical results for $\eta = 1.$ are plotted in figure 4.27.

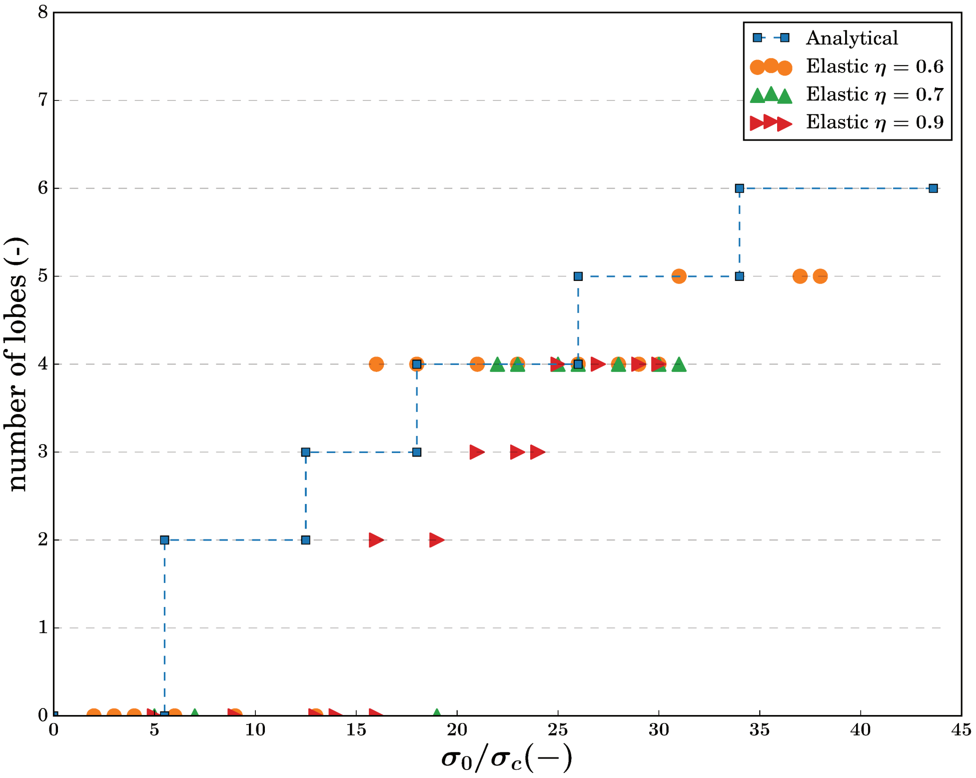

FIGURE 4.27: *Number of lobes n resulting from the destabilization process of an initially circular blister at different loading ratios* $\frac{\sigma_0}{\sigma_c}$. *Numerical results are obtained using cohesive zone model for a mode mixity dependence parameters of* 0.9, 0.7 *and* 0.6 *and Poisson's ratio of the film* $\nu = 0.44$. *The analytical results are obtained for* $\eta = 1$ *and* $\nu = \frac{1}{3}$.

We can notice that in the frame of our finite element modelling a destabilization into 2 and 3 lobes could not be obtained for low values of η including 0.6 and 0.7 In particular low values of η seem to stabilize circular blister and only favour the destabilization into 4 lobes. We think that the destabilization of the blister becomes less energetically favourable at low mode mixity dependence because it is a lot easier to break the interface at high mode mixity angles. To confirm this hypothesis further investigation concerning the mode mixity distribution and energy balance should be conducted.

4.3.3 Influence of plasticity on the destabilization of circular blisters

The aim of this section is to study the effect of plasticity on the destabilization of circular blisters. To this end, we implemented an elastic-plastic behaviour into our simulations consisting of a Ludwik law with the following parameters $\sigma_y = 800\,\mathrm{MPa}$,$K = 50\,\mathrm{MPa}$, $n = 0.25$. We chose first to compare an elastic and an elastic-plastic case for which the elastic and interfacial properties as well the geometries of the problem are identical. Only the elastic-plastic behaviour differs. We chose to work with the parameters that allowed the destabilization of an elastic circular blister into three lobes for $\frac{\sigma_0}{\sigma_c} = 24$ for $\eta = 0.9$ (see figure 4.26). This result is obtained for $\sigma_0 = 750\,\mathrm{MPa}$. The remaining parameters are summarized in table 4.6.

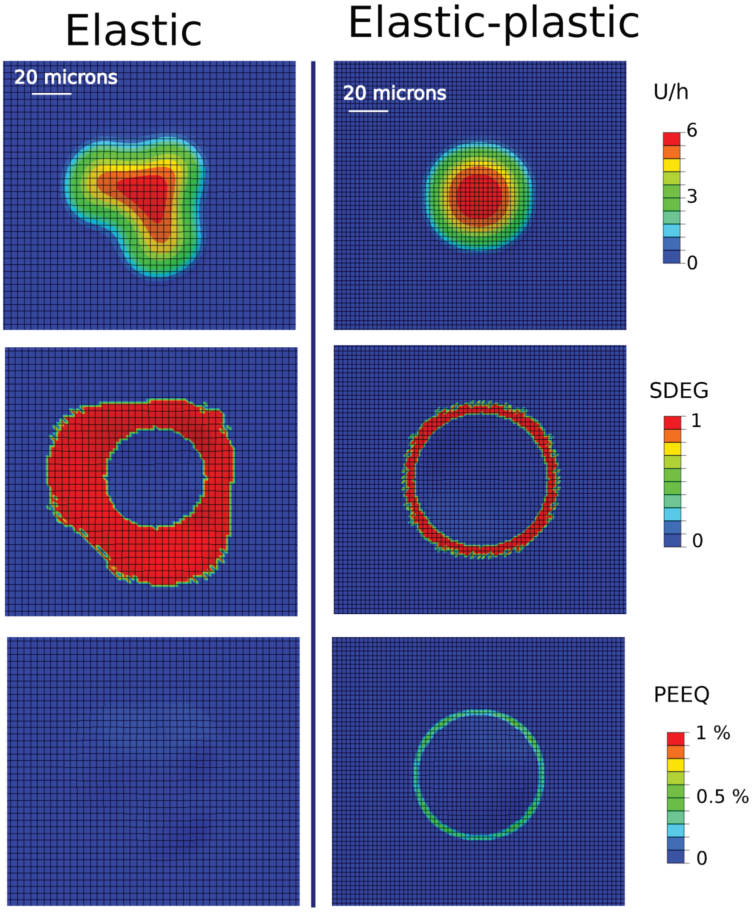

FIGURE 4.28: *Various stages of growth of a circular blister submitted to constant load σ_0 in the case of an elastic and an elastic-plastic behaviour ($\sigma_y = 800\,\mathrm{MPa}$,$K = 50\,\mathrm{MPa}$, $n = 0.25$). Each case features the mapping of the normalized out-of-plane displacement $\frac{U}{h}$ at the equilibrium point, the corresponding degradation variable of the interface SGEG and the distribution of the plastic deformation.*

The corresponding results are presented in figure 4.28. We can notice that the plastic deformation occurs locally and forms a ring around the blister at the region where the delamination took place. The presence of plastic dissipation around then blister might locally increase the mode mixity angle around the blister making it more difficult to fracture the interface as demonstrated in section 4.2.3. Further investigations of the energy balance and mode mixity are also needed here to confirm this hypothesis.

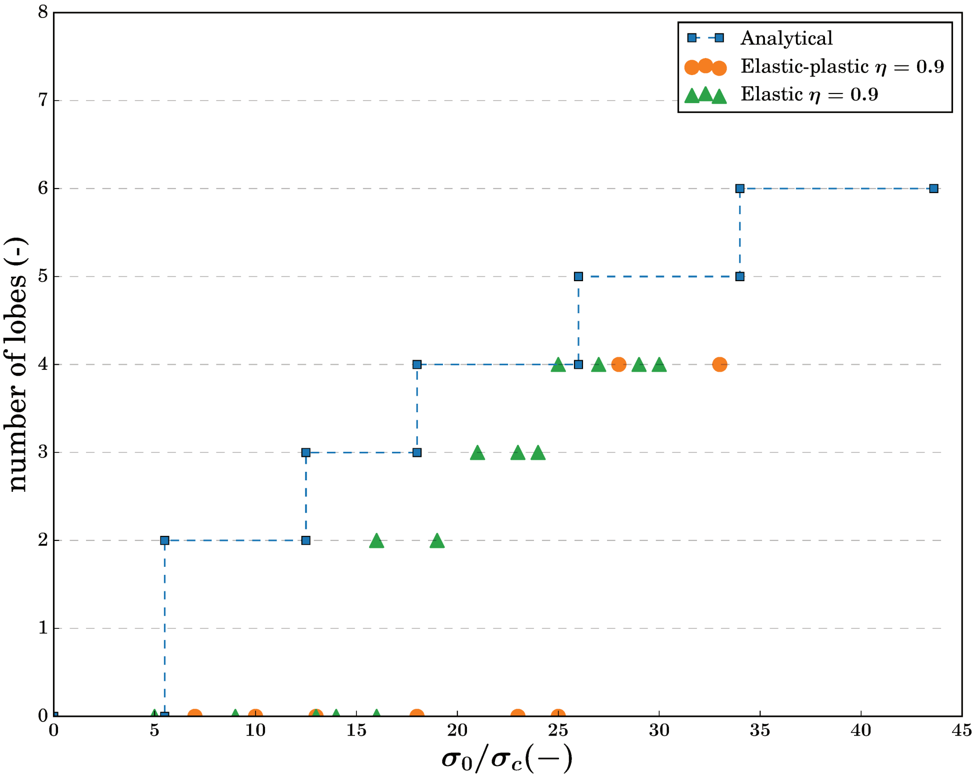

FIGURE 4.29: *Number of lobes n resulting from the destabilization process of an initially circular blister at different loading ratios* $\frac{\sigma_0}{\sigma_c}$ *for an elastic and an elastic-plastic thin film. Numerical results are obtained using cohesive zone model for a mode mixity dependence parameters of* 0.9 *and Poisson's ratio of the film* $\nu = 0.44$. *The analytical results are obtained for* $\eta = 1$ *and* $\nu = \frac{1}{3}$.

To understand to what extent plasticity modifies the destabilization process of circular blisters, we perform various elastic-plastic simulations and compare the results with those of the elastic model which serves as a reference. It should be mentioned that due to the presence of an elastic-plastic behaviour, varying the thermal load to obtain different $(\frac{\sigma_0}{\sigma_c}, n)$ with a fixed plastic law will lead to different levels of plastic deformation among the different simulations and the effect of plasticity would not be similar for the different results. To avoid this problem, we chose to maintain a fixed internal stress and elastic-plastic behaviour for all simulations and only vary the size of the initial defect which causes a variation of $\frac{\sigma_0}{\sigma_c}$. We first tested this method in the elastic case (at least the two extreme values for each single number of lobes), and the results showed to be very similar to the previous ones. Then, we implemented this method it in the case of an elastic-plastic behaviour of the film. The results are presented in figure 4.29.

According to the results presented in figure 4.29, the elastic-plastic behaviour of the film seems to either stabilize circular shapes or favour the destabilization into 4 lobes for very high values of the stress. We could not observe the destabilization into 2 or 3 lobes in the case of elastic-plastic thin films. This result is very interesting and might explain why we could not so far observe a destabilized blister in the case of gold thin film experimentally. Given the elastic properties and the thickness of the gold thin film as well as the geometry of the defect area in the experimental case γ, we will need residual compressive stresses to observe destabilized blisters. With a value of residual stresses of 500 MPa, the experimental case present a loading ratio $\frac{\sigma_0}{\sigma_c} = 8$ and lies then in the area where the circular blister is stable.

4.4 Conclusion

In this chapter, we focused on understanding how coupling an elastic-plastic response of the film with the delamination of the interface can influence the final morphology of the blister. The results were presented under two main sections: buckling-driven delamination of straight blisters and the growth and destabilization of circular blisters.

Straight blister In the study of the buckling-driven delamination of thins film, we started by studying a purely elastic case. In particular, we studied the influence of the different parameters that govern the delamination of the interface and highlighted the importance of mode mixity in the stabilization of the blister. Then we explained how the elastic-plastic model has been implemented and we the different difficulties encountered when trying to carry out buckling-driven delamination simulations using $3D$ elements with an implicit and explicit approach.

The first simulation results were presented in section 4.2.3 and aimed at studying the influence of the ratio $\frac{\sigma_0}{\sigma_y}$ on the propagation and the morphology of the blister. It has been evidenced that as the ratio $\frac{\sigma_0}{\sigma_y}$ increases, the levels of plastic deformation in the plate increase causing the blister to form a sharp tip compared to the sinusoidal shape of elastic blisters. Moreover, the development of plasticity at the interface during the propagation of the blister seems to stabilize it and limit its final width compared to the corresponding elastic case. This trend seems to be caused by the modification of the shear to normal stress ratio at the interface rather than by a decrease in the dissipated energy at the interface. The results presented so far represent rather a theoretical study of the effects of the plasticity on the equilibrium state of straight blisters.

The experimental case of the straight blister observed in sample α has been more closely examined in part 4.2.4 and it has been demonstrated that it is possible to cause the buckling-driven delamination of ductile thin films when a ratio $\frac{\sigma_0}{\sigma_y} > 1$ is considered. Subsequently, we combined this approach with a non-monotonous loading that goes through three stages: a linear loading of the film until a value of σ_{max} larger that the yield stress is reached, a maintain at σ_{max} until the blister reaches its equilibrium profile and finally the unloading of the film to a target value σ_0 that is lower then the initial yield stress σ_y and equal to the values of residual stress measured experimentally. This approach proved to be efficient in generating buckles at final residual stresses lower than the initial yield stress of the film and the critical buckling stress calculated in the frame of elastic mechanics. It also provides us with a plausible scenario about the causes of the appearance on buckling structures in a ductile thin film with such low compressive residual stresses.

We closed the discussion about elastic-plastic buckling of thin films by considering an alternative way of stress loading that uses boundary conditions to prevent the onset of buckling-driven delamination from happening before the desired stress σ_0 is reached. This method is thought to better mimic the onset of buckling in experimental cases which seem generally to take place once the deposition process is completed and the final residual stresses in the film reached. The results obtained using this method seem to be consistent with those obtained using the former loading which validates our approach.

Circular blister In the study of the growth and destabilization of circular blisters, we started by considering the growth and destabilizations of blisters in a purely elastic thin films and we considered the evolution of the number of destabilized lobes at equilibrium as function of the loading ratio. It has been observed that the same number of lobes n is formed at a larger loading ratio compared to analytical results which is consistent with ref. [53] and is thought to be due to the influence of the process zone and its extent. Our contribution in the study of growth and destabilization of circular blisters in the frame of elastic mechanics comes from the study of the influence of mode mixity dependence parameter η. Indeed we demonstrated that using lower values of η for instance 0.6 and 0.7 resulted in the stabilization of the circular shape compared to the case $\eta = 0.9$. However, to have a better understanding of the mechanism of such stabilization, further investigation concerning the mode mixity distribution and energy balance should be conducted.

The last part of this study is dedicated to the investigation of the effect of plastic deformation of the film on the destabilization of the blister. By implementing an elastic-plastic behaviour in the case of circular blisters growth and destabilization, we could demonstrate that plastic dissipation helps stabilize the circular shape of the blister. The mechanism of stabilization of circular blisters in ductile thin film is however not totally clarified. Plastic dissipation is thought to influence mode mixity which leads to a stabilization. Nevertheless this hypothesis needs to be confirmed via a study of the evolution of mode mixity during the growth of the circular blister.

General conclusion and outlook

Conclusion

In this study, we have developed a $3D$ mechanical model to study the buckling delamination of ductile thin films on rigid substrates. The model has been implemented under the finite element code ABAQUS and takes into account isotropic plasticity, geometrically non-linearity contact with on a rigid substrate. Delamination of the film from the substrate is also taken into account by a a mode mixity dependent cohesive zone model. The main parameters used in this the model to describe the geometry of the film, its elastic-plastic behaviour and the value of residual stresses were measured experimentally on a gold thin film of $400\,\mathrm{nm}$ thick, deposited by sputtering on a $Si(100)$ substrate. The profiles of the buckling patterns have been characterized using atomic force microscopy and it has been evidenced that these profiles cannot be simply explained in the framework of linear elasticity. In particular, the straight blister present an unusually elongated shape with a curved basis, while the circular blisters showed a strong bending of the film at the delamination front. The internal stresses have been determined by the X-ray diffraction method to be around a few hundreds MPa, typically $300\ \mathrm{MPa}$ in compression in the case of the straight blister. Finally, the elastic-plastic response of the thin film has been studied using the nano-indentation technique. In particular, the Young's modulus of the film is shown to be around $85\,\mathrm{GPa}$ and and its yield stress around $400\,\mathrm{MPa}$. The film showed little hardening and we chose to model its elastic-plastic behaviour using a Ludwik law with a small hardening coefficient (approximately $50\,\mathrm{MPa}$).

One remarkable observation from this experimental study was the obvious possibility of triggering the buckling of ductile thin films with residual stresses that are lower than the theoretical critical buckling stress predicted for a purely elastic film. Indeed, in the case of the straight blister, the residual stress $\sigma_f = 300\ \mathrm{MPa}$ is lower than the critical stress calculated using the geometric and elastic properties of the film $\sigma_c \simeq 550\ \mathrm{MPa}$. One aim of the numerical study was thus to study the influence of plasticity on the morphology of straight and circular blisters. Another objective was to understand another remarkable observation concerning circular gold blisters on silicon substrates. Those observations are suggesting that this circular shape can be stable, whereas theoretical derivations in the framework of pure elasticity showed that it should not.

In chapter 3, we focused on the study of buckling of ductile thins films without delamination and discussed the influence of plasticity on the buckling mechanism. We have first studied the influence of the ratio $\frac{\sigma_f}{\sigma_y}$ on the buckling of thin film subjected to monotonic loading. We have evidenced that the elastic-plastic behaviour of the film causes higher deflections of the blister compared to the elastic case. In particular, the deflection of the blister is an increasing function of $\frac{\sigma_f}{\sigma_y}$. This behaviour is due to the increase in the plastic deformation levels and their concentration at the base of the blister with increasing values of $\frac{\sigma_f}{\sigma_y}$. Another interesting observation is that for $\frac{\sigma_f}{\sigma_y} > 1$, we could cause the buckling of the film even if the value of residual stresses σ_f are lower than the critical buckling stress derived for a purely elastic film. However, even for high values of $\frac{\sigma_f}{\sigma_y}$ and a finely meshed plate, the generic sinusoidal shape of the blister seems to be maintained.

Then, we have focused on the experimental cases and demonstrated that the use of monotonic loading with the experimental values of residual and yield stresses seems to be sufficient to form circular buckles with profiles that are (under certain conditions) sufficiently close to the the experimental case in terms of deflection and shape. However, in the case of the straight blister, the use of monotonic loading is not even enough to trigger the buckling of the film.

In order to solve this issue, we proposed a model that takes into account the evolution of stress during the deposition of thin films by using non-monotonic loading. During the non-monotonic loading, the stress in the film first reaches linearly a maximum stress value σ_{max} which is slightly above the initial yield stress before decreasing until the final stress corresponding to the measurement of the final curvature. This method aims at triggering the buckling of the straight blister (because σ_f is higher than σ_c). During the unloading of the film, the plastic deformation of the film helps maintain the structure of the blister which allowed as to generate buckling structures that have a similar maximum deflection to the experimental case.

The only issue that remained unsolved using an elastic-plastic buckling model is the elongated shape of the observed straight blister. Indeed, the addition of plasticity to the buckling problem does not seem to alter the sinusoidal shape of the blister. In order to solve this problem, we decided to account for delamination in the buckling model and study the influence of the interface along with the elastic-plastic behaviour of the film on the equilibrium shape of the blister which is presented in chapter 4.

The addition of cohesive zone behaviour proved to be a key ingredient in modifying the sinusoidal shape of the blister. Indeed by setting the appropriate cohesive parameters that allow for the onset and the propagation of interfacial damage and choosing values of applied stresses that are higher than the yield stress, we achieved elongated straight blisters with shapes that are comparable to the experimentally observed profile. The mechanism leading to the formation of such shapes as well as the influence of plasticity on the interfacial damage response have been studied thoroughly. In particular, we have demonstrated that the elastic-plastic response of thin films causes higher mode mixity values a the crack front, making it more difficult to delaminate than elastic film under the same loading conditions.

In the last part of this thesis, we have studied the influence of the mode mixity dependence parameter and the plasticity on the growth and destabilization of circular blisters. In particular, we have demonstrated that plasticity helps stabilize the circular shape during its growth. This result is important and might explain why we could not so far observe a non-axisymmetric structures in ductile thin film. This work should be completed by the study of the evolution of mode mixity during the propagation of circular blister in the case of elastic-plastic thin films and compare it to the elastic case in order to clarify the mechanism behind the stabilization of circular shapes.

Outlook

Coupling of Finite Element Modelling and Discrete Dislocation Dynamic

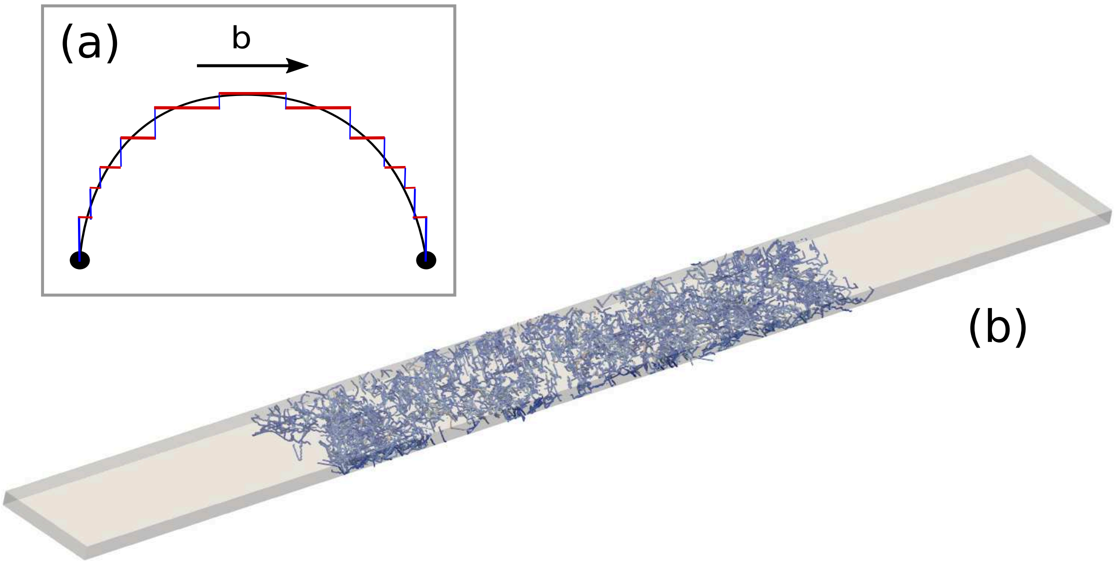

FIGURE 4.30: *(a) Edge-screw discretization of a dislocation line. Blue lines are edge dislocations and red lines are screw dislocations. (b) Coupling finite element method with discrete dislocation dynamics. The Frank–Read sources are distributed randomly in a rectangular single crystal that represents the thin film. Different colours represent different slip systems.*

In the case of thin films undergoing plastic deformations, size effects are often observed. One way of taking this phenomenon into account while staying in a continuum framework is to use strain gradient plasticity models. One another way is to use a coupled approach between finite element method and discrete dislocation dynamics (DDD). During this thesis, we started a collaboration with Dr. M. Fivel in order to model the buckling of ductile thin films using the coupling between discrete dislocation dynamics simulation and finite element method. This method provides a complementary approach to the finite element model discussed in the chapters 3 and 4 in which a macroscopic plastic law is implemented. The model is implemented using the code Cast3m as the finite element solver and TRIDIS for dislocation dynamics. TRIDIS is an edge-screw $3D$ Discrete Dislocation Dynamics code developed at SIMaP Laboratory by M.Fivel and M. Verdier [107]. The concept of 3D dislocation dynamics method has been imagined by L. Kubin, Y. Bréchet and G. Canova in the early 1990s [20, 62]. In such model, the dislocation lines are discretized into sets of edge and screw dislocations segments embedded in a continuum medium as shown in figure 4.30(a) and each of the segments generates a long range elastic stress field within the simulated body.

In the case of our model, a fixed number of Frank–Read sources are distributed randomly in a rectangular single crystal that represents the thin film at the beginning of the simulation. The geometry and a random distribution of Frank-read sources is presented in figure 4.30(b). During the simulation, the desired loading of the film is then applied linearly as function of time. During each load increment, the equilibrium elastic stress field inside the bulk material is calculated using the finite element solver and the results of the previous discrete dislocation dynamics calculation. The stress acting on each dislocation segment is then actualized and the segments are displaced accordingly. The dislocation motion is repeated until all the dislocations reach their equilibrium state. The algorithm then moves to the next loading increment in the FEM problem.

For the moment, we are working on the compensation of the traction at the free surfaces of the film by implementing image stresses [47]. Preliminary results of the buckling thin films obtained using FEM/DDD coupling should however be obtained soon.

Other questions raised by experiments

In the frame of our study, we considered exclusively two simple buckling structures which are straight and circular blisters. However, the observations of the buckling structures in ductile thin films reveal more complex structures. For instance, a snail-like structure have been observed in a $630\ \mathrm{nm}$ gold thin film deposited on a Si(100) substrate[18] and is shown in figure 4.31(a). It is thought that such structures result from the successive growth of a circular blister during the thin film deposition. To model such structures, a model taking into account the variation of the thickness during the loading should be developed.

Another interesting structure has been observed in a $200\ \mathrm{nm}$ thin film and features a straight blister segment with two circular blisters at its ends, as shown in figure 4.31(b). When observing the circular blister located at the top of figure 4.31(b), we can also notice two growing straight blisters in the form of branches. This structure could result either from the interaction between a straight and a circular blister or from the destabilization of the circular blister itself into a straight one. The study of the interaction of a straight blister and a circular one should be feasible using the $3D$ finite element model developed in this work.

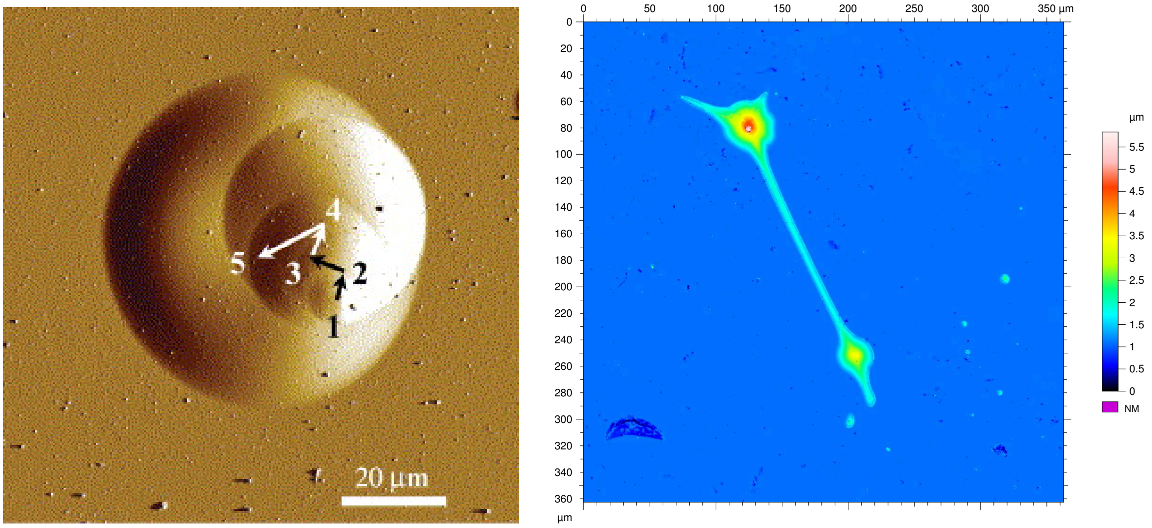

(a) (b)

FIGURE 4.31: *Examples of unresolved cases of buckling delamination structures in gold thin film. (a) Signal error-mode atomic force microscopy image of a snail like blister. The rings result from the successive growth of one circular blister in a gold thin film, labelled from initial state 1 to the final position 5. – Au(630 nm) on Si [18]. (b) interaction between straight and circular blisters – Au(200 nm) on Si.(Courtesy of C. Coupeau, Institut P')*

Appendix A

Influence of mesh size on elastic-plastic response

Choosing the right element type and size is a fundamental part in any FEM simulation process. It influences the accuracy, convergence and speed of the solution especially in non-linear problems with high local deformation and high stress concentration, which are encountered in elastic-plastic buckling problems. In this part, we will focus therefore on investigating the effect of elements type and discretization on the buckling profiles and plastic deformation of elastic-plastic thin films. Once the choice of element's type set, we will investigate the effect of mesh density on the final result and choose a density that provides good balance between accuracy and calculations' speed. In order to have reasonably short running times, we chose to perform this study using only a straight blister geometry.

A.1 selection of the appropriate element's type

During elastic-plastic buckling, thin films undergo large deformations and can exhibit large stress concentration resulting in plastic deformations especially near the interface between the film and the rigid substrate. In order to solve this non-linear problem numerically optimally, one needs to perform non-linear analysis and use 3D elements that can sustain rigid contact, plasticity and large deformations. Moreover, quadratic interpolation is known to provide higher accuracy than first order interpolation in bending problems, and to favor localization of plastic strains. Among quadratic 3D elements available in ABAQUS elements' library, one can find tetrahedrons and bricks. Although tetrahedral elements are very convenient to mesh complex shapes and perform refined meshing, they can exhibit poor convergence rates especially in problems involving hard contact. For this reason, we mainly used quadratic uniform bricks in buckling problems. We also tested (as presented in the next paragraph) a combination of quadratic bricks and tetrahedrons: We used refined bricks near the base of the blister where shear stress and plastic deformation are the highest, and meshed the remaining parts automatically with tetrahedrons as presented in figure A.5 .

In our case study, because the thickness is small compared to the in-plane dimensions, it can be very tempting to uses shell elements in order to reduce computational costs. However, it should be noted that in the formulation of conventional shell elements, the constitutive equations are projected onto the shell reference surface which is usually the mid-surface. It is clear that such a formulations is not suitable with the application of three-dimensional elastic-plastic constitutive equations. To encounter this issue, the use of 3D shell elements called continuum shell elements instead of the conventional ones is recommended in ABAQUS. In fact, continuum shells have several integration points through thickness which make it possible to discretize an entire three-dimensional body and estimate its through-thickness section forces. So, from a modelling point of view, these elements are three-dimensional elements with the kinematics of conventional shell elements [21].

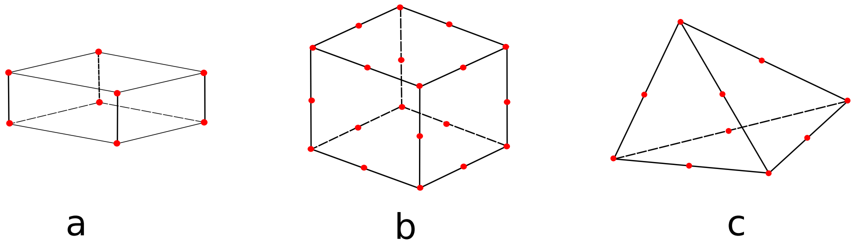

FIGURE A.1: *Shell and solid elements: (a) Continuum shell linear elements (8-node brick, SC8R), (b) Solid quadratic element (20-node brick, C3D20), (c) Solid quadratic element (10-node tetrahedron, C3D10)*

It should be noted that continuum shell elements can be stacked to provide more refined through-thickness response allowing a richer transverse shear stress and force prediction.

To sum up, the elements used in the frame of this study are the following (see fig A.1):

- SC8R: continuum shell element, 8-node linear brick, reduced integration
- C3D20: solid element, 20-node quadratic brick, full integration
- C3D10: solid element, 10-node quadratic tetrahedron, full integration

A.1.1 Solid elements versus continuum shells

Although continuum shell elements seem to properly discretize a three-dimensional body, especially when several elements are stacked through the thickness, we decided to verify to what extend the overall deformation sustained by these elements is consistent with that of solid elements. We ran several simulations using continuum shell elements (SC8R) and solid quadratic bricks (C3D20) and compared their respective responses to different $\frac{\sigma_0}{\sigma_y}$ ratios in terms of final blister shape and equivalent plastic strain. The geometry is chosen according to the experimental case study presented in section 2.1 and we chose to place several elements through the thickness in both solid and continuum shell simulations, for the sake of accuracy. We resumed the different parameters in the table A.1.

The different profiles are plotted in figure A.2. Curves corresponding to solid element response are plotted in plain lines whereas those corresponding to continuum shell response are plotted in dotted lines. We can notice that for ratios $\frac{\sigma_0}{\sigma_y} \leq 1.06$, solid and shell curves are almost superimposed. However for the highest value of $\frac{\sigma_0}{\sigma_y}$, there is a small difference

Geometry		Elastic properties		Ludwik's law		
h (nm)	$2b$ μm	E GPa	ν (-)	σ_y MPa	K MPa	n (-)
400	11	85	0.44	800	130	0.25

TABLE A.1: *Summary of the geometrical characteristics, the elastic properties the elastic plastic response of the modelled thin film (h: thickness of the film, $2b$: total width of the defect, E: Young's modulus, ν: Poisson's ratio, σ_y: elastic limit, K:, n) for both samples α and γ*

between the two curves: The solid curve is slightly higher than the shell curve. However, at this point we cannot conclude about the reliability of continuum shell elements in the modelling of elastic-plastic behaviour. We still need to look at the distribution of plastic deformations in both solid and continuum shell elements and compare them.

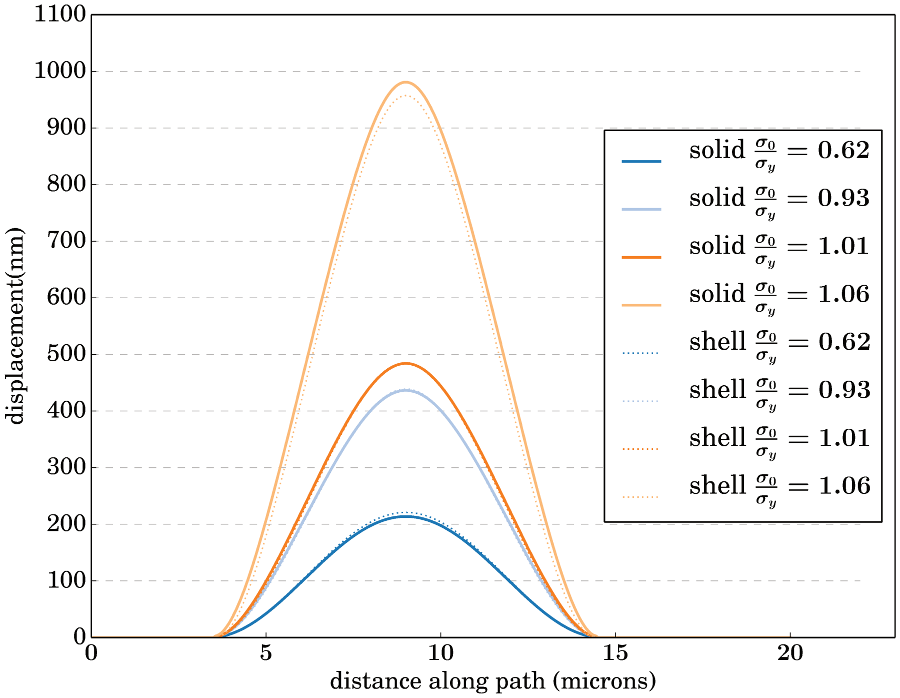

FIGURE A.2: *Effect of the element's type (solid or shell elements) on the elastic-plastic buckling of straight blister. The profiles obtained are given for different σ_0 and the same hardening law (Ludwik $\sigma_y = 800$ MPa, $K = 130$ MPa, $n = 0.25$)*

In figure A.3, we plotted the equivalent plastic strain (PEEQ) mapping for the ratio $\frac{\sigma_0}{\sigma_y} = 1.06$ for solid and continuum shell elements. In order to make the comparison convenient, we used the same colour scale and set the same maximum value (5%) for both mappings even-thought the maximum PEEQ values are different. On the one hand, the two profiles present some similarities:

- Both cases present global plastic deformation ($\sigma_0 > \sigma_y$) with non-homogeneous distribution.

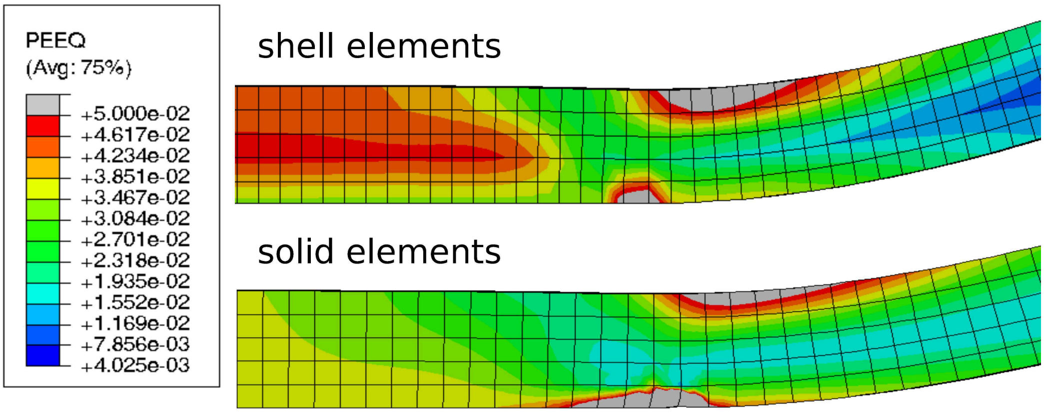

FIGURE A.3: *Equivalent plastic strain mapping obtained in the case of solid and shell elements for the same* $\sigma_0 = 850$ MPa *and the same hardening law (Ludwik* $\sigma_y = 800$ MPa, $K = 130$ MPa, $n = 0.25$*)*

- The maximum PEEQ value is reached at the folding area of the film near the interface between the film and the rigid substrates. The top part of the film concerned with folding also have high values of PEEQ (higher than 5%).
- The plane area of the film (unbended) has sensibly lower PEEQ values (less than 5%).

On the other hand, the two cases present some differences, caracterized by various PEEQ distributions and concentration areas:

- In the case of continuum shell elements, the maximum Value is 6.2% (located at the base of the buckle), whereas in the case of continuum solid elements the value of 26%.
- The area where PEEQ reaches the maximum is more extended in the case of solid elements

As a conclusion, continuum shell elements do not seem to properly capture the plastic deformation and have different equivalent plastic strain distribution and values compared to solid element modelling. This difference have small impact on the profile's shape and hight in the case of simple buckling. However, when delamination is involved such a difference of plastic deformation can have a significant impact on the final diameter of the blister. Thus, even if it makes calculations costs more important, only solid elements have been used in the frame of elastic-plastic buckling.

A.2 Influence of the elements' size

Once the choice of element's type is set (solid element with quadratic interpolation), it is important to study the effect of global and local mesh refinement on elastic-plastic buckling in order to assure good accuracy. The main challenge is to find the best compromise between calculations costs and accuracy. In fact, refined meshes guarantee a good accuracy but can be very demanding in terms of calculation time and convergence rate, whereas bigger elements are known to speed the calculations while being less accurate. In this study, we tested several solid elements' sizes. The process of mesh refinement starts by resolving the buckling problem with a coarse mesh (3 elements through thickness) before moving successively to finer meshes and comparing the results between these different meshes in term of buckling profiles and plastic strain distribution. The geometry, elastic properties and hardening law are the same for the different mesh sizes and are identical to those presented in table A.1. We set the final post buckling stress to the value ($\frac{\sigma_0}{\sigma_y} = 1.03$) for all the cases. The different levels of refinement are shown in figure A.5 and consist of the following configurations:

- Uniformly refined mesh using solid quadratic hexahedrons, 3 elements through the thickness
- Uniformly refined mesh using solid quadratic hexahedrons, 5 elements through the thickness
- Uniformly refined mesh using solid quadratic hexahedrons, 10 elements through the thickness
- Uniformly refined mesh using solid quadratic hexahedrons, 30 elements through the thickness
- Locally refined mesh using solid quadratic hexahedrons at the folding area (20 elements through the thickness), the remaining part of the film is meshed with coarser tetrahedral elements (4 elements through thickness)

Lets us first focus on uniform hexahedral meshes. The equivalent plastic strain mapping of the coarsest meshing presented in figure A.5 reveals little plastic strain concentration at the folding area of the blister. At the interface between the film and the substrate, the maximum value doesn't exceed 5% and is located within a single layer of elements. It is clear that this level of refinement is not sufficient. Ideally, we would like to observe a concentration of plastic deformation within multiple element layers. When using 5 elements through the thickness, the maximum PEEQ value is this time equal to 10.55% and the corresponding area is still located within a single layer of elements. For 10 and 30 elements through thickness, the maximum PEEQ value is equal to 21.11% and 47% respectively. The area corresponding to $PEEQ > 5\%$ seems to be more extended along x direction. However it is still confined within a single layer of elements along the z direction. Computing simulations with higher number of elements through thickness were difficult to perform as it resulted in higher PEEQ values and convergence problems. The uniform meshes with 10 and 30 elements through thickness capture in similar ways the plastic distribution with a difference in the maximum PEEQ values reached. Moreover, their buckling profiles presented in figure A.4 are also very similar and above those corresponding to 3 and 5 elements through thickness. keeping in mind computational costs, modelling the films with 10 elements through thickness is more convenient and reasonable although less accurate.

In order to get more accurate results at lower or similar convergence rate, we tried elaborating a locally refined mesh: We used solid hexahedrons at the area of interest (folding

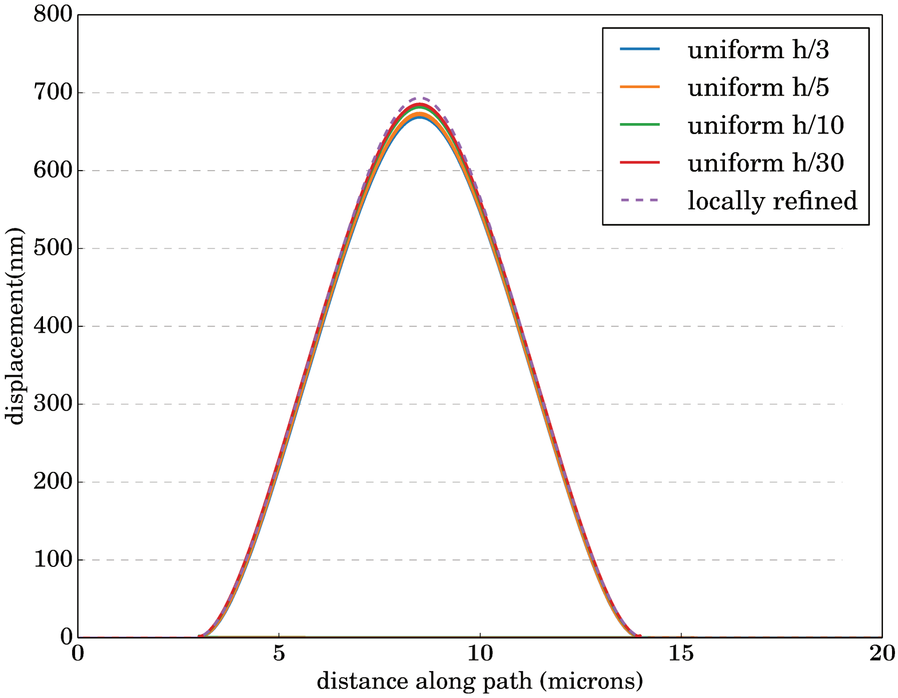

FIGURE A.4: *Effect of mesh refinement on the buckling profile of straight blisters. The profiles are obtained for the same ratio* $\frac{\sigma_0}{\sigma_y} = 1.03$*, the same hardening law (Ludwik* $\sigma_y = 800$ MPa, $K = 130$ MPa, $n = 0.25$*) and different solid element sizes. (see figure A.5)*

area) and meshed the remaining part of the film with coarser tetrahedral elements using the automatic meshing algorithm of ABAQUS. in terms of plastic strain distribution, the locally refined configuration is very similar to that of uniform meshing with 30 elements across the thickness. it also have similar maximum PEEQ value reaching 43%. However when considering the buckling profiles, we can see that the locally refined mesh case reaches higher deflection than any other uniform meshing case. this can be explained by the fact that solid terahedrons are known to overestimate the bending stiffness [21]. In addition, they have slower convergence rate compared to hexahedrons and showed instabilities in the boundary between hexahedrons and tetrahedrons. Locally refining the part seems interesting but should be done using only hexahedral elements which usually done manually and is difficult to automate. In our case, the best compromise between accuracy and computational costs corresponds to the uniform hexahedral mesh with 10 elements through the thickness, which is the configuration that has been used.

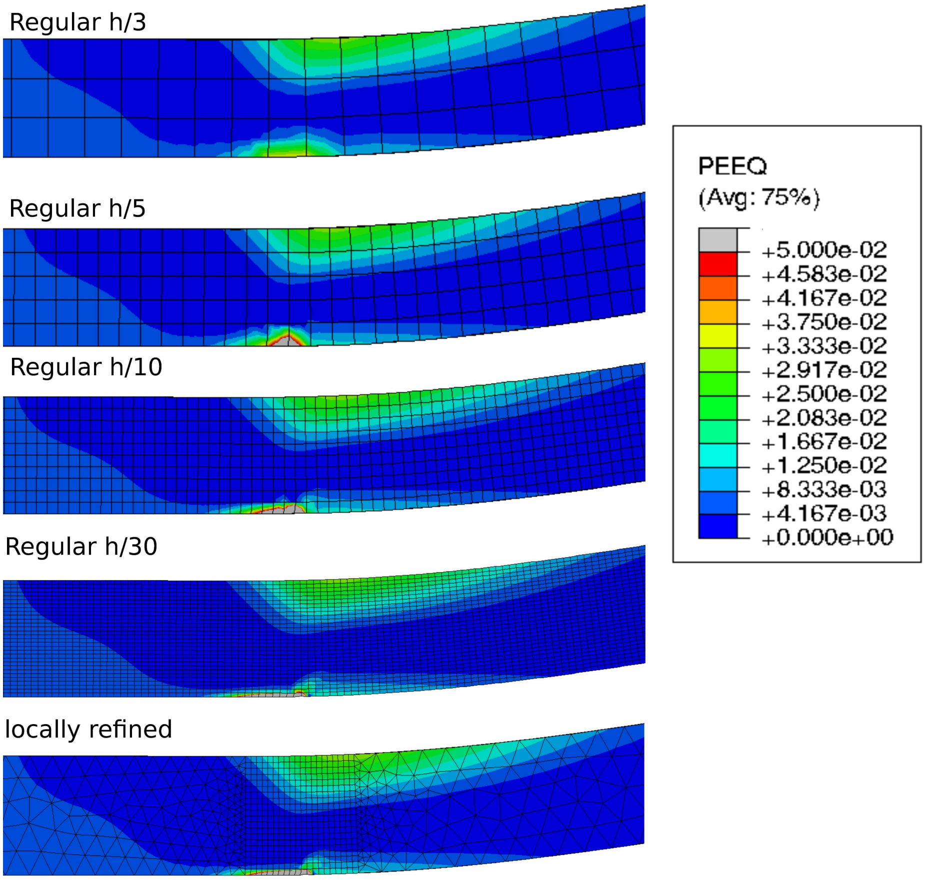

FIGURE A.5: *Effect of mesh refinement on the equivalent plastic strain distribution. The profiles are obtained for the same ratio* $\frac{\sigma_0}{\sigma_y} = 1.03$*, the same hardening law (Ludwik* $\sigma_y = 800$ MPa, $K = 130$ MPa, $n = 0.25$*) and different solid element sizes: Uniform hexahedral mesh with respectively 3, 5, 10 and 30 elements through thickness. The last case has hybrid meshing with locally refined hexahedrons at the folding area (20 elements) and coarser tetrahedrons in the remaining part. (*$\sigma_0 = 830$ MPa, $\sigma_y = 800$ MPa, $K = 130$ MPa, $n = 0.25$*)*

Bibliography

[1] G Abadias et al. “Real-time stress evolution during early growth stages of sputter-deposited metal films: influence of adatom mobility”. In: *Vacuum* 100 (2014), pp. 36–40.

[2] Michael F Ashby and DR Jones. “Engineering materials 1. An introduction to their properties and applications”. In: *Fuel and Energy Abstracts*. Vol. 4. 36. 1995, p. 284.

[3] B Audoly, B Roman, and A Pocheau. “Secondary buckling patterns of a thin plate under in-plane compression”. In: *The European Physical Journal B-Condensed Matter and Complex Systems* 27.1 (2002), pp. 7–10.

[4] Basile Audoly. “Stability of straight delamination blisters”. In: *Physical review letters* 83.20 (1999), p. 4124.

[5] G.I. Barenblatt. “The Mathematical Theory of Equilibrium Cracks in Brittle Fracture”. In: ed. by G. Kuerti F.H. van den Dungen H.L. Dryden Th. von Kármán and L. Howarth. Vol. 7. Advances in Applied Mechanics. Elsevier, 1962, pp. 55 –129.

[6] R Boijoux, G Parry, and C Coupeau. “Buckle depression as a signature of Young’s modulus mismatch between a film and its substrate”. In: *Thin Solid Films* 645 (2018), pp. 379–382.

[7] Jean-Luc Bucaille et al. “A new technique to determine the elastoplastic properties of thin metallic films using sharp indenters”. In: *Thin Solid Films* 447 (2004), pp. 239–245.

[8] SI Bulychev et al. “Determining Young’s modulus from the indentor penetration diagram”. In: *Ind. Lab.* 41.9 (1975), pp. 1409–1412.

[9] Godofredo T Camacho and M Ortiz. “Computational modelling of impact damage in brittle materials”. In: *International Journal of solids and structures* 33.20-22 (1996), pp. 2899–2938.

[10] E Chason et al. “Origin of compressive residual stress in polycrystalline thin films”. In: *Physical Review Letters* 88.15 (2002), p. 156103.

[11] Thomas Chudoba et al. “Comparison of nanoindentation results obtained with Berkovich and cube-corner indenters”. In: *Philosophical Magazine* 86.33-35 (2006), pp. 5265–5283.

[12] F Cleymand, C Coupeau, and J Grilhé. “Atomic force microscopy investigation of buckling patterns of nickel thin films on polycarbonate substrates”. In: *Philosophical Magazine Letters* 82.9 (2002), pp. 477–482.

[13] Jérôme Colin, Christophe Coupeau, and Jean Grilhé. “Plastic folding of buckling structures”. In: *Physical review letters* 99.4 (2007), p. 046101.

[14] MJ Cordill, NR Moody, and DF Bahr. "The effects of plasticity on adhesion of hard films on ductile interlayers". In: *Acta Materialia* 53.9 (2005), pp. 2555–2562.

[15] MJ Cordill et al. "Adhesion measurements using telephone cord buckles". In: *Materials Science and Engineering: A* 443.1 (2007), pp. 150–155.

[16] C Coupeau. "Atomic force microscopy study of the morphological shape of thin film buckling". In: *Thin Solid Films* 406.1 (2002), pp. 190–194.

[17] C Coupeau and J Grilhé. "Atomic force microscopy observations of in situ deformed materials: application to single crystals and thin films on substrates". In: *Journal of microscopy* 203.1 (2001), pp. 99–107.

[18] C Coupeau et al. "Evidence of plastic damage in thin films around buckling structures". In: *Thin Solid Films* 469 (2004), pp. 221–226.

[19] Jyoti Das et al. "The Fourth-order Bessel–type Differential Equation". In: *Applicable Analysis* 83.4 (2004), pp. 325–362.

[20] B Devincre et al. "Three-dimensional simulations of plastic flow in crystals". In: *Microscopic simulations of complex hydrodynamic phenomena*. Springer, 1992, pp. 413–423.

[21] Abaqus Documentation and User Manual. "6.14 Documentation". In: *Dassault Systemes* (2014).

[22] MF Doerner, DS Gardner, and WD Nix. "Plastic properties of thin films on substrates as measured by submicron indentation hardness and substrate curvature techniques." In: *Journal of Materials Research* 1.06 (1986), pp. 845–851.

[23] Donald S Dugdale. "Yielding of steel sheets containing slits". In: *Journal of the Mechanics and Physics of Solids* 8.2 (1960), pp. 100–104.

[24] J. Dundurs. In: *J Appl Mech* 36 (1969), p. 650.

[25] Julien Durinck et al. *A stress relaxation mechanism through buckling-induced dislocations in thin films*. 2010.

[26] Julien Durinck et al. "Molecular dynamics simulations of buckling-induced plasticity". In: *Applied Physics Letters* 93.22 (2008), p. 221904.

[27] RD Emery and GL Povirk. "Tensile behavior of free-standing gold films. Part I. Coarse-grained films". In: *Acta Materialia* 51.7 (2003), pp. 2067–2078.

[28] Anthony G Evans and John W Hutchinson. "Effects of non-planarity on the mixed mode fracture resistance of bimaterial interfaces". In: *Acta Metallurgica* 37.3 (1989), pp. 909–916.

[29] J-Y Faou, Etienne Barthel, and Sergey Y Grachev. "Stress tuning in sputter-deposited MoO x films". In: *Thin Solid Films* 527 (2013), pp. 222–226.

[30] Jean-Yvon Faou. "Mechanics of functionnal thin films: instabilities and adhesion". PhD thesis. Université Pierre et Marie Curie-Paris VI, 2013.

[31] Jean-Yvon Faou et al. "How does adhesion induce the formation of telephone cord buckles?" In: *Physical review letters* 108.11 (2012), p. 116102.

[32] Jean-Yvon Faou et al. “Telephone cord buckles—A relation between wavelength and adhesion”. In: *Journal of the Mechanics and Physics of Solids* 75 (2015), pp. 93–103.

[33] D Faurie et al. “Measurement of thin film elastic constants by X-ray diffraction”. In: *Thin Solid Films* 469 (2004), pp. 201–205.

[34] Jerrold A Floro, Eric Chason, and AR Krauss. “Curvature-based techniques for real-time stress measurement during thin film growth”. In: *Situ Real-Time Characterization of Thin Films* (2001).

[35] Jerrold A Floro et al. “Physical origins of intrinsic stresses in Volmer–Weber thin films”. In: *MRS bulletin* 27.1 (2002), pp. 19–25.

[36] August Föppl. *Vorlesungen über technische Mechanik: Bd. Die wichtigsten Lehren der höheren Elastizitätstheorie. 1907. xi, 391,[1] p. 44 diagr*. Vol. 5. BG Teubner, 1907.

[37] Lambert Ben Freund and Subra Suresh. *Thin film materials: stress, defect formation and surface evolution*. Cambridge University Press, 2004.

[38] Kaustubh S Gadre and TL Alford. “Contact angle measurements for adhesion energy evaluation of silver and copper films on parylene-n and SiO 2 substrates”. In: *Journal of applied physics* 93.2 (2003), pp. 919–923.

[39] William F Gale and Terry C Totemeier. *Smithells metals reference book*. Butterworth-Heinemann, 2003.

[40] YF Gao and AF Bower. “A simple technique for avoiding convergence problems in finite element simulations of crack nucleation and growth on cohesive interfaces”. In: *Modelling and Simulation in Materials Science and Engineering* 12.3 (2004), p. 453.

[41] M George et al. “Delamination of metal thin films on polymer substrates: from straight-sided blisters to varicose structures”. In: *Philosophical Magazine A* 82.3 (2002), pp. 633–641.

[42] G Gille and B Rau. “Buckling instability and adhesion of carbon layers”. In: *Thin Solid Films* 120.2 (1984), pp. 109–121.

[43] Gustavo Gioia and Michael Ortiz. “Delamination of compressed thin films”. In: *Advances in applied mechanics* 33.08 (1997), pp. 119–192.

[44] Julia R Greer, Warren C Oliver, and William D Nix. “Size dependence of mechanical properties of gold at the micron scale in the absence of strain gradients”. In: *Acta Materialia* 53.6 (2005), pp. 1821–1830.

[45] Alan A Griffith. “The phenomena of rupture and flow in solids”. In: *Philosophical transactions of the royal society of london. Series A, containing papers of a mathematical or physical character* 221 (1921), pp. 163–198.

[46] S Hamade et al. “Effect of plasticity and atmospheric pressure on the formation of donut-and croissantlike buckles”. In: *Physical Review E* 91.1 (2015), p. 012410.

[47] A Hartmaier et al. “Image stresses in a free-standing thin film”. In: *Modelling and Simulation in Materials Science and Engineering* 7.5 (1999), p. 781.

[48] John W Hutchinson and Zhigang Suo. "Mixed mode cracking in layered materials". In: *Advances in applied mechanics* 29.63 (1992), p. 191.

[49] JW Hutchinson, MD Thouless, and EG Liniger. "Growth and configurational stability of circular, buckling-driven film delaminations". In: *Acta metallurgica et materialia* 40.2 (1992), pp. 295–308.

[50] Robert G Hutchinson and John W Hutchinson. "Lifetime assessment for thermal barrier coatings: tests for measuring mixed mode delamination toughness". In: *Journal of the American Ceramic Society* 94.s1 (2011).

[51] ASM International, ASM International. Handbook Committee, and ASM International. Alloy Phase Diagram Committee. *Metals Handbook: Properties and selection*. Vol. 2. Asm International, 1990.

[52] George R Irwin. "Fracture Mechanics". In: *Structural Mechanics, Proceedings of the First symposium on Naval Structural Mechanics* (1960), pp. 557–591.

[53] Faou Jean-Yvon et al. "From telephone cords to branched buckles: A phase diagram". In: *Acta Materialia* 125 (2017), pp. 524–531.

[54] MF Kanninen. "An augmented double cantilever beam model for studying crack propagation and arrest". In: *International Journal of fracture* 9.1 (1973), pp. 83–92.

[55] BJORN Karlsson et al. "Materials for solar-transmitting heat-reflecting coatings". In: *Thin Solid Films* 86.1 (1981), pp. 91–98.

[56] Von Theodore Kármán. *Festigkeitsprobleme im Maschinenbau, Encyclopädie der mathematischen Wissenschaften IV*. Teubner Verlag, Leipzig, 1910.

[57] M Kemdehoundja, JL Grosseau-Poussard, and JF Dinhut. "Raman microprobe spectroscopy measurements of residual stress distribution along blisters in Cr 2 O 3 thin films". In: *Applied Surface Science* 256.9 (2010), pp. 2719–2725.

[58] Koreo Kinosita. "Recent developments in the study of mechanical properties of thin films". In: *Thin Solid Films* 12.1 (1972), pp. 17–28.

[59] Rajesh Kitey, Philippe H Geubelle, and Nancy R Sottos. "Mixed-mode interfacial adhesive strength of a thin film on an anisotropic substrate". In: *Journal of the Mechanics and Physics of Solids* 57.1 (2009), pp. 51–66.

[60] HJ Kleemola and MA Nieminen. "On the strain-hardening parameters of metals". In: *Metallurgical transactions* 5.8 (1974), pp. 1863–1866.

[61] R Koch. "The intrinsic stress of polycrystalline and epitaxial thin metal films". In: *Journal of Physics: Condensed Matter* 6.45 (1994), p. 9519.

[62] LP Kubin and G Canova. "The modelling of dislocation patterns". In: *Scripta metallurgica et materialia* 27.8 (1992), pp. 957–962.

[63] Lev D Landau and EM Lifshitz. "Theory of Elasticity, vol. 7". In: *Course of Theoretical Physics* 3 (1986), p. 109.

[64] Michael Lane et al. “Plasticity contributions to interface adhesion in thin-film interconnect structures”. In: *Journal of materials research* 15.12 (2000), pp. 2758–2769.

[65] KM Liechti and YS Chai. “Asymmetric shielding in interfacial fracture under in-plane shear”. In: *Journal of applied mechanics* 59.2 (1992), pp. 295–304.

[66] DM Lipkin, DR Clarke, and AG Evans. “Effect of interfacial carbon on adhesion and toughness of gold–sapphire interfaces”. In: *Acta materialia* 46.13 (1998), pp. 4835–4850.

[67] JL Loubet et al. “Vickers indentation curves of magnesium oxide (MgO)”. In: *Journal of tribology* 106.1 (1984), pp. 43–48.

[68] P Ludwik. “Element der Technologischen”. In: *Mechanik* 166 (1909).

[69] André Mézin. “Coating internal stress measurement through the curvature method: A geometry-based criterion delimiting the relevance of Stoney’s formula”. In: *Surface and Coatings Technology* 200.18 (2006), pp. 5259–5267.

[70] M-W Moon et al. “Buckle delamination on patterned substrates”. In: *Acta Materialia* 52.10 (2004), pp. 3151–3159.

[71] MW Moon et al. “The characterization of telephone cord buckling of compressed thin films on substrates”. In: *Journal of the Mechanics and Physics of Solids* 50.11 (2002), pp. 2355–2377.

[72] D Nir. “Stress relief forms of diamond-like carbon thin films under internal compressive stress”. In: *Thin solid films* 112.1 (1984), pp. 41–50.

[73] Milton Ohring. *Materials science of thin films*. Academic press, 2001.

[74] Warren Carl Oliver and George Mathews Pharr. “An improved technique for determining hardness and elastic modulus using load and displacement sensing indentation experiments”. In: *Journal of materials research* 7.06 (1992), pp. 1564–1583.

[75] M Ortiz and A Pandolfi. “CALTECH ASCI TECHNICAL REPORT 090”. In: *Int. J. Numer. Meth. Engng* 44 (1999), pp. 1267–1282.

[76] B. Panicaud and J.L. Grosseau-Poussard. “Stress analysis of local blisters coupling Raman spectroscopy and X-ray diffraction. Correlation between experimental results and continuous damage modelling for buckling in an iron oxide/phosphated iron system”. In: *Applied Surface Science* 257.4 (2010), pp. 1282 –1288. ISSN: 0169-4332. DOI: `http://dx.doi.org/10.1016/j.apsusc.2010.08.048`. URL: `http://www.sciencedirect.com/science/article/pii/S0169433210011256`.

[77] Kyoungsoo Park and Glaucio H Paulino. “Cohesive zone models: a critical review of traction-separation relationships across fracture surfaces”. In: *Applied Mechanics Reviews* 64.6 (2011), p. 060802.

[78] G Parry et al. “Stability diagram of unilateral buckling patterns of strip-delaminated films”. In: *Physical Review E* 74.6 (2006), p. 066601.

[79] Per-Erik Petersson. “Crack growth and development of fracture zones in plain concrete and similar materials”. PhD thesis. Division, Inst., 1981.

[80] JB Pethicai, R Hutchings, and Wi C Oliver. "Hardness measurement at penetration depths as small as 20 nm". In: *Philosophical Magazine A* 48.4 (1983), pp. 593–606.

[81] GM Pharr and A Bolshakov. "Understanding nanoindentation unloading curves". In: *Journal of Materials Research* 17.10 (2002), pp. 2660–2671.

[82] Ivar E Reimanis et al. "Effects of plasticity on the crack propagation resistance of a metal/ceramic interface". In: *Acta metallurgica et materialia* 38.12 (1990), pp. 2645–2652.

[83] P.O. Renault et al. "Damage mode tensile testing of thin gold films on polyimide substrates by X-ray diffraction and atomic force microscopy". In: *Thin Solid Films* 424.2 (2003), pp. 267 –273. ISSN: 0040-6090. DOI: `http://dx.doi.org/10.1016/S0040-6090(02)01127-6`. URL: `http://www.sciencedirect.com/science/article/pii/S0040609002011276`.

[84] J. Rice. "Elastic Fracture Mechanics concepts for interfacial cracks". In: *J. Appl. Mech.* 55 (1988), pp. 98–103.

[85] James R Rice, Zhigang Suo, and Jian-Sheng Wang. "MECHANICS AND 1HERMO-DYNAMICS OF BRITILE IN1ERFACIAL FAILURE IN BIMATERIAL SYSTEMS". In: (1990).

[86] R.O. Ritchie, C.J. Gilbert, and J.M. McNaney. "Mechanics and mechanisms of fatigue damage and crack growth in advanced materials". In: *International Journal of Solids and Structures* 37.1–2 (2000), pp. 311 –329. ISSN: 0020-7683. DOI: `http://dx.doi.org/10.1016/S0020-7683(99)00096-7`. URL: `http://www.sciencedirect.com/science/article/pii/S0020768399000967`.

[87] A Ruffini et al. "Gliding at interface during thin film buckling: A coupled atomistic/elastic approach". In: *Acta Materialia* 60.3 (2012), pp. 1259–1267.

[88] Antoine Ruffini et al. "Buckling-induced dislocation emission in thin films on substrates". In: *International Journal of Solids and Structures* 50.22 (2013), pp. 3717–3722.

[89] Antoine Ruffini et al. "Effect of interface plasticity on circular blisters". In: *Scripta Materialia* 113 (2016), pp. 222–225.

[90] S. Sakai, H. Tanimoto, and H. Mizubayashi. "Mechanical behavior of high-density nanocrystalline gold prepared by gas deposition method". In: *Acta Materialia* 47.1 (1998), pp. 211 –217. ISSN: 1359-6454. DOI: `http://dx.doi.org/10.1016/S1359-6454(98)00339-5`. URL: `http://www.sciencedirect.com/science/article/pii/S1359645498003395`.

[91] I. Scheider and W. Brocks. "Simulation of cup–cone fracture using the cohesive model". In: *Engineering Fracture Mechanics* 70.14 (2003). Cohesive Models, pp. 1943 –1961. ISSN: 0013-7944. DOI: `http://dx.doi.org/10.1016/S0013-7944(03)00133-4`. URL: `http://www.sciencedirect.com/science/article/pii/S0013794403001334`.

[92] C.F Shih. In: *Mater. Sci. Eng. A* 143 (1991), pp. 77–90.

[93] Ian N Sneddon. “Boussinesq’s problem for a rigid cone”. In: *Mathematical Proceedings of the Cambridge Philosophical Society*. Vol. 44. 4. Cambridge University Press. 1948, pp. 492–507.

[94] G Gerald Stoney. “The tension of metallic films deposited by electrolysis”. In: *Proceedings of the Royal Society of London. Series A, Containing Papers of a Mathematical and Physical Character* 82.553 (1909), pp. 172–175.

[95] D. Tabor. “The hardness of solids”. In: *Review of Physics in Technology* 1.3 (1970), p. 145. URL: `http://stacks.iop.org/0034-6683/1/i=3/a=I01`.

[96] P-Y Théry et al. “Adhesion energy of a YPSZ EB-PVD layer in two thermal barrier coating systems”. In: *Surface and Coatings Technology* 202.4 (2007), pp. 648–652.

[97] John Michael Tutill Thompson and Giles W Hunt. *A general theory of elastic stability*. Wiley, 1973.

[98] John A Thornton and DW Hoffman. “Stress-related effects in thin films”. In: *Thin solid films* 171.1 (1989), pp. 5–31.

[99] MD Thouless. “Combined buckling and cracking of films”. In: *Journal of the American Ceramic Society* 76.11 (1993), pp. 2936–2938.

[100] Michael D Thouless. “Fracture of a model interface under mixed-mode loading”. In: *Acta Metallurgica et Materialia* 38.6 (1990), pp. 1135–1140.

[101] Stephen P Timoshenko and James M Gere. “Theory of elastic stability”. In: (1961).

[102] J Tong, KY Wong, and C Lupton. “Determination of interfacial fracture toughness of bone–cement interface using sandwich Brazilian disks”. In: *Engineering fracture mechanics* 74.12 (2007), pp. 1904–1916.

[103] Viggo Tvergaard. “Effect of fibre debonding in a whisker-reinforced metal”. In: *Materials science and engineering: A* 125.2 (1990), pp. 203–213.

[104] Viggo Tvergaard and John W Hutchinson. “The influence of plasticity on mixed mode interface toughness”. In: *Journal of the Mechanics and Physics of Solids* 41.6 (1993), pp. 1119–1135.

[105] Olaf Van Der Sluis et al. “Stretching-induced interconnect delamination in stretchable electronic circuits”. In: *Journal of Physics D: Applied Physics* 44.3 (2011), p. 034008.

[106] Eduard Ventsel and Theodor Krauthammer. *Thin plates and shells: theory: analysis, and applications*. CRC press, 2001.

[107] M Verdier, M Fivel, and In Groma. “Mesoscopic scale simulation of dislocation dynamics in fcc metals: Principles and applications”. In: *Modelling and Simulation in Materials Science and Engineering* 6.6 (1998), p. 755.

[108] JJ Vlassak and WD Nix. “A new bulge test technique for the determination of Young’s modulus and Poisson’s ratio of thin films”. In: *Journal of Materials Research* 7.12 (1992), pp. 3242–3249.

[109] AA Volinsky, NR Moody, and WW Gerberich. “Interfacial toughness measurements for thin films on substrates”. In: *Acta materialia* 50.3 (2002), pp. 441–466.

[110] J-S Wang and Zhigang Suo. “Experimental determination of interfacial toughness curves using Brazil-nut-sandwiches”. In: *Acta Metallurgica et Materialia* 38.7 (1990), pp. 1279–1290.

[111] George Neville Watson. *A treatise on the theory of Bessel functions*. Cambridge university press, 1995.

[112] Y Wei and JW Hutchinson. “Toughness of Ni/Al2O3 interfaces as dependent on micron-scale plasticity and atomistic-scale separation”. In: *Philosophical Magazine* 88.30-32 (2008), pp. 3841–3859.

[113] ML Williams. “On the stress distribution at the base of a stationary crack”. In: *ASME Journal of Applied Mechanics* 24 (1957), pp. 109–114.

[114] Henry Windischmann. “Intrinsic stress in sputter-deposited thin films”. In: *Critical Reviews in Solid State and Material Sciences* 17.6 (1992), pp. 547–596.

[115] FH Wittmann et al. “Fracture energy and strain softening of concrete as determined by means of compact tension specimens”. In: *Materials and Structures* 21.1 (1988), pp. 21–32.

[116] HY Yu, C Kim, and SC Sanday. “Buckle formation in vacuum-deposited thin films”. In: *Thin Solid Films* 196.2 (1991), pp. 229–233.

[117] Sen-Jiang Yu et al. “Morphological selections and dynamical evolutions of buckling patterns in SiAlNx films: from straight-sided to telephone cord or bubble structures”. In: *Acta Materialia* 64 (2014), pp. 41–53.

Résumé

Les revêtements de couches minces soumis à de fortes contraintes de compression peuvent subir un phénomène de flambage et de délaminage simultané appelé « cloquage ». Le mécanisme de formation et de propagation des cloques en forme de rides droites et des cloques circulaires a largement été étudié dans la littérature en considérant un comportement élastique linéaire pour le film. Cependant, l'effet de la plasticité sur la propagation et l'équilibre de telles cloques, bien que constaté expérimentalement, n'avait pas encore été vraiment étudié à ce jour.

Dans ce travail nous nous intéressons tout d'abord à l'observation et à la caractérisation des structures de flambement observées sur des film d'or déposés sur des substrats en silicium. Des effets de la plasticité sur la morphologie ou la charge critique de flambage des structures cloquées sont mis en évidence de manière quantitative grâce à des techniques d'observation morphologique comme l'AFM, ainsi que des tests mécaniques par nano-indentation et des mesures de contrainte.

Un modèle mécanique est développé, permettant de modéliser le film comme une plaque non-linéaire géométrique au comportement élasto-plastique en contact unilatéral sur un support rigide représentant le substrat. De plus, un modèle de zone cohésive est introduit entre la plaque et le support de manière à prendre en compte le délaminage du film, avec un travail de séparation dépendant de la mixité modale du chargement.

Ce modèle nous a permis de mettre en évidence l'effet de la plasticité sur les profils d'équilibres résultant du cloquage élasto-plastique, pour des morphologies de cloques en ride droite et de cloque circulaire. L'effet sur le décalage de la charge critique de flambage a également été étudié. Enfin, l'influence de la déformation plastique sur le mécanisme de propagation de la rupture interfacial lui même a été étudiée. En particulier, un effet de stabilisation de la forme de cloque circulaire, qui avait été observé expérimentalement dans diverses études, a pu être démontré par le calcul.

Mots-clés : Films minces, flambage, délaminage, plasticité, méthode des éléments finis, zones cohésives.

Abstract

Thin film coatings submitted to high compressive stresses may experience a simultaneous buckling and delamination phenomenon called "blistering". The mechanism of formation and propagation of blisters in the form of straight wrinkles and circular blisters has been extensively studied in the literature considering a linear elastic behavior for the film. However, the effect of plasticity on the propagation and mechanical equilibrium of such blisters, although experimentally observed, had not been systematically studied to date.

In this work, we are interested in the observation and characterization of buckling structures observed on gold films deposited on silicon substrates. The effects of plasticity on the morphology or critical buckling load of buckled structures are quantitatively demonstrated using small scale surface observation techniques such as AFM, as well as mechanical testing by nanoindentation tests and stress measurement methods.

A mechanical model is developed in order to model the film as a geometric nonlinear plate with elastic-plastic behavior in unilateral contact with a rigid support representing the substrate. In addition, a cohesive zone model is introduced between the plate and the support in order to take into account the delamination of the film, with a separation work depending on the mode mix of the interface loading.

This model allowed us to highlight the effect of plasticity on the equilibrium profiles resulting from elastic-plastic blistering, for both straight and circular blisters morphologies. The effect on the offset of the critical buckling load has also been studied. Finally, the influence of plastic deformation on the propagation mechanism of the interfacial fracture itself has been studied. In particular, a stabilizing effect of the circular blister form, which has been observed experimentally in various studies, has been demonstrated through calculation.

Keyword : Thin films, buckling, delamination, plasticity, finite elements method, cohesive zones modeling.